
Quantum State Reconstruction in several-particle systems

Anders Sørrig Mouritzen

Lundbeck Foundation Theoretical Center for Quantum System Research
Department of Physics and Astronomy
University of Århus
Denmark

Ph.D. thesis
July 2007

Contents

1	Welcome	1
1.1	Dear Reader	1
1.2	Introduction to Quantum State Reconstruction	1
1.2.1	States, dynamics and measurements	3
1.3	Overview of this report	4
2	Reconstruction in N-dimensional systems	5
2.1	Synopsis	5
2.2	Introduction	5
2.3	The Harmonic Oscillator	7
2.3.1	The multidimensional oscillator	8
2.3.2	Incommensurable frequencies	10
2.3.3	An example of realizing incommensurable frequencies	12
2.3.4	Commensurable frequencies and partial information	13
2.4	The free particle	16
2.4.1	The one-dimensional case	17
2.4.2	N -dim. free particle, periodic boundary conditions	19
2.4.3	Particle in a box	20
2.5	Summary	22
3	Molecular rotational states	25
3.1	Synopsis	25
3.2	Introduction	25
3.3	A typical alignment experiment	28
3.4	Reconstruction method for linear molecules	30
3.4.1	Free rotation	30
3.4.2	Measurements and observables	32

3.4.3	Reconstruction formulas	33
3.5	Real molecules and centrifugal distortion	38
3.6	Symmetric top states	38
3.7	Discussion	40
4	Vibrations and four-wave mixing	43
4.1	Synopsis	43
4.2	Introduction	44
4.3	States and measurements	45
4.4	Experimental implementation outline	47
4.5	Theory	51
4.5.1	Case (I) : Emission due to a single k	57
4.5.2	Calibration pulse	60
4.5.3	Case (II) : Interference between different k	63
4.5.4	Case (III) : Variation of temperature	65
4.6	Discussion	66
4.6.1	Rotations	66
4.6.2	Generalizations of the method	67
5	Quantum correlations in BEC	71
5.1	Synopsis	71
5.2	Introduction	72
5.3	The MAXENT principle in Quantum State Reconstruction	73
5.3.1	The MAXENT principle and density operators	73
5.4	Description of the condensate	75
5.4.1	The Bogoliubov Hamiltonian	75
5.4.2	Discretization of position and momentum	76
5.4.3	Diagonalization of the Bogoliubov Hamiltonian	78
5.4.4	General para-unitary diagonalization	80
5.5	Using MAXENT with the Bogoliubov approximation	82
5.6	Tomography on three quantum states	85
5.6.1	Initial excited states	85
5.6.2	Results of tomography	86
5.7	Discussion	90
5.7.1	Practical considerations	95
5.8	Conclusion	96

6	Potential-laser effects	99
6.1	Synopsis	99
6.2	Introduction	99
6.3	Theory	102
6.3.1	The Strong Field Approximation	105
6.3.2	The M/A-potential corrected case	109
6.4	Discussion	115
6.4.1	Numerical calculations	115
6.4.2	Prior uses of $\Delta\mathbf{q}^{(1)}$	117
6.4.3	Divergent potentials and the Method of Steepest Descent	117
6.4.4	On the applicability of CEV and Coulomb-Volkov states	118
7	HHG and ATI with rotations and vibrations	123
7.1	Synopsis	123
7.2	Introduction	123
7.3	General considerations	126
7.4	Effects on HHG	127
7.5	Effects on ATI	130
7.6	Conclusion	132
8	Summary and Goodbye	133
A	Wigner functions	a
A.1	Discrete Wigner functions	c
B	Numerical details of chapter 5	e

List of Figures

2.1	Quadrature phases for a two-dimensional harmonic oscillator. . .	11
3.1	Molecule in a laser field: Classical alignment.	27
3.2	Overview of an alignment experiment.	29
4.1	Time sequence of the four laser pulses.	48
4.2	Schematic energy diagram of a four-wave mixing process.	49
4.3	Geometric outline of the four laser pulses.	52
4.4	Schematic spectrogram: case (I).	58
4.5	Schematic spectrogram: case (II).	64
5.1	Density distributions at different times for <i>State 1-3</i>	88
5.2	Absolute normal second moments, <i>State 1</i>	89
5.3	Wigner function for <i>State 1</i>	90
5.4	Absolute normal second moments, <i>State 2</i>	91
5.5	Absolute anomalous second moments, <i>State 2</i>	92
5.6	Absolute normal second moments, <i>State 3</i>	93
5.7	Absolute anomalous second moments, <i>State 3</i>	94
6.1	XUV ionization in presence of a moderately strong IR laser field. . .	103
6.2	Numerical momentum shift of the photoelectron peak in 1D. . .	116

Foreword

This report summarizes the research I did in connection with my Ph.D. education at the Department of Physics and Astronomy, University of Århus. The research was done during the period August 1st 2003 – July 31st 2007 under the supervision of Professor Klaus Mølmer. Apart from being good fun, I have also had the privilege of enjoying the company, help and collaboration of wonderful people both at the University of Århus and at the Steacie Institute for Molecular Sciences in Ottawa, Canada. Thank you, Everybody.

List of publications

1. Anders S. Mouritzen and Klaus Mølmer: *Tomographic reconstruction of quantum correlations in excited Bose-Einstein condensates*, Phys. Rev. A **71**, 033602 (2005); arXiv:cond-mat/0409500.
2. Anders S. Mouritzen and Klaus Mølmer: *Tomographic reconstruction of quantum states in N spatial dimensions*, Phys. Rev. A **73**, 042105 (2006); arXiv:quant-ph/0511173.
3. Anders S. Mouritzen and Klaus Mølmer: *Quantum state tomography of molecular rotation*, J. Chem. Phys. **124**, 24311 (2006); arXiv:quant-ph/0512193.
4. Olga Smirnova, Anders S. Mouritzen, Serguei Patchkovskii and Misha Yu. Ivanov: *Coulomb-laser coupling in strong-field assisted photoionization and molecular tomography*, J. Phys. B. **40**, p. F197-F206 (2007).
5. Christian B. Madsen, Anders S. Mouritzen, Thomas K. Kjeldsen and Lars B. Madsen: *Molecules in intense fields: Effects of alignment in high-harmonic generation and above threshold ionization*, Phys. Rev. A **76**, p. 035401 (2007); arXiv:physics/0703234.

VIII

6. Etienne Brion, Anders S. Mouritzen and Klaus Mølmer: *Conditional dynamics induced by new configurations for Rydberg dipole-dipole interactions*, Phys. Rev. A **76**, p. 022334 (2007); arXiv:0706.0147.
7. Anders S. Mouritzen, Olga Smirnova, Stephanie Gräfe, Rune Lausten and Albert Stolow: *Reconstructing vibrational states in warm molecules using four-wave mixing with femtosecond laser pulses*; arXiv:0706.1452 (2007).

Papers in preparation

8. Rune Lausten, Olga Smirnova, Stephanie Gräfe, Anders S. Mouritzen and Albert Stolow: *Observation of high-order fractional revivals in molecular wavepackets with Four-Wave mixing*.

Chapter 1

Welcome

1.1 Dear Reader

Welcome to my Ph.D. report. Please find a nice, comfy chair and something warm to drink. When you are all set, let us begin our trip.

1.2 Introduction to Quantum State Reconstruction

To get a good feel for what we will be occupied with in this report, let us take a look at the title: "Quantum State Reconstruction in several-particle systems". The "several-particle systems" is easy to understand: It means that our main focus will be on physical systems with more than one particle. The most important systems we will encounter are rotating and vibrating molecules, Bose-Einstein condensates and electron/ion-systems in strong laser fields.

"Quantum State Reconstruction" (QSR) is the research field that binds the topics of this report together, and requires an explanation. "Reconstruction" refers to piecing together knowledge of something that already happened. Like the Belgian detective Mr. Poirot¹ scrutinizes pieces of evidence to reconstruct events surrounding a crime, we will scrutinize the results of measurements to reconstruct a quantum state, i.e. the physical state of a quantum system. Our

¹Mr. Hercule Poirot is the protagonist in many crime-novels by Agatha Christie, e.g. *Murder on the Orient Express* and *Death on the Nile*.

motivation for reconstructing the physical state is that it tells us all there is to know about the physical system; a statement that will be made more clear in section 1.2.1. With this in mind, we will spend the remaining part of this section on introducing the central ideas and concepts behind QSR, leaving the detailed treatments of methods and physical systems to the relevant chapters below.

The reason for seeking a quantum state, rather than a classical physical state, is that a quantum mechanical description is necessary to accurately describe the small objects we will be concerned with: molecules, atoms and electrons. Quantum mechanics seriously complicates finding the state, as there is no single observable that reveals it. This is well-known for pure states, i.e. states that can be characterized by a single wave function, where there is no observable directly revealing this complex function. The same absence is true for the more general case of mixed states, which are states that can be characterized by a density matrix, but not necessarily by a single wave function [1].

Although the state is not directly observable, one can determine the state from measurements of other quantities. This is precisely the aim of QSR. The apparent complication that a measurement disturbs a quantum system is resolved by using an *ensemble* of identically prepared, uncorrelated systems. On each member of the ensemble, one or more commuting measurements are performed, whereafter this member is discarded. Further, the ensemble must be large enough to permit measurement of statistically significant data of all quantities of interest. Naturally, this is exactly what lays ground to the usual statistical Born-interpretation of quantum mechanics. In this report, we shall assume throughout that the measured values are close to their true expectation values, which obviously requires numerous measurements of each quantity. Fortunately, this will be the case in all of the following where an actual experimental situation is involved.

With these definitions, QSR is really an inverse problem, working backwards from precise measurements to the quantum state that caused them. This inverse problem is related to, but different from, problems of estimation, where one tries to make the best guess on certain quantities of interest, given uncertain measurements.

In a broader perspective, there has recently been growing interest in reconstructing quantum states for various systems, for an extensive review see [2]. The general problem of QSR is experimentally and theoretically challenging, and methods tend to apply to only a very particular setting. The most well-known is the tomographic reconstruction of harmonic oscillator states from measurements of spatial distributions [3], [4], which we will introduce and deal

with in the first part of chapter 2. Examples of other systems include particles in traps (neutral atoms [5] and ions [6]), general one-dimensional systems [7], dissociating diatomic molecules [8] and the angular state of an electron in a Hydrogen atom with $n = 3$ [9]. As we move through the chapters, we will compare with these and other prior works where it is relevant.

1.2.1 States, dynamics and measurements

In the previous section, we stated the importance of the physical state and that it can be found from measurements on an ensemble. In this section, we will specify more closely what we mean by the physical state and what these measurements must fulfill.

Before proceeding further, it is important to distinguish between the state of a system and its dynamics. The state contains the answer to all questions we may ask the system at a certain point in time, i.e. the result of all thinkable one-time measurements at this time. In sharp contrast to this state is the concept of dynamics, which is prescriptions for finding the state at a later time, from knowing it at an earlier time.

Having accounted for what we mean by the state, we turn our attention to the measurements we will use to reconstruct this state. To accomplish the reconstruction, we will require knowledge of the results of enough measurements to uniquely determine the state. Such a set of measurements is known as a *quorum*.

Finding a quorum can be straightforward or tedious, depending on both the system and the level of description. In a classical system of particles, one quorum is given by measurements of the coordinates and momenta of all particles at a fixed point of time. However, because we will be dealing with states of small objects, we must use quantum mechanics for an accurate description. In this theory, finding a quorum can be more challenging. For example, the uncertainty principle makes the classical quorum mentioned above fail, since each particle does not simultaneously have both a well-defined position and momentum.

In principle, since the quantum state is completely characterized by its density operator's matrix elements in a complete basis $\{|\lambda\rangle\}$, one could just measure (the real and imaginary values of) all these matrix elements $\langle\lambda|\hat{\rho}|\lambda'\rangle$ - i.e. the density matrix [2]. A well-known example of this is the state of a spin-1/2 system, where the state can be found from measurements of the expectation values of the spin projection along three mutually perpendicular axes. In the general case, however, such a set of observations may be very difficult to perform experimentally, and it will instead be our aim to find the quantum state from ex-

perimentally realizable measurements. In this spirit, we will almost exclusively use the prevalent approach, which is to perform the same type of measurement at different points of time, thereby letting the dynamics reveal the state.

1.3 Overview of this report

As we progress through the chapters, the general trend will be from the most general toward the more specific.

Opening our tour, the chapter 2 will be concerned with the generalizations of two well-known methods of reconstruction from one to N spatial dimensions. In this chapter, nothing is assumed about the quantum state being reconstructed, only the Hamiltonian and measurements are known.

With the insights gained, we move on to chapter 3 where we treat an inherently multidimensional system: The quantum mechanical rigid rotor. We set out from a prevalent experiment on molecules, which allows us to limit the state space enough to completely reconstruct the quantum state.

In chapter 4, we treat another subject important for molecules: reconstruction of the vibrational state of a molecule excited by a laser pulse. In this chapter, several assumptions are made for the state, but knowledge of the exact form of the Hamiltonian is largely circumvented by using a separate calibration experiment.

The intricacy of the system is still deeper in chapter 5, where we treat a many-particle system: A Bose-Einstein condensate. To perform QSR on this complicated system, we use both an approximate Hamiltonian and drastically limit the state space. What is more, we must be content with reconstructing only some aspects of the state rather than the complete many-particle state. Due to these drastic approximations, and to the ability of the chapter's method of accepting imperfect data, classifying it as dealing with reconstruction or estimation is largely a matter of taste.

The two chapters 6 and 7 deal with various processes in molecules and atoms exposed to strong laser fields. The chapters present no state reconstruction methods themselves, but are intimately connected to various recent QSR experiments using ultrashort laser pulses.

Lastly, chapter 8 sums up our experiences and we say goodbye.

Apart from the brief overview here, each chapter but the last will be initiated by a synopsis, revealing the topic and main results of the chapter. In addition, each of these chapters will have its own introduction, setting the scene for the particular subject treated therein.

Chapter 2

Reconstruction in N -dimensional systems

2.1 Synopsis

In this chapter, we will extend two well-known one-dimensional Quantum State Reconstruction (QSR) situations to N spatial dimensions: The harmonic oscillator and the particle in a box using measurements of spatial distributions at different points of time. We assume a time-independent Hamiltonian for which the dynamics along each coordinate always occurs simultaneously with the others and measurements on all coordinates are performed simultaneously. We will give conditions determining whether or not a complete reconstruction is possible, and quantify the amount of information available when it is not.

The chapter is based on the article [10].

2.2 Introduction

So far, most methods in quantum state tomography have been concerned with systems described by only one effective position coordinate. An exception is electromagnetic light systems, where methods for two-dimensional [11], [12] and for N -dimensional [2], [13] QSR have been proposed and demonstrated. All of these methods require the ability to vary the time for the subsystems individually by e.g. delay lines or phase retarders. In contrast, we shall focus on the case where

there is only one common time governing the dynamics of the N coordinates and where the measurements are performed on all coordinates simultaneously. This is not a fundamental limitation since the observables corresponding to the different coordinates commute, but rather a practical limitation since destructive measurements are usually much easier to perform. This scenario applies to trapped particles, so far only treated by quantum state tomography in one spatial dimension (neutral atoms [5] and charged ions [6]), and for vibration in molecules [14]. Another interesting possibility for QSR in higher dimensions uses variation of the Hamiltonian as suggested in [15] and [16] for the transverse motion of an atomic beam. Because of the potential difficulty in varying the Hamiltonian in many cases, we shall consider a time-independent Hamiltonian in the rest of the following.

Throughout this chapter, we shall consider the quantum state as being described by the density operator $\hat{\rho}$, which we treat in the Heisenberg picture¹. Our goal shall be to find this operator; or rather, a complete representation hereof. In section 2.3, this representation will be a complex function, whereas we in section 2.4 will find the matrix elements of $\hat{\rho}$ in the Hamiltonian's eigenbasis. For the measurements, we shall adopt the quantum tomographic approach where only measurements of the spatial distribution is made at different points of time [3], [4], [18]-[21]. From these diagonal elements of the density operator in the position representation, $\text{Pr}(x, t) = {}_t\langle x|\hat{\rho}|x\rangle_t$, and the known time evolution due to the Hamiltonian we obtain the full density matrix $\langle x'|\hat{\rho}|x\rangle$ or, equivalently, the phase space distribution, e.g. the Wigner Function $W(x, p)$ [22] (a brief introduction to Wigner functions is given in appendix A).

We shall in this chapter present the extension of two well-known methods of quantum state tomography in one dimension to N dimensions. In section 2.3 we shall consider the harmonic oscillator by a treatment similar to that in [4]. This is not a trivial extension as revealed by a simple consideration of the dimensionality of the sets of measurements and the quantum state, i.e. the number of continuous parameters required to specify each: $\text{Pr}(x, t)$ and $\langle x'|\hat{\rho}|x\rangle$ are both of dimensionality two in the spatial one-dimensional case, suggesting that one may correspond to the other through a 1 : 1 mapping. In contrast, the N -dimensional sets of measurements $\text{Pr}(x_1, \dots, x_N, t)$ is of dimension $N + 1$, but the density matrix $\langle x'_1, \dots, x'_N|\hat{\rho}|x_1, \dots, x_N\rangle$ is of dimensionality $2N$, suggesting

¹Using the Heisenberg picture, the density operator $\hat{\rho}$ is time independent, whereas the observables are time-dependent. Connecting with the Schrödinger picture, we are finding the state at the initial time, where the two pictures are identical [17]. In the Schrödinger picture, is naturally only necessary to know the state at one point of time to find it at another because we assume that we know the dynamics.

an absence of a 1 : 1 correspondence. Moving on, section 2.4 treats the case of free particles previously considered in one dimension in [21], but with periodic boundary conditions and in a box potential. We finally give a summary of the chapter in section 2.5.

2.3 The Harmonic Oscillator

It is shown in [23] that there is a 1 : 1 correspondence between the density operator and the quantum characteristic function $\widetilde{W}(\xi)$, where ξ is a complex variable². This means that instead of finding $\hat{\rho}$ we may just as well find the quantum characteristic function, and that is exactly what we will do in the following. This is traditionally the main trick used in the quantum state tomography of the harmonic oscillator. Before proceeding to the multidimensional case we will briefly recapitulate this procedure in one dimension. The quantum characteristic function can be found from $\hat{\rho}$ by [23]:

$$\widetilde{W}(\xi) = \text{Tr} \left(e^{\xi \hat{a}^\dagger - \xi^* \hat{a}} \hat{\rho} \right), \quad (2.1)$$

where ξ is a complex variable, free to assume any value. Under the harmonic oscillator Hamiltonian $\hat{H} = \hbar\omega(\hat{a}^\dagger \hat{a} + 1/2)$ with angular frequency ω , the ladder operators in the Heisenberg picture evolve according to $\hat{a}(t) = \hat{a}e^{-i\omega t}$, $\hat{a}^\dagger(t) = \hat{a}^\dagger e^{i\omega t}$. Letting $\theta = \omega t$, the position operator \hat{x} evolves according to:

$$\begin{aligned} \hat{x}(\theta) &= \cos(\theta)\hat{x} + \sin(\theta)\hat{p} \\ &= \frac{1}{\sqrt{2}} (\hat{a}^\dagger e^{i\theta} + \hat{a} e^{-i\theta}). \end{aligned} \quad (2.2)$$

Please note that we use dimensionless coordinates³ x and p . We now make a change of variables in (2.1) from the complex number ξ to two real plane-polar coordinates (η, θ) using $\xi = \frac{i}{\sqrt{2}}\eta e^{i\theta}$:

$$\begin{aligned} \tilde{w}(\eta, \theta) &= \widetilde{W} \left(\frac{i}{\sqrt{2}}\eta e^{i\theta} \right) \\ &= \text{Tr} \left[e^{i\eta \hat{x}(\theta)} \hat{\rho} \right]. \end{aligned} \quad (2.3)$$

²That $\widetilde{W}(\xi)$ and $\hat{\rho}$ contains the same information is also justified in appendix A. There, we also present how to find the $\langle x|\hat{\rho}|x' \rangle$ representation from the characteristic function. For simplicity, we choose the ordering parameter $s = 0$, [4]. This choice corresponds to the choice of the Wigner distribution as the complex Fourier transform of Eq. (2.1).

³For the massive harmonic oscillator, this means measuring x in units of $\sqrt{\hbar/m\omega}$ and p in units of $\sqrt{\hbar m\omega}$.

So far, we have not really done anything: We just introduced an equivalent representation $\tilde{w}(\eta, \theta)$ of the density operator $\hat{\rho}$, which will be convenient for us. It will moreover prove convenient to choose the variables to be in the intervals $-\infty < \eta < \infty$ and $0 \leq \theta < \pi$.

Now, an important observation can be made: The position distribution $\text{Pr}(x, \theta)$ at the time θ/ω is a Fourier transform of the quantum characteristic function $\tilde{w}(\eta, \theta)$:

$$\begin{aligned} \text{Pr}(x, \theta) &= \text{Tr} \{ \hat{\rho} \delta[\hat{x}(\theta) - x] \} \\ &= \text{Tr} \left\{ \hat{\rho} \frac{1}{2\pi} \int_{-\infty}^{\infty} d\eta e^{i\eta[\hat{x}(\theta) - x]} \right\} \\ &= \frac{1}{2\pi} \int_{-\infty}^{\infty} d\eta \tilde{w}(\eta, \theta) e^{-i\eta x}. \end{aligned} \quad (2.4)$$

By inverting this Fourier transformation, we can find the quantum characteristic function $\tilde{w}(\eta, \theta)$ from the measured position distributions:

$$\tilde{w}(\eta, \theta) = \int_{-\infty}^{\infty} dx \text{Pr}(x, \theta) e^{i\eta x}. \quad (2.5)$$

This is the main equation of quantum tomography in one dimension: We can find the quantum state (through the quantum characteristic function) by observing the position distribution for $0 \leq \theta < \pi$ corresponding to one half period of the oscillator.

For completeness we write the result Eq. (2.5) in terms of the Wigner-function; the complex Fourier transform of the characteristic function [23], [22]:

$$\begin{aligned} W(x, p) &= \frac{1}{(2\pi)^2} \int_{-\infty}^{\infty} d\eta \int_0^{\pi} d\theta |\eta| \tilde{w}(\eta, \theta) e^{-i\eta[\cos(\theta)x + \sin(\theta)p]} \\ &= \frac{1}{(2\pi)^2} \int_{-\infty}^{\infty} d\eta \int_0^{\pi} d\theta \int_{-\infty}^{\infty} dx' |\eta| \times \\ &\quad \text{Pr}(x', \theta) e^{i\eta[x - \cos(\theta)x' - \sin(\theta)p]}. \end{aligned} \quad (2.6)$$

2.3.1 The multidimensional oscillator

We proceed to show that it is possible to reconstruct the joint quantum state of a multidimensional harmonic oscillator under certain conditions.

The Hamiltonian is now $\hat{H} = \sum_{j=1}^N \hbar\omega_j (\hat{a}_j^\dagger \hat{a}_j + 1/2)$ and we measure the set of N mutually commuting position operators \hat{x}_j , $j = 1 \dots N$. For notational

simplicity, we arrange these operators in a vector $\hat{\mathbf{x}} = (\hat{x}_1, \dots, \hat{x}_N)$. The N -dimensional quantum characteristic function is now $\widetilde{W}(\boldsymbol{\xi})$, where $\boldsymbol{\xi}$ is a vector of N complex variables ξ_j . As before, we let $\xi_j = \frac{i}{\sqrt{2}}\eta_j e^{i\theta_j}$, with $-\infty < \eta_j < \infty$ and $0 \leq \theta_j < \pi$. This yields the N -dimensional equivalent of Eq. (2.5):

$$\begin{aligned} \tilde{w}(\boldsymbol{\eta}, \boldsymbol{\theta}) &= \widetilde{W}(\boldsymbol{\xi}) \\ &= \text{Tr} \left\{ \exp \left[i \sum_{j=1}^N \eta_j \hat{x}_j(\theta_j) \right] \hat{\rho} \right\} \\ &= \int_{-\infty}^{\infty} d^N \mathbf{x} \text{Pr}(\mathbf{x}, \boldsymbol{\theta}) e^{i\boldsymbol{\eta} \cdot \mathbf{x}}. \end{aligned} \quad (2.7)$$

To gain full knowledge of the function $\tilde{w}(\boldsymbol{\eta}, \boldsymbol{\theta})$ we must be able to vary the N variables θ_j independently of each other on the interval $0 \leq \theta_j < \pi$. This is naturally not possible when considering destructive measurements, since we can only vary the N variables comprising $\boldsymbol{\theta}$ through variation of the one parameter t . A way to clearly see this restriction is by noticing that the present reconstruction scheme relies on a Fourier-transformation, which preserves dimensionality. While we measure the joint spatial distribution in N dimensions for different t , this equals $N + 1$ dimensional measurements, while the quantum state (e.g. the characteristic function or Wigner function) is a $2N$ -dimensional object.

It is important to realize what kind of limitations are implied by the inability to vary the θ_j 's independently. It is always possible to find the quantum state of any single degree of freedom, corresponding to tracing out all other degrees of freedom. The limitation comes about when trying to find the joint quantum state of the N -dimensional system, in particular the correlations between the different degrees of freedom and entanglement. A simple illustration of this is offered by a two-dimensional harmonic oscillator with $\omega_1 = \omega_2 = \omega$. Let us consider measuring the observable $\hat{x}_1(\omega t)\hat{x}_2(\omega t)$. By using Eq. (2.2) we find:

$$\begin{aligned} \langle \hat{x}_1(\omega t)\hat{x}_2(\omega t) \rangle &= \langle [\cos(\omega t)\hat{x}_1 + \sin(\omega t)\hat{p}_1] [\cos(\omega t)\hat{x}_2 + \sin(\omega t)\hat{p}_2] \rangle \\ &= \cos^2(\omega t) \langle \hat{x}_1\hat{x}_2 \rangle + \sin^2(\omega t) \langle \hat{p}_1\hat{p}_2 \rangle + \\ &\quad \cos(\omega t) \sin(\omega t) \langle \hat{x}_1\hat{p}_2 + \hat{p}_1\hat{x}_2 \rangle. \end{aligned} \quad (2.8)$$

Here one can see that it is impossible by variation of t to find the moments $\langle \hat{x}_1\hat{p}_2 \rangle$ and $\langle \hat{p}_1\hat{x}_2 \rangle$ individually, even though one can find their sum. This means that even a simple two-dimensional Gaussian state cannot be reconstructed if $\omega_1 = \omega_2$, since one must know the first and second moments to completely specify such a state. In section 2.3.4 we shall give a precise method to identify which

correlations can be found from a certain set of data. Among other results we shall see that an N -dimensional Gaussian state can be completely reconstructed if no two ω_j 's are equal.

Let us return to the problem with Eq. (2.7): The θ_j 's are all varied through the one parameter t . The obvious solution to this problem is to devise some means to vary the θ_j 's independently. There are important situations where this is indeed possible for destructive measurements, e.g. the case of several entangled light fields. In this case a full reconstruction may be done, regardless of the values of the ω_j 's, as can be seen in Eq. (2.7). The independent variation of θ_j can here be achieved simply by delaying the measurement on the subsystems by introduction of a variable delay line or, in the case of homodyne measurements, by changing the phases or strengths of local oscillators [2], [11]-[13].

Another possibility for varying the θ_j 's independently would be to vary the times for the subsystems independently. For this purpose one might use a method closely analogous to the so-called "twin-paradox" from special relativity. For instance, imagine two spin-0 particles in each their one-dimensional harmonic oscillator. One may then leave the one subsystem undisturbed while the other is accelerated to a relativistic speed. This second subsystem is then allowed to fly along for a while, then accelerated back again towards the first subsystem and ultimately brought to rest in its original position. The time dilation will hereby delay the second subsystem compared to the first, effectively giving a means to independently vary the elapsed time for the two subsystems. To avoid direct disturbance of the second oscillator due to the acceleration, one should accelerate the system perpendicular to its direction of mechanical oscillation. In principle, this method of exercising control over the time of subsystems can also be used for more than two subsystems, but presumably with much increased practical complication. We note that the idea of relativistic time-displacement of subsystems has been suggested in [24] and recently applied to entanglement properties with highly non-trivial results [25].

2.3.2 Incommensurable frequencies

Returning to the general problem of full state reconstruction by (2.7), we shall discuss under what circumstances this is possible. By considering all times $t \geq 0$ and choosing the ω_j 's mutually incommensurable, i.e. their ratios are irrational numbers, we can find a unique t to reach any θ as long as θ_j/θ_k with $j \neq k$ is an irrational number. To see this, remember that $\theta_j = [\omega_j t]_\pi$, with $[\]_\pi$ being the modulus function with respect to π . The whole scheme can be pictured as letting N initially coinciding points move around a circle

with mutually incommensurable angular frequencies: If the points coincide at one angle (which we have chosen to be $\theta = 0$), then no pair will ever again coincide at this angle. The situation is illustrated for $N = 2$ in figure 2.1. A small technical detail in this respect is that since we have chosen the intervals of $0 \leq \theta_j < \pi$ and $-\infty < \eta_j, x_j < \infty$, then each time a θ_j surpasses an integer multiple of π we must let $\eta_j \rightarrow -\eta_j$ in Eq. (2.7).

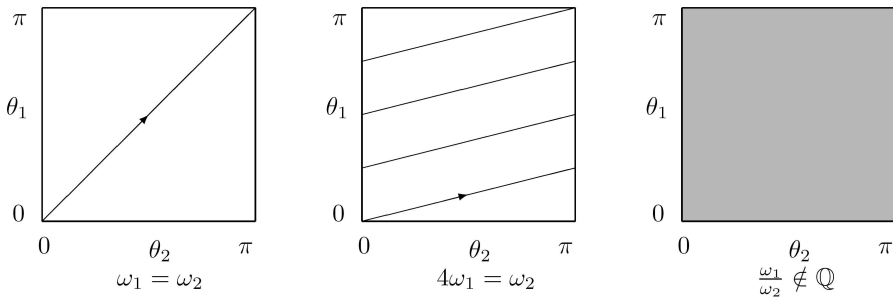


Figure 2.1: The figure illustrates the variation of $\theta_j = \omega_j t$ for the case of a two-dimensional harmonic oscillator. The graph to the left shows what values of (θ_1, θ_2) can be obtained for $\omega_1 = \omega_2$. More generally, if $\omega_1/\omega_2 = \alpha_1/\alpha_2$ is an irreducible fraction smaller than 1, there will be α_2 lines in the (θ_1, θ_2) -plane, as shown in the middle graph. Moreover, if ω_1/ω_2 is an irrational number, almost the whole (θ_1, θ_2) -plane will be covered as the measurement time $T' \rightarrow \infty$. The values of (θ_1, θ_2) not covered are all the values where θ_1/θ_2 is a rational number. Fortunately, it turns out we do not need this set of values to exactly reconstruct the quantum state.

Thus, we can find the function $\tilde{w}(\boldsymbol{\eta}, \boldsymbol{\theta})$ except on the values of $\boldsymbol{\theta}$ where two or more θ_j/θ_k , $j \neq k$ is a rational number. Fortunately, this non-available set of $\boldsymbol{\theta}$ values has measure zero, and since $\tilde{w}(\boldsymbol{\eta}, \boldsymbol{\theta})$ is uniformly continuous (and thereby non-singular), the inability to find $\tilde{w}(\boldsymbol{\eta}, \boldsymbol{\theta})$ on a set of measure zero is of no consequence. The uniform continuity of $\tilde{w}(\boldsymbol{\eta}, \boldsymbol{\theta})$ is a consequence of $\hat{\rho}$ belonging to the trace class [23].

The price we pay to gain knowledge of the N -dimensional state as compared to the one-dimensional case is that we must measure the joint position distribution of all coordinates for all times instead of just half of the oscillators' period. In actual applications, where infinite measurement times are not available, one would presumably use frequencies of the N oscillators whose ratios are rational

numbers and measure for the recurrence time of the joint system. The frequencies should then be chosen so that the $\boldsymbol{\theta}$ -space is sufficiently closely sampled for a reliable reconstruction. The exact amount of information obtained in such an experiment will be quantified in subsection 2.3.4.

It should also be noticed that this procedure is equally applicable to a quantum system comprised of several distinguishable non-interacting particles in separate harmonic potentials.

For completeness we give the formula for reconstruction of the N -dimensional Wigner function:

$$W(\mathbf{x}, \mathbf{p}) = \lim_{T' \rightarrow \infty} \frac{1}{2^N (2\pi)^N T'} \int_0^{T'} dt \int_{-\infty}^{\infty} d^N \boldsymbol{\eta} \int_{-\infty}^{\infty} d^N \mathbf{x}' \times \\ |\boldsymbol{\eta}| (-1)^{\sum_{j=1}^N F_j(t)} \Pr(\mathbf{x}', [\boldsymbol{\omega}t]_{\pi}) \times \\ \exp \left\{ i \sum_{j=1}^N (-1)^{F_j(t)} \eta_j [x_j - x'_j \cos([\omega_j t]_{\pi}) - p_j \sin([\omega_j t]_{\pi})] \right\},$$

where $F_j(t) = \text{Floor}(\omega_j t / \pi)$, and the Floor-function rounds downwards to the nearest integer.

2.3.3 An example of realizing incommensurable frequencies

In the above discussion, it was demonstrated that the quantum state of an N -dimensional harmonic oscillator could be exactly reconstructed if the N frequencies were incommensurable. It may be noticed that the reconstruction of the joint quantum state did not require interactions between the N degrees of freedom. We will now give a brief example of how it is possible, by introducing interactions between the oscillators, to reconstruct the full quantum state when the all frequencies are identical and equal to ω . We imagine the N oscillators arranged in a line, and introduce nearest-neighbor interaction terms in the Hamiltonian. We note that a very similar situation was recently considered for N trapped ions in connection with the construction of quantum gates [26].

Letting $\kappa \leq \omega$ be a real coupling constant, we have the Hamiltonian:

$$\hat{H} = \sum_{j=1}^N \hbar\omega \left(\hat{a}_j^\dagger \hat{a}_j + \frac{1}{2} \right) + \hat{H}_{int} \quad (2.9)$$

$$\hat{H}_{int} = \sum_{j=1}^N \hbar\kappa \left(\hat{a}_j^\dagger \hat{a}_{j+1} + \hat{a}_{j+1}^\dagger \hat{a}_j \right). \quad (2.10)$$

Arranging the N annihilation operators in a column vector $\mathbf{a} = (\hat{a}_1, \hat{a}_2, \dots, \hat{a}_N)^T$, we find from the Heisenberg equation of motion:

$$\frac{d}{dt} \begin{pmatrix} \hat{a}_1(t) \\ \hat{a}_2(t) \\ \vdots \\ \hat{a}_N(t) \end{pmatrix} = -i \underbrace{\begin{pmatrix} \omega & \kappa & 0 & \dots \\ \kappa & \omega & \kappa & \dots \\ 0 & \kappa & \omega & \dots \\ \vdots & \vdots & \vdots & \ddots \end{pmatrix}}_{\mathcal{D}} \begin{pmatrix} \hat{a}_1(t) \\ \hat{a}_2(t) \\ \vdots \\ \hat{a}_N(t) \end{pmatrix},$$

where the matrix \mathcal{D} is tri-diagonal and real. Since there are no terms containing \hat{a}_j^\dagger , we can perform a usual orthogonal diagonalization of this matrix to yield N new modes, characterized by new annihilation operators \hat{a}'_j . The eigenvalues ω'_j of \mathcal{D} are well-known from e.g. Hückel molecular orbital theory and solid-state physics:

$$\omega'_j = \omega + 2\kappa \cos \left(\frac{2j\pi}{N} \right), \quad j \in \{1, 2, \dots, N\}. \quad (2.11)$$

In this way, the new ladder operators have simple time evolutions $\hat{a}'_j(t) = \hat{a}'_j(0) \exp(-i\omega'_j t)$, and we can again find position operators $\hat{x}'_j(t) = 1/\sqrt{2}[\hat{a}'_j(t) + \hat{a}'_j{}^\dagger(t)]$. So if we choose κ so that the ω'_j 's are incommensurable, we can use the reconstruction method from subsection 2.3.2. Experimentally, one still has only to measure the \hat{x}_j 's since the \hat{x}'_j 's are merely linear combinations of these.

2.3.4 Commensurable frequencies and partial information

We have shown above that a complete tomographic reconstruction of the state of an N -dimensional quantum oscillator system is possible if all the oscillator angular frequencies are mutually incommensurable. This naturally leads to the question of which aspects of the quantum state can, and which cannot, be obtained from such tomographic measurements if some of the angular frequencies

are commensurable. We will seek to quantify this degree of information through the moments of the ladder operators \hat{a}_j and \hat{a}_j^\dagger , which have recently attracted attention in connection with characterization of entanglement [27]. For this to be meaningful, we must assume that these moments are finite. For convenience we shall be considering the Weyl-ordered (i.e. symmetrically ordered) products. Letting \mathbf{r} and \mathbf{s} be N -vectors with non-negative integer components, these moments of \hat{a}_j and \hat{a}_j^\dagger are generally of the form:

$$S(\mathbf{r}, \mathbf{s}) = \left\langle \prod_{j=1}^N \frac{r_j!}{s_j!(r_j - s_j)!} \left\{ (\hat{a}_j)^{s_j} (\hat{a}_j^\dagger)^{r_j - s_j} \right\}_0 \right\rangle, \\ \text{where } r_j \in \mathbb{N}_0 \text{ and } s_j \in \{0, 1, \dots, r_j\}. \quad (2.12)$$

That is, all factors in the product $S(\mathbf{r}, \mathbf{s})$ is the sum of all symmetric permutations of a number s_j of the operator \hat{a}_j and a number $(r_j - s_j)$ of the operator \hat{a}_j^\dagger . Here, $\{ \ }_0$ stands for the Weyl ordering, which is the same as the sum of all permutations divided by the number of terms. For example:

$$\{\hat{a}\hat{a}^\dagger\}_0 = \{\hat{a}^\dagger\hat{a}\}_0 = \frac{1}{2} (\hat{a}\hat{a}^\dagger + \hat{a}^\dagger\hat{a}).$$

A quantum state is completely characterized if all moments of the form in Eq. (2.12) are specified, provided they are finite. In this way we are recasting the question of to what extent the quantum state can be reconstructed into the question of how many of the moments $S(\mathbf{r}, \mathbf{s})$ can be found.

To keep things transparent, we shall initially consider only two oscillators with commensurable frequencies and only later generalize to the case of N oscillators. We shall need the recurrence time for the system, $T = 2\pi/\omega$ so that $\theta_j = \omega_j t = \alpha_j \omega t = \alpha_j \theta$, making α_j a positive integer. Since we are measuring the joint \mathbf{x} -distributions at different times, it is natural to consider moments of these distributions⁴ $\langle [\hat{x}_1(\theta_1)]^{r_1} [\hat{x}_2(\theta_2)]^{r_2} \rangle$. Recalling Eq. (2.2):

$$2^{\frac{r_1+r_2}{2}} \langle [\hat{x}_1(\theta_1)]^{r_1} [\hat{x}_2(\theta_2)]^{r_2} \rangle = 2^{\frac{r_1+r_2}{2}} \langle [\hat{x}_1(\alpha_1\theta)]^{r_1} [\hat{x}_2(\alpha_2\theta)]^{r_2} \rangle \\ = \left\langle \left(\hat{a}_1 e^{-i\alpha_1\theta} + \hat{a}_1^\dagger e^{i\alpha_1\theta} \right)^{r_1} \left(\hat{a}_2 e^{-i\alpha_2\theta} + \hat{a}_2^\dagger e^{i\alpha_2\theta} \right)^{r_2} \right\rangle \\ = \sum_{s_1=0}^{r_1} \sum_{s_2=0}^{r_2} S(r_1, r_2, s_1, s_2) e^{i\theta[\alpha_1(r_1-2s_1)+\alpha_2(r_2-2s_2)]}. \quad (2.13)$$

⁴Actually, no further information on the quantum state can be gained by considering other functions of the position distribution. This can be seen by expanding the function in its moments of the position operators, and realizing that the resulting equation is simply a linear combination of equations obtained in (2.13).

Since the set of functions $\{e^{in\theta}, n \in \mathbb{N}\}$ is linearly independent on the interval $[0; 2\pi[$ we can find all the moments $S(r_1, r_2, s_1, s_2)$ if there are no two of the exponential functions in the sum (2.13) that have the same period in θ . Indeed, to find all moments (and not only the symmetric ones) of order (r_1, r_2) , we must know all symmetric moments of this and lower order. A precise way to state this is that there must be no recurrences in the following lists, where we keep the r'_j 's fixed in each list and let the s'_j 's assume all possible values: $(\alpha_1[r'_1 - 2s'_1] + \alpha_2[r'_2 - 2s'_2])_{r'_j}$ with $r'_j \leq r_j$ and $s'_j \leq r'_j$. Finding these moments can then be done, for instance, by Fourier transformation since the aforementioned exponential functions are orthogonal.

Furthermore, one should notice that reconstructing the quantum state through the moments of the ladder operators, one in principle needs knowledge of only a small but finite interval of the angle θ , and not the whole interval $[0; \pi[$. A similar result is found in [28]. The fundamental assumption that allows for reconstruction from any small finite θ -interval is that of finiteness of the moments of the ladder operators and position operators in Eq. (2.13). The earlier discussed method of state reconstruction via Fourier transformation, (2.7), does not suffer from this limitation. On the other hand not all these moments need be finite, only the ones we use in the reconstruction.

Finally, one should notice that some of the moments can always be found, regardless of the value of α_1/α_2 . This trivially includes the moments $\langle \hat{x}_1^{r_1} \hat{x}_2^{r_2} \rangle$, since these are directly measured, but also the moments $\langle \hat{a}_1^{r_1} \hat{a}_2^{r_2} \rangle$ and their complex conjugates for any (r_1, r_2) since these moments evolve with the unique largest numerical frequency.

We proceed to discuss the practical usefulness of this approach to reconstruction. It is easy to realize that it is possible to find all moments with $r_1 < \alpha_2$ and/or $r_2 < \alpha_1$, so one may indeed settle for reconstructing moments of only low order, e.g. $r_1 + r_2 < \max(\alpha_1, \alpha_2)$. The reason for this is both the difficulty in precisely measuring higher moments of the joint position distribution and that finding higher moments of the ladder operators in general requires the ability to measure very rapid variations in the joint position distribution (see Eq. (2.13)). In addition, it is not necessary to measure a continuum of angles if one is only interested in moments up to a certain order, but only a number of angles equalling this number, which makes the procedure practically feasible. In this way one only has to solve a number of equations with an equal number of unknowns.

Generalizing the above results to arbitrary N , we let $T = 2\pi/\omega$ be the recurrence time of the system and $\theta_j = \alpha_j\theta$. The positive integers α_j are

arranged in an N -vector $\boldsymbol{\alpha}$, and we find that to reconstruct the moments up to $S(\mathbf{r}, \mathbf{s})$ one needs to measure $\left\langle \prod_{j=1}^N \hat{x}_j^{r_j}(\theta_j) \right\rangle$ and that there can be no recurring numbers in each of the lists (once more the r'_j 's are fixed in each list while s'_j assumes all possible values): $(\boldsymbol{\alpha} \cdot [\mathbf{r}' - 2\mathbf{s}'])_{\mathbf{r}'}$ with $r'_j \leq r_j$ and $s'_j \leq r'_j$. Like before, we can in particular always find all moments $\left\langle \prod_{j=1}^N \hat{x}_j^{r_j} \right\rangle$, since they are directly measured, and also $\left\langle \prod_{j=1}^N \hat{a}_j^{r_j} \right\rangle$ and its complex conjugate for all \mathbf{r} .

It is amusing to note that if all the moments of the ladder operators are finite and the angular frequencies are incommensurable, it is in principle possible to reconstruct the full quantum state from measurements made in a small but finite time interval regardless of the dimension N – an impossible task if just two angular frequencies are commensurable.

One may also remark that an N -dimensional Gaussian state can always be completely reconstructed if no two ω_j 's are equal: The required measurements are the joint position distribution for either 4 points of time or any finite continuous interval of time.

Lastly, we make a brief comment on a possible strategy for guessing the quantum state in the case of commensurable frequencies, i.e. estimation rather than reconstruction. Even though we do not know the moments of the ladder operators individually, we still find the sum of two or more – the exact number is determined by the how many occurrences there are of a particular number in the aforementioned lists. One method of guessing the state from an incomplete set of data is the Maximum Entropy Principle, due to Jaynes [29], which has been used in several reconstruction schemes [8], [30], and will be the topic of chapter 5. The Maximum Entropy principle says that in case one has a set of data which could have come about due to several different quantum states, one should choose the state with the largest entropy. In our present scenario, this means that if we only know the sum of, say, $n_{\mathbf{r}, \mathbf{s}}$ different symmetric moments, the Maximum Entropy principle would ascribe equal Lagrange multipliers to each observable in the Maximum Entropy density operator.

2.4 The free particle

The tomographic reconstruction of the free particle on an unbounded axis has been considered in [21], but as stated herein, cannot be used beyond the one-dimensional case. The very general treatment of time-independent problems in [7] is also restricted to one dimension. Here, we instead study the semi-

continuous case of the free particle with different boundary conditions. In the first two subsections 2.4.1 and 2.4.2, we shall study the free particle with periodic boundary conditions, also valid for the planar rotor⁵. In the last subsection 2.4.3 we shall give a brief treatment of the particle in a box where it will be seen that the different boundary condition has an important effect on the available information.

2.4.1 The one-dimensional case

As in the case of the oscillator, we shall first treat the one-dimensional case and later extend this to N dimensions. In the present case the reconstruction of the quantum state will be done through finding the matrix elements of $\hat{\rho}$ by simple inversion of Fourier transforms used in [21]. Let us consider a particle with mass m on the spatial interval $0 \leq x < L$. The Hamiltonian is $\hat{H} = \hat{p}^2/2m$, yielding the eigenstates $|n\rangle$ with energy $E(n) = \hbar\Omega n^2$. Here $\Omega = \pi\hbar/mL^2$ and \hbar is Planck's constant. The eigenstate $|n\rangle$ in the x -representation is:

$$\langle x|n\rangle_t = \frac{1}{\sqrt{L}} e^{2\pi i n x/L} e^{-i\Omega n^2 t}. \quad (2.14)$$

We can use this to find the position distribution at any time:

$$\begin{aligned} \text{Pr}(x, t) &= {}_t \langle x|\hat{\rho}|x\rangle_t \\ &= \sum_{n, n'=-\infty}^{\infty} {}_t \langle x|n\rangle \langle n|\hat{\rho}|n'\rangle \langle n'|x\rangle_t \\ &= \sum_{n, n'=-\infty}^{\infty} \rho(n, n') \frac{1}{L} e^{2\pi i(n-n')x/L} e^{-i\Omega(n^2-n'^2)t}. \end{aligned} \quad (2.15)$$

It will be convenient to change variables from n and n' to $\bar{n} = n+n'$, $\Delta n = n-n'$. Note that \bar{n} and Δn are both either even or odd. Changing summation variables in this manner yields:

$$\begin{aligned} \text{Pr}(x, t) &= \frac{1}{L} \left(\sum_{\substack{\bar{n}=-\infty \\ \text{even}}}^{\infty} \sum_{\substack{\Delta n=-\infty \\ \text{even}}}^{\infty} + \sum_{\substack{\bar{n}=-\infty \\ \text{odd}}}^{\infty} \sum_{\substack{\Delta n=-\infty \\ \text{odd}}}^{\infty} \right) \times \\ &\quad \rho\left(\frac{\bar{n} + \Delta n}{2}, \frac{\bar{n} - \Delta n}{2}\right) e^{2\pi i \Delta n x/L} e^{-i\Omega \bar{n} \Delta n t}. \end{aligned} \quad (2.16)$$

⁵For the rotor, one must substitute $ma^2 \rightarrow \mathcal{I}$, where \mathcal{I} is the moment of inertia and ma^2 is defined in subsection 2.4.1.

Our task is to invert this equation to find the matrix elements of $\hat{\rho}$. Fortunately, this is quite easy. Notice that there are two exponential functions in Eq. (2.16) and both can be used with a Fourier transformation to pick out certain values of \bar{n} and Δn : The first exponential function in x contains only Δn and once Δn is fixed, the other exponential function in t can be used to select \bar{n} . In order to show how this works, we let $N_T \in \mathbb{N}$ and $2T = 2\pi/\Omega$ be the minimum required measurement time, which corresponds to twice the time a classical particle with the lowest non-zero energy ($n = 1$) would take to traverse the length L . For any integers ν and $\beta \neq 0$ of the same parity, we form the appropriate Fourier Transforms of Eq. (2.16) to obtain:

$$\begin{aligned}
& \int_0^L dx e^{-2\pi i \beta x/L} \frac{1}{2N_T T} \int_{-N_T T}^{N_T T} dt e^{i\Omega \nu \beta t} \text{Pr}(x, t) = \\
& \frac{1}{2N_T T} \int_{-N_T T}^{N_T T} dt \sum_{\substack{\bar{n}=-\infty \\ \text{parity as } \beta}}^{\infty} \rho\left(\frac{\bar{n} + \beta}{2}, \frac{\bar{n} - \beta}{2}\right) e^{i\Omega(\nu - \bar{n})\beta t} = \\
& \sum_{\substack{\bar{n}=-\infty \\ \text{parity as } \beta}}^{\infty} \rho\left(\frac{\bar{n} + \beta}{2}, \frac{\bar{n} - \beta}{2}\right) \delta_{\nu, \bar{n}} = \\
& \rho\left(\frac{\nu + \beta}{2}, \frac{\nu - \beta}{2}\right) \quad \begin{array}{l} \beta \text{ and } \nu \text{ of} \\ \text{same parity.} \end{array} \tag{2.17}
\end{aligned}$$

We have found all elements of the density matrix except those for which $\beta = 0$, i.e. the diagonal in the (momentum) n -representation. If we were to choose $\beta = 0$, we would always obtain the result of unity in Eq. (2.17), as this is the same as taking the trace of $\hat{\rho}$ in the x -basis. This inability to find the diagonal was also pointed out for finite observation times for the free particle on an unbounded axis in [21], and will unfortunately carry over to the multidimensional case. This limitation arises because all probability densities of the eigenstates are identical: $|\langle x|n\rangle|^2 = 1/L$ whereby, for example, a thermal state and any pure eigenstate $|n\rangle\langle n|$ have the same probability distribution at all times. Even though finding the diagonal of a density matrix is impossible given the rest of the matrix, one can use the Schwartz inequality to constrain the size of the diagonal elements through $|\rho(n, n')|^2 \leq \rho(n, n)\rho(n', n')$.

2.4.2 N -dimensional free particle with periodic boundary conditions

We will now move on to the N -dimensional case, that is to say a single particle in N spatial dimensions, the combined state of N particles in one dimension each, or a combination yielding a total of N dimensions. We shall work in the N -dimensional interval $x_j \in [0, L_j]$. The energies of the eigenstates are $E(\mathbf{n}) = \hbar \sum_{j=1}^N \Omega_j n_j^2$ and in extension of Eq. (2.16) we introduce the N -vectors of intergers $\bar{\mathbf{n}}$ and $\Delta \mathbf{n}$. This yields:

$$\begin{aligned} \Pr(\mathbf{x}, t) = & \left[\prod_{j=1}^N \left(\sum_{\substack{\bar{n}_j \\ \text{even}}} \sum_{\substack{\Delta n_j \\ \text{even}}} + \sum_{\substack{\bar{n}_j \\ \text{odd}}} \sum_{\substack{\Delta n_j \\ \text{odd}}} \right) \frac{1}{L_j} e^{2\pi i \Delta n_j x_j / L_j} e^{-i \Omega_j \bar{n}_j \Delta n_j t} \right] \\ & \times \rho \left(\frac{\bar{\mathbf{n}} + \Delta \mathbf{n}}{2}, \frac{\bar{\mathbf{n}} - \Delta \mathbf{n}}{2} \right). \end{aligned} \quad (2.18)$$

We shall try to invert this equation to find the matrix elements of $\hat{\rho}$. Of course, we cannot approach this completely as in the one-dimensional case and select a particular vector $\bar{\mathbf{n}}$ through Fourier-transforms, having only the parameter t to vary. We can, however, expand the time interval of integration to incorporate all points of time:

$$\lim_{T'' \rightarrow \infty} \frac{1}{2T''} \int_{-T''}^{T''} dt e^{i \sum_{j=1}^N \Omega_j (\nu_j - \bar{n}_j) \beta_j t} = \delta_{\sum_{j=1}^N \Omega_j (\nu_j - \bar{n}_j) \beta_j, 0}. \quad (2.19)$$

If the Ω_j 's are mutually incommensurable, the only possibility for this Kronecker delta-function to give a non-zero result is for $\nu_j = \bar{n}_j \forall j$. Remembering that $\Omega_j = \frac{\pi \hbar}{m_j L_j^2}$, the condition of incommensurability of the Ω_j 's is equivalent to demanding the elements of the list:

$$(m_j L_j^2) \quad \text{be incommensurable}$$

In this way it becomes possible for a single delta-function to effectively serve as N distinct delta-functions. We shall henceforth make this requirement of incommensurability of the Ω_j 's and, as in the one-dimensional case, we only obtain useful results for $\beta_j \neq 0$. With these limitations we can exactly reconstruct the rest of the density matrix. Additionally, β_j and \bar{n}_j have the same parity for

all j :

$$\rho\left(\frac{\nu + \beta}{2}, \frac{\nu - \beta}{2}\right) = \lim_{T'' \rightarrow \infty} \frac{1}{2T''} \int_{-T''}^{T''} dt \int_{\mathbf{0}}^L d^N \mathbf{x} e^{-2\pi i \sum_{j=1}^N \beta_j x_j / L_j} \times e^{i \sum_{j=1}^N \Omega_j \nu_j \beta_j t} \text{Pr}(\mathbf{x}, t). \quad (2.20)$$

The special feature of this system, which allows the treatment above, is that all its eigen-energies are rational numbers (actually integers) times some minimum energy. This can in fortunate circumstances, i.e. if the products of the energy eigenstates in the position representation are reasonably placid, allow state reconstruction equations like that in Eq. (2.17). These reconstruction equations will make use of a finite measurement time, and by using the trick in Eq. (2.19), can be used in multiple dimensions. Another example of this kind of system is the quantum mechanical rotor with fixed angular momentum projection, which is the topic of chapter 3.

2.4.3 Particle in a box

In the last two subsections we found ourselves unable to determine the momentum distribution for the free particle with periodic boundary conditions. The reason for this was that all the energy eigenstates of the system had the same spatial distribution. In this subsection we shall show how imposing other boundary conditions can completely alter this situation. In particular, we shall study the particle in a box, where the spatial density is zero at the boundaries of the box. As usual, we shall first treat the one-dimensional case and later move on to the N -dimensional case.

We choose $x \in [0, L]$ whereby $E(n) = \hbar\Omega'n^2$, now with $n \in \mathbb{N}$. We use $\Omega' = \Omega/4 = \frac{\pi\hbar}{4mL^2}$, yielding the energy eigenstates:

$$\langle x|n\rangle_t = \sqrt{\frac{2}{L}} \sin\left(n\frac{\pi x}{L}\right) e^{-i\Omega't}.$$

These eigenstates all have different spatial distributions, and we already suspect that we shall be able to reconstruct the momentum distribution. Following

section 2.4.2 we find the joint position distribution, similar to Eq. (2.15):

$$\begin{aligned} \Pr(x, t) &= {}_t\langle x | \hat{\rho} | x \rangle_t \\ &= \sum_{n, n'=1}^{\infty} \rho(n, n') \frac{2}{L} \sin\left(n \frac{\pi x}{L}\right) \sin\left(n' \frac{\pi x}{L}\right) e^{-i\Omega'(n^2 - n'^2)t} \\ &= \frac{1}{L} \sum_{n, n'=1}^{\infty} \rho(n, n') \left\{ \cos\left[(n - n') \frac{\pi x}{L}\right] - \cos\left[(n + n') \frac{\pi x}{L}\right] \right\} e^{-i\Omega(n^2 - n'^2)t}. \end{aligned}$$

Making once more the substitution $\bar{n} = n + n'$ and $\Delta n = n - n'$ we arrive at the box equivalent of Eq. (2.16):

$$\begin{aligned} \Pr(x, t) &= \frac{1}{L} \left(\sum_{\substack{\bar{n}=0 \\ \text{even}}}^{\infty} \sum_{\substack{\Delta n = -\bar{n}+1 \\ \text{even}}}^{\bar{n}-1} + \sum_{\substack{\bar{n}=1 \\ \text{odd}}}^{\infty} \sum_{\substack{\Delta n = -\bar{n}+1 \\ \text{odd}}}^{\bar{n}-1} \right) \rho\left(\frac{\bar{n} + \Delta n}{2}, \frac{\bar{n} - \Delta n}{2}\right) \\ &\quad \times \left[\cos\left(\Delta n \frac{\pi x}{L}\right) - \cos\left(\bar{n} \frac{\pi x}{L}\right) \right] e^{-i\Omega \bar{n} \Delta n t}. \end{aligned} \quad (2.21)$$

Recalling that the set of functions $\{\cos(k\pi x/L)\}$, $k \in \mathbb{N}$, is orthogonal on $x \in [0, L]$ we can use the cosine functions in Eq. (2.21) and the exponential function in time to select a certain term in the sum. Selecting $\nu \in \mathbb{N}$ and $\beta \in \mathbb{Z}$ with $\nu > |\beta|$ and letting $T' = 2\pi/\Omega'$ we obtain the equivalent of Eq. (2.17)⁶:

$$\begin{aligned} \rho\left(\frac{\nu + \beta}{2}, \frac{\nu - \beta}{2}\right) &= 2 \int_0^L dx \cos\left(\beta \frac{\pi x}{L}\right) \times \\ &\quad \frac{1}{2N_T T'} \int_{-N_T T'}^{N_T T'} dt e^{i\Omega' \nu \beta t} \Pr(x, t), \quad \nu > |\beta|. \end{aligned} \quad (2.22)$$

Here it is apparent that we can reconstruct the full density matrix, including the momentum distribution. Thus, the choice of boundary conditions has allowed us to overcome the limitation encountered in the case of periodic boundary conditions. Later on, in chapter 3, boundary conditions will similarly allow us to reconstruct diagonal elements of the density operator for a rotor; elements hidden in the case of section 2.4.2⁷.

⁶Performing the necessary sums, it is easiest to let the sums extend over all positive and negative \bar{n} and Δn (each sum containing only even or odd indices) and then in the end set all $\rho(n, n') = 0$ if $n \leq 0$ or $n' \leq 0$.

⁷Specifically, chapter 3 uses a spherical coordinate space given by the spherical polar angles (θ, ϕ) , rather than the toroidal one given by the periodic boundary conditions in subsection 2.4.2.

Moving on to the multidimensional case where $E(\mathbf{n}) = \hbar \sum_{j=1}^N \Omega'_j n_j^2$ we find the equivalent of Eq. (2.18):

$$\begin{aligned} \Pr(\mathbf{x}, t) = & \left\{ \prod_{j=1}^N \left(\sum_{\substack{\bar{n}_j=0 \\ \text{even}}}^{\infty} \sum_{\substack{\Delta n_j = \\ -\bar{n}_j+1 \\ \text{even}}}^{\bar{n}_j-1} + \sum_{\substack{\bar{n}_j=1 \\ \text{odd}}}^{\infty} \sum_{\substack{\Delta n_j = \\ \bar{n}_j-1 \\ \text{odd}}}^{\bar{n}_j-1} \right) \times \right. \\ & \left. \frac{1}{L_j} \left[\cos \left(\Delta n_j \frac{\pi x_j}{L_j} \right) - \cos \left(\bar{n}_j \frac{\pi x_j}{L_j} \right) \right] e^{-i\Omega_j \bar{n}_j \Delta n_j t} \right\} \times \\ & \rho \left(\frac{\bar{\mathbf{n}} + \Delta \mathbf{n}}{2}, \frac{\bar{\mathbf{n}} - \Delta \mathbf{n}}{2} \right). \end{aligned} \quad (2.23)$$

Selecting the two N -vectors $\boldsymbol{\nu}$ and $\boldsymbol{\beta}$ with $\nu_j > |\beta_j|$ and demanding incommensurability of the elements in the list $(m_j L_j^2)$, we find the reconstruction formula corresponding to (2.20):

$$\begin{aligned} \rho \left(\frac{\boldsymbol{\nu} + \boldsymbol{\beta}}{2}, \frac{\boldsymbol{\nu} - \boldsymbol{\beta}}{2} \right) = & \lim_{T'' \rightarrow \infty} \frac{1}{2T''} \int_{-T''}^{T''} dt \int_{\mathbf{0}}^{\mathbf{L}} d^N \mathbf{x} \left[\prod_{j=1}^N \cos \left(\beta_j \frac{\pi x_j}{L_j} \right) \right] \times \\ & e^{i \sum_{j=1}^N \Omega'_j \nu_j \beta_j t} \Pr(\mathbf{x}, t), \quad \nu_j > |\beta_j|. \end{aligned} \quad (2.24)$$

As in the one-dimensional particle in a box, it is in the multidimensional case possible to completely reconstruct the density matrix.

2.5 Summary

We have shown how to extend two common schemes of quantum state tomography from one to N dimensions: The harmonic oscillator and the free particle on a finite interval. We have assumed that the time of the N subsystems cannot be varied independently and that the Hamiltonian is time-independent. In both cases a complete reconstruction required extension of the time interval of observation to all times and required incommensurability of the eigen-energy differences for the different N spatial dimensions.

For the harmonic oscillator, we quantified the information that can be reconstructed if some of the N frequencies are commensurable. This was done by reconstructing the moments of the ladder operators. This partial reconstruction only required measurements at a finite number of points of time.

For the free particle on a finite interval we showed that all off-diagonal elements of the density matrix in the energy-representation can be reconstructed in the case of periodic boundary conditions, and that a full reconstruction is possible for the box potential

In a more general perspective, the oscillators with commensurable frequencies, and the free particle with periodic or box-like boundary conditions, both illustrate more fundamental aspects of state reconstruction, and we imagine that further analyses along the lines of the current work may serve to identify the conditions imposed on dynamical laws such that quantum states can be generally reconstructed, as suggested in the conclusion of [7].

Chapter 3

Molecular rotational states

3.1 Synopsis

In this chapter, we will investigate the reconstruction of rotational states of molecules from measurements of their angular distribution at different points of time. For this purpose, we take our starting point in a widespread experimental situation for non-adiabatic alignment of molecules. We show both that sufficient information for complete reconstruction may be obtained with a small modification of the usual experiment, and present an analytical reconstruction method.

The chapter is based on the article [31].

3.2 Introduction

Molecular alignment refers to aligning an axis of the molecule along a fixed axis in the laboratory. In contrast to orientation where molecules point in a certain direction (e.g. up), alignment only fixes an axis allowing molecules to be oriented two opposite ways (e.g. up or down). To cause this alignment, the usual method is applying a laser pulse to a molecular gas, interacting non-resonantly with the molecules through their polarizability. For aligning laser pulses with intensity envelopes changing slowly compared to the molecule's rotational transition frequencies, the field free rotational states evolve adiabatically into the so-called pendular states [32]. In contrast, we shall be exclusively interested in field-free alignment which is inherently a non-adiabatic effect. Since its first experimen-

tal demonstration in 2001 [33]-[34], non-adiabatic alignment of molecules using short non-resonant laser pulses has spurred great interest, finding application in ultra-fast optics, high harmonic generation, scattering theory and potentially in electronic state tomography [35]. A recent review can be found in [36].

Non-adiabatic alignment can be achieved through using a short laser pulse, usually lasting somewhere between a few picoseconds down to tens of femtoseconds, to give the molecules an angular “kick” which serves to align them after the pulse has passed. Before we delve into the quantum mechanics, we illustrate this effect with a brief classical treatment. Specifically, we consider the rigid diatomic molecule in Fig. 3.1 whose internuclear axis is at an angle θ to the fixed polarization vector \mathbf{n}_z of a laser field, defining the z -axis.

Resolving the laser field in the molecular (X,Y,Z)-coordinates, we find the dipole moment $\mathbf{p}(t)$ in the molecular frame, induced by the electric field $\mathcal{E}(t) = \mathcal{E}(t)\mathbf{n}_z$:

$$\mathbf{p}(t) = \begin{pmatrix} \alpha_{\perp} & & \\ & \alpha_{\perp} & \\ & & \alpha_{\parallel} \end{pmatrix} \begin{pmatrix} 0 \\ -\mathcal{E}(t)\sin(\theta) \\ \mathcal{E}(t)\cos(\theta) \end{pmatrix} = \begin{pmatrix} 0 \\ -\mathcal{E}(t)\alpha_{\perp}\sin(\theta) \\ \mathcal{E}(t)\alpha_{\parallel}\cos(\theta) \end{pmatrix},$$

where α_{\parallel} and α_{\perp} are the polarizabilities along and perpendicular to the molecular axis. The resulting torque is:

$$\boldsymbol{\tau}(t) = \mathbf{p}(t) \times \mathcal{E}(t) = \mathcal{E}(t)^2(\alpha_{\parallel} - \alpha_{\perp})\sin(2\theta)\mathbf{n}_x, \quad (3.1)$$

where \mathbf{n}_x is a unit vector in the positive x -direction. Four observations can be made: First, the torque is proportional to the intensity, and thus independent of the sign of $\mathcal{E}(t)$. Second, in the usual case where $\alpha_{\parallel} > \alpha_{\perp}$, the torque gives the molecules an angular momentum tending to rotate them directly towards alignment with the polarization axis. Third, for small numeric angles $|\theta| \ll 1$, we find $\tau \propto \theta$. Fourth and finally, if the laser pulse only has nonzero intensity for a time so short that θ can be considered fixed, one can find the angular velocity $\boldsymbol{\omega}$ given to the molecule by the field:

$$\boldsymbol{\omega} = \int dt \frac{\boldsymbol{\tau}(t)}{\mathcal{I}} \approx \left[2 \frac{\alpha_{\parallel} - \alpha_{\perp}}{\mathcal{I}} \int dt \mathcal{E}(t)^2 \right] \theta \mathbf{n}_x. \quad (3.2)$$

Since we have for small angles $\boldsymbol{\omega} \propto \theta \mathbf{n}_x$, an ensemble of molecules starting out with different small θ and negligible initial angular velocities will all reach $\theta = 0$ at the same time $\mathcal{I} / [2(\alpha_{\parallel} - \alpha_{\perp}) \int dt \mathcal{E}(t)^2]$ after the passage of the laser pulse. By symmetry, a similar argument can be made for $|\theta - \pi| \ll 1$. Taking into account the values of θ that are not close to either 0 or π , initial angular

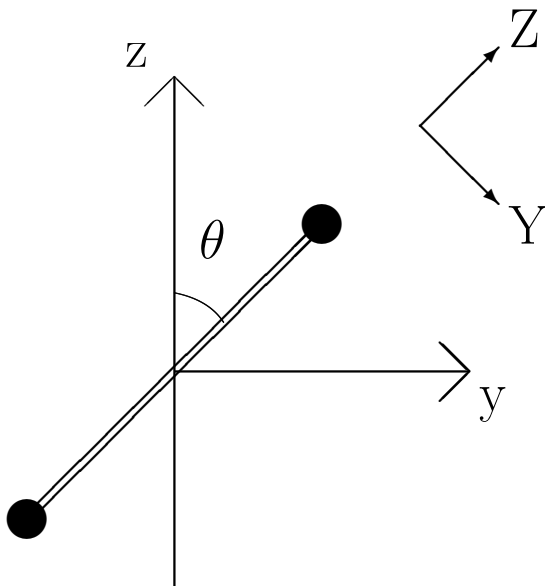


Figure 3.1: Molecule in a laser field shows alignment using classical arguments. The molecular axis has an initial angle θ to the z -axis, along which the laser field is polarized. The molecular axes (Y,Z) are also shown, and the two axes x and X are coincident. The polarizability matrix is diagonal in the (X,Y,Z)-basis and reads $\underline{\alpha} = \text{diag}(\alpha_{\perp}, \alpha_{\perp}, \alpha_{\parallel})$. For small angles θ and short laser pulses, the angular velocity given to the molecules by the laser field $|\omega| \propto \theta$ effecting that all such molecules align with the z -axis at the same instant of time.

velocities and the finite time of the laser pulse, perfect alignment will usually not be obtained in a realistic ensemble. There will instead be a short time interval, after the passage of the laser pulse, during which most molecules in the ensemble will be approximately aligned along the laser's polarization axis.

Having a classical grasp of alignment, we shall leave this treatment behind and move on to the quantum mechanical model. This is necessary for a precise description of the state due to the tiny size of the molecules, and carries with it non-classical phenomena such as rotational revivals.

3.3 A typical alignment experiment

A typical example of an alignment experiment is shown in figure 3.2. Here, a supersonic molecular beam is used as the molecular system in a pump-probe experiment. Such beams are formed by throttle-like expansions through a small valve, usually together with a background noble gas, and has the advantage of rotationally cooling the molecules to temperatures of a few Kelvin. While this temperature is low compared to standard conditions, it is still high enough to appreciably populate more than one rotational level in molecules used in alignment experiments. The initial state is thus approximately a thermal state with a few energy levels excited. The pump is a short (typically a few ps), intense non-resonant laser pulse, which induces the rotational state. The pump pulse is linearly polarized and since the initial state is thermal and therefore rotationally symmetric, the rotational state formed will be cylindrically symmetric around the pump polarization axis. Furthermore, because the field mainly interacts with the molecule through the molecular polarizability, the rotational state is reflection symmetric in a plane orthogonal to the pump polarization. Whereas the cylindrical symmetry is critical to our treatment, the reflection symmetry is not required.

After a delay, the molecules are Coulomb-exploded by an intense ultrashort probe-pulse, polarized parallel to the pump pulse, and with a duration of typically a few tens of femtoseconds. This time and the subsequent dissociation passes so quickly that simultaneous rotations can be neglected. The molecular fragments therefore recoil approximately back-to-back and their angular distribution can be found from the imaged fragments [37], [38]. Because of the cylindrical symmetry, the true angular distribution can be found even though the fragments are pulled by an electric field towards a detection plane containing the laser polarizations [39]. In a future work, we will show that one can easily use the raw data for the Quantum State Reconstruction, without the numerical errors introduced by the commonly used mathematical technique of Abel inversion [40]. For the moment, however, we can think of having the true angular distribution at our disposal.

So far, the comparison of such experiments with theory has been through the resemblance of experimental data with numerical simulations of the time evolution from a known initial state. Conversely, we propose a tomographic method by which one can determine an unknown quantum rotational state of a linear and symmetric top rotor from measurements of the angular distributions at several points of time. Apart from giving explicit reconstruction formulas, we also show that the full quantum state information is present in these measure-

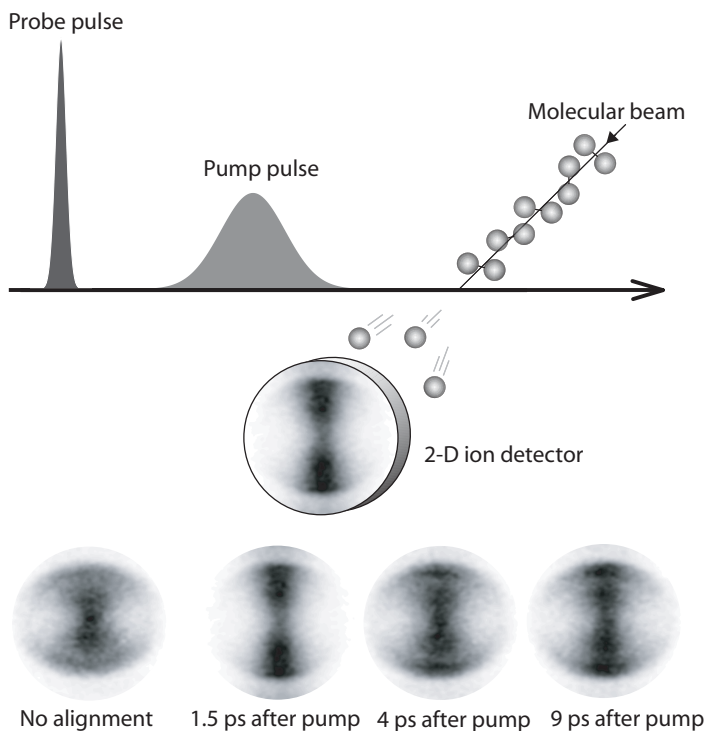


Figure 3.2: A typical non-adiabatic alignment experiment with short laser pulses. The initially cool molecules are excited into a rotational state by a non-resonant, vertically polarized pump pulse. After a time t the molecules are Coulomb-exploded with an intense, ultrashort probe pulse, also vertically polarized. The fragments recoil back-to-back and are imaged on a 2-D detector. The 3-D angular distributions can be found from these 2-D images by Abel inversion because of the cylindrical symmetry. Four examples of experimental data with Iodobenzene are shown for illustration, the imaged fragments being iodine ions: (from left) Probe applied long before pump, probe applied after respectively 1.5, 4 and 9ps. Part of the anisotropy, apparent in the un-aligned case, is due to the Coulomb-explosion preferentially occurring parallel to the probe polarization. This is corrected for when finding the 3-D distribution. Strictly speaking, Iodobenzene is an asymmetric top, but only slightly. For many purposes, it behaves like a symmetric top. Illustrative experimental data kindly provided by Simon S. Viftrup.

ments, which may be useful in the development of approximate reconstruction methods.

This chapter is arranged as follows: In section 3.4 we present the tomographic method for the rigid linear rotor. In section 3.5 we show how to extend the tomographic method to molecules where centrifugal distortion must be taken into account. In section 3.6 we extend the tomographic method to the case of symmetric top molecules. In section 3.7 we discuss the possibilities of recording the experimental data necessary to perform a reconstruction and we conclude the chapter.

3.4 Reconstruction method for linear molecules

In this section we will present a reconstruction method by which one can find the rotational state of a linear rigid rotor. Specifically, we imagine that we are able to perform measurements of spatial distributions at different points of time and that we know the Hamiltonian governing the time evolution. The goal shall be to find the unique quantum state corresponding to these measurements.

3.4.1 Free rotation

Before discussing the description of the quantum state, we shall first digress to account for what we know about the Hamiltonian and its eigenstates. As discussed in the introduction, we are varying the time elapsed between when the rotational state is created by a pump pulse and when it is probed. During this time the molecule is in a field-free environment. Consequently, we shall be interested in the Hamiltonian for the free rotor.

The Hamiltonian governing the time evolution for the linear rotor with moment of inertia \mathcal{I} is:

$$\hat{H} = \frac{\hat{\mathbf{J}}^2}{2\mathcal{I}},$$

where $\hat{\mathbf{J}}$ is the angular momentum operator. The energy eigenstates of this Hamiltonian are $\{|J, m\rangle\}$ where the angular momentum quantum number $J \in \mathbb{N}_0$ and the projection quantum number $m \in \{-J, -J+1, \dots, J\}$. These states have energy $E_J = \hbar\Omega J(J+1)$, where $\Omega = \frac{\hbar}{2\mathcal{I}}$. Since we will reconstruct the quantum state using angular distribution measurements only, we shall need the spatial coordinate representation of the energy eigenstates. As stated above, we shall restrict our study to azimuthally symmetric distributions, and we shall

hence be interested in the distribution of the polar angle θ . For notational simplicity, we shall use the parameter $x = \cos(\theta)$ so the position representation of the eigenstates becomes:

$${}_t\langle x|J, m\rangle = \mathcal{P}_J^{|m|}(x) e^{-i\Omega J(J+1)t}. \quad (3.3)$$

There should be a factor of $e^{im\phi}$ in Eq. (3.3), with ϕ being the azimuthal angle, but we can safely ignore this since we shall restrict our treatment to fixed values of m : Any phase factor will disappear when multiplied with the complex conjugate in Eq. (3.5) below. Another way to look at this is that since we assume azimuthal symmetry of the angular distributions, we might as well evaluate the position distribution at the azimuthal angle $\phi = 0$. The $\mathcal{P}_J^{|m|}$ are the normalized associated Legendre functions, normalized on $x \in [-1, 1]$ [41]:

$$\int_{-1}^1 dx \mathcal{P}_{J_1}^{|m|}(x) \mathcal{P}_{J_2}^{|m|}(x) = \delta_{J_1, J_2}. \quad (3.4)$$

The multiplicative factors relating these to the un-normalized associated Legendre functions $P_J^{|m|}(x)$ are:

$$\mathcal{P}_J^{|m|}(x) = \sqrt{\frac{2J+1}{2} \frac{(J-m)!}{(J+m)!}} P_J^{|m|}(x).$$

Equation (3.3) fully accounts for the free time evolution of the rotor. The angular position distribution of a single eigenstate is constant in time, but due to the different time dependent phase factors, a linear combination of different $|J, m\rangle$ states will have time dependent interference terms. Hence, such a linear combination will have a time dependent position distribution, also in the field free case.

After this brief account of the dynamics of the system, we proceed to define what we mean by the quantum state we are trying to reconstruct.

In the present treatment, the state will be characterized by its density operator $\hat{\rho}$, allowing a description of statistically mixed states. Specifically, we shall find all the matrix elements of $\hat{\rho}$ in the $|J, m\rangle$ -basis at $t = 0$ restricted to single m 's. This is the same as finding the diagonal blocks of constant m in the density matrix, i.e. $\rho(J, m, J', m) = \rho_m(J, J')$. For a general state this is only a partial characterization, but if it is somehow known that the state has no correlations between different m values, knowledge of all $\rho_m(J, J')$ amounts to a full characterization of the state. This is the case in the experiment described in the introduction, the reason being that the initial thermal state and all Hamiltonians causing dynamics in the system have this symmetry. The procedure

below will completely reconstruct the quantum state for such systems. For the angular distribution, this diagonality in m implies cylindrical symmetry for all time around a laboratory fixed axis, which we choose to be a spherical polar axis. Please note that we assume for the moment that measurements of the angular distribution can be performed for a single m index. That is, a full reconstruction would require a separate measurement for each m . We will return to the practical realizability of such measurements in section 3.7.

There are several reasons why it is necessary to use the density matrix to describe the system's state rather than the wave-function (i.e. a state vector). The first reason for this is that the initial state, before excitation with the pump pulse, is a thermal state with more than one rotational level populated. Furthermore, the pump pulse intensity will vary across its focus, whereby molecules at different points of space will experience different pulse strengths. Thus, even if the initial state had been pure, molecules in different parts of the focus will be evolved with different Hamiltonians, creating a mixed state. Consequently, we choose to describe the system's quantum state by its density matrix which is a complete characterization of the quantum state in this case, much as the wave-function is in the case of pure states.

3.4.2 Measurements and observables

Having described the physical system, we proceed to consider the measurements performed; namely the (angular) position distributions for a fixed m at the time t :

$$\begin{aligned}
 \text{Pr}(x, t) &= {}_t\langle x | \hat{\rho}_m | x \rangle_t \\
 &= \sum_{J_1=|m|}^{\infty} \sum_{J_2=|m|}^{\infty} {}_t\langle x | J_1, m \rangle \langle J_1, m | \hat{\rho}_m | J_2, m \rangle \langle J_2, m | x \rangle_t \\
 &= \sum_{J_1=|m|}^{\infty} \sum_{J_2=|m|}^{\infty} \rho_m(J_1, J_2) \mathcal{P}_{J_1}^{|m|}(x) \mathcal{P}_{J_2}^{|m|}(x) \times \\
 &\quad e^{-i\Omega[J_1(J_1+1) - J_2(J_2+1)]t}, \tag{3.5}
 \end{aligned}$$

where $t = 0$ is an arbitrary, but fixed, point of time after passage of the pump pulse. Our aim is to invert this equation to find the density matrix in the eigenstate-representation $\rho_m(J_1, J_2)$. It will prove convenient to write the products of the two Legendre functions $\mathcal{P}_{J_1}^{|m|}(x) \mathcal{P}_{J_2}^{|m|}(x)$ as a sum of single Legendre functions. This is exactly what is done in the decomposition of direct product

bases for irreducible representations of the rotation group:

$$\mathcal{P}_{J_1}^{|m|}(x)\mathcal{P}_{J_2}^{|m|}(x) = \sum_{L=|J_1-J_2|}^{J_1+J_2} \sqrt{2\pi} C(J_1, J_2, L|m, -m, 0) \mathcal{P}_L^0(x), \quad (3.6)$$

where $C(J_1, J_2, L|m, -m, 0)$ are Clebsch-Gordan coefficients [41]. Next, we introduce the variables $J = J_1 + J_2$ and $\Delta J = J_1 - J_2$, and the notational simplification:

$$C_{J,\Delta J,L}^m = \sqrt{2\pi} C\left(\frac{J+\Delta J}{2}, \frac{J-\Delta J}{2}, L|m, -m, 0\right).$$

Writing the position distributions Eq. (3.5) in the new variables J and ΔJ , and using Eq. (3.6) we arrive at:

$$\Pr(x, t) = \left(\sum_{\substack{J=|m| \\ J \text{ even}}}^{\infty} \sum_{\substack{J \\ \Delta J \text{ even}}}^J + \sum_{\substack{J=|m| \\ J \text{ odd}}}^{\infty} \sum_{\substack{J \\ \Delta J \text{ odd}}}^J \right) \rho_m\left(\frac{J+\Delta J}{2}, \frac{J-\Delta J}{2}\right) \times e^{-i\Omega\Delta J(J+1)t} \sum_{L=|\Delta J|}^J \mathcal{P}_L^0(x) C_{J,\Delta J,L}^m. \quad (3.7)$$

For readability, we shall in the following abbreviate the summations in the first line of Eq. (3.7) as:

$$\sum_{J,\Delta J}^{ee,oo}. \quad (3.8)$$

We have now expanded the time dependent position distribution on orthogonal polynomials $\mathcal{P}_\alpha^0(x)$ with coefficients that can be found by simple spatial integrals $\int_{-1}^1 dx \mathcal{P}_\alpha^0(x) \Pr(x, t)$. These coefficients, in turn, are linear combinations of the density matrix elements which can be found if the distribution is recorded at different times, as we show below.

3.4.3 Reconstruction formulas

In this subsection we will present the reconstruction formulas. We will first consider the off-diagonal elements of the density matrix and deal with the diagonal elements further below.

Reconstruction of off-diagonal elements

We let $N_T T$ be the time interval in which position measurements $\text{Pr}(x, t)$ have been performed. Here $N_T \in \mathbb{N}$ and the minimum measurement time $T = 2\pi\mathcal{I}/\hbar$, equalling $\sqrt{2}$ times the semiclassical rotational period of the $J_1 = 1$ state or the rotational revival period [37].

The time dependent factor $e^{-i\Omega\Delta J(J+1)t}$ in Eq. (3.7) suggests that a temporal Fourier transform evaluated at frequency $\Omega\beta(\alpha + 1)$, with α and β suitably chosen integers, will be part of the reconstruction procedure. Following this strategy, we consider the integral:

$$\begin{aligned}
 I(\alpha, \beta) &= \frac{1}{N_T T} \int_0^{N_T T} dt e^{i\Omega\beta(\alpha+1)t} \int_{-1}^1 dx \mathcal{P}_\alpha^0(x) \text{Pr}(x, t) \\
 &= \sum_{J, \Delta J}^{ee, oo} \rho_m \left(\frac{J + \Delta J}{2}, \frac{J - \Delta J}{2} \right) \delta_{\beta(\alpha+1), \Delta J(J+1)} \times \\
 &\qquad \sum_{L=|\Delta J|}^J C_{J, \Delta J, L}^m \delta_{L, \alpha}, \tag{3.9}
 \end{aligned}$$

where $\alpha \in \{|m|, |m+1|, \dots\}$ and $\beta \in \{-\alpha, -\alpha+2, \dots, \alpha\}$, which makes both α and β either even or odd. For the time being, we shall choose $\beta \neq 0$ and deal with the $\beta = 0$ case (i.e. diagonal matrix elements) later.

Notice that the delta-function in the sum over L ensures that α , J and ΔJ are all of the same parity. This is also the parity of β , since we chose α and β to be of the same parity.

$$\begin{aligned}
 I(\alpha, \beta) &= \sum_{\substack{J=|m| \\ \text{parity as } \alpha}}^{\infty} \sum_{\substack{\Delta J=-J \\ \text{parity as } \alpha}}^J \rho_m \left(\frac{J + \Delta J}{2}, \frac{J - \Delta J}{2} \right) \times \\
 &\qquad \delta_{\beta(\alpha+1), \Delta J(J+1)} C_{J, \Delta J, \alpha}^m \sum_{L=|\Delta J|}^J \delta_{L, \alpha}. \tag{3.10}
 \end{aligned}$$

Rather than giving a single term in the general case, the sums are greatly simplified. From the L -sum we get $I(\alpha, \beta) = 0$ unless:

$$|\Delta J| \leq \alpha \leq J. \tag{3.11}$$

Using this in conjunction with the other delta-function we find $I(\alpha, \beta) = 0$ unless:

$$|\Delta J| \leq |\beta| \leq \alpha, \quad \beta \text{ and } \Delta J \text{ of same sign.} \tag{3.12}$$

Furthermore, this delta-function demands:

$$\beta(\alpha + 1) = \Delta J(J + 1). \quad (3.13)$$

As it turns out, for many choices of α and β there is only the straightforward solution to the equation Eq. (3.13) under the conditions Eqs. (3.11) and (3.12), namely $\alpha = J$ and $\beta = \Delta J$. In these cases we easily find the density matrix elements:

$$I(\alpha, \beta) = C_{\beta, \alpha, \alpha}^m \rho_m \left(\frac{\alpha + \beta}{2}, \frac{\alpha - \beta}{2} \right), \quad \begin{array}{l} \text{for unique integer solution} \\ \text{to 3.11, 3.12 and 3.13.} \end{array} \quad (3.14)$$

For some choices of α and β there will be more than one term surviving from the sums in Eq. (3.10). The physical reason for this is that there is more than one pair of energy eigenstates having a certain energy difference. One example is the energy difference between the states ($J_1 = 3 \rightarrow J_2 = 0$) and between the states ($J_1 = 6 \rightarrow J_2 = 5$). In our variables this corresponds to ($J = 3, \Delta J = 3$) and ($J = 11, \Delta J = 1$). These degeneracies are easily found numerically by using Eq. (3.13) and the conditions Eqs. (3.11) and (3.12). We proceed to show that all density matrix elements with $\beta \neq 0$ can be found regardless of this complication.

Imagine that we have found $I(\alpha, \beta)$ to contain the term $C_{\beta, \alpha, \alpha}^m \rho_m \left(\frac{\alpha + \beta}{2}, \frac{\alpha - \beta}{2} \right)$, but also several other terms $C_{\beta'_{n_1}, \alpha'_{n_1}, \alpha}^m \rho_m \left(\frac{\alpha'_{n_1} + \beta'_{n_1}}{2}, \frac{\alpha'_{n_1} - \beta'_{n_1}}{2} \right)$, where $n_1 = 1, 2, \dots, N_1$. The strategy is to calculate all the integrals $I(\alpha'_{n_1}, \beta'_{n_1})$. These may also contain several terms with ($J = \alpha''_{n_2}, \Delta J = \beta''_{n_2}$), where $n_2 = 1, 2, \dots, N_2$, but always fewer than in the former integrals, i.e. $N_j < N_{j+1}$. The reason for this is the condition $|\Delta J| \leq |\beta|$ from Eq. (3.12): Whereas the $\beta = \Delta J$ term will always appear, the rest of the terms in the sum Eq. (3.10) will have $\Delta J < \beta$, whereby the procedure will terminate and we can find all the matrix elements of $\hat{\rho}_m$ by back substitution.

To clarify this procedure a little, let us consider an example: We shall try to find the matrix element $\rho_m(5, 0)$. In this case $J = \Delta J = 5$, and we find $I(5, 5) = C_{5, 5, 5}^m \rho_m(5, 0) + C_{9, 3, 5}^m \rho_m(6, 3) + C_{29, 1, 5}^m \rho_m(15, 14)$. To find the desired matrix element we shall need the two extra equations $I(9, 3) = C_{9, 3, 3}^m \rho_m(6, 3) + C_{29, 1, 3}^m \rho_m(15, 14)$ and $I(29, 1) = C_{29, 1, 1}^m \rho_m(15, 14)$. These three resulting equations can be solved by back substitution to yield $\rho_m(5, 0)$, $\rho_m(6, 3)$ and $\rho_m(15, 14)$.

Reconstructing the diagonal

We proceed to show how one can go about finding the diagonal of $\hat{\rho}_m$ in the energy-representation. To do this we shall use Eq. (3.10) with $\beta = 0$, by which α is even:

$$\begin{aligned}
 I(\alpha, 0) &= \frac{1}{N_T T} \int_0^{N_T T} dt \int_{-1}^1 dx \mathcal{P}_\alpha^0(x) \text{Pr}(x, t) \\
 &= \sum_{\substack{J=|m| \\ J \text{ even}}}^{\infty} \rho_m \left(\frac{J}{2}, \frac{J}{2} \right) C_{J,0,\alpha}^m \\
 &= \sum_{J_1=\text{ceil}(\frac{|m|}{2})}^{\infty} \rho_m(J_1, J_1) C_{2J_1,0,\alpha}^m,
 \end{aligned} \tag{3.15}$$

where we have used $J_1 = J/2$ and the ceil-function rounds upwards to nearest integer. We notice that the coefficient $C_{2J_1,0,\alpha}^m$ is zero unless $\alpha \leq 2J_1$. We arrange the $I(\alpha, 0)$ in a column vector \mathbf{I} and the $\rho_m(J_1, J_1)$ in a column vector \mathbf{R} :

$$\begin{aligned}
 \mathbf{I} &= \begin{pmatrix} I[2|m|, 0] \\ I[2(|m|+1), 0] \\ \vdots \end{pmatrix}, \\
 \mathbf{R} &= \begin{pmatrix} \rho_m(|m|, |m|) \\ \rho_m(|m|+1, |m|+1) \\ \vdots \end{pmatrix}.
 \end{aligned}$$

Eq. (3.15) now reads:

$$\begin{aligned}
 \mathbf{I} &= \mathcal{M}_m \cdot \mathbf{R}, \quad \text{where} \\
 \mathcal{M}_m &= \underbrace{\begin{pmatrix} C_{2|m|,0,2|m|}^m & C_{2(|m|+1),0,2|m|}^m & \cdots \\ 0 & C_{2(|m|+1),0,2(|m|+1)}^m & \cdots \\ \vdots & \vdots & \ddots \end{pmatrix}}_{\text{upper-triangular}}
 \end{aligned} \tag{3.16}$$

To find the desired elements $\rho_m(J_1, J_1)$ we shall need to invert the matrix \mathcal{M}_m , which can be done since the diagonal elements $C_{\alpha,0,\alpha}^m = \sqrt{2\pi} C(\alpha/2, \alpha/2, \alpha|m, -m, 0)$ are all non-zero.

It may be noted that since the linear system (3.16) always has the same coefficient matrix, we could just as well have used a function $\mathcal{F}_{J_1}^{(m)}(x)$ that selects a certain J_1 in Eq. (3.15), so that:

$$\rho_m(J_1, J_1) = \frac{1}{N_T T} \int_0^{N_T T} dt \int_{-1}^1 dx \mathcal{F}_{J_1}^{(m)}(x) \Pr(x, t).$$

The functions $\mathcal{F}_{J_1}^{(m)}(x)$ can be precalculated and are given by:

$$\mathcal{F}_{J_1}^{(m)}(x) = \sum_{J'=J_1}^{\infty} f_{J_1, J'}^{(m)} \mathcal{P}_{2J'}(x),$$

where the expansion coefficients $f_{J_1, J'}^{(m)}$ can be found by using Cramer's rule and the fact that \mathcal{M}_m is upper-triangular:

$$f_{J_1, J}^{(m)} = (-1)^{J_1+J'} \frac{|\mathcal{M}_{J_1, J'}^{\text{sub}}|}{\prod_{\gamma=J_1-|m|+1}^{J'-|m|+1} \mathcal{M}_m(\gamma, \gamma)}, \quad (3.17)$$

and $|\mathcal{M}_{J_1, J'}^{\text{sub}}|$ is the determinant of the sub-matrix:

$$\mathcal{M}_{J_1, J'}^{\text{sub}} = \begin{cases} 1 & \text{if } J = J_1 \\ \mathcal{M}_m(J_1 - |m| + 1 : J' - |m|, J_1 - |m| + 2 : J' - |m| + 1) & \text{otherwise.} \end{cases}$$

This method would be relevant if only a few particular diagonal elements of the density matrix are desired. One may notice the similarity of these functions to the pattern functions used with harmonic oscillator systems [18], [19].

It may be noted that we could not have circumvented the back substitution procedure for the elements with $\beta \neq 0$ above by choosing other functions than the $\mathcal{P}_\alpha^0(x)$ in Eq. (3.10). The reason is that the solution of the resulting system of equations depends on the measurement values through the $I(\alpha_j, \beta_j)$'s.

For most practical application one will be interested in only part of the density matrix, truncated at some maximum $J_1, J_2 = J_{max}$ corresponding to truncating at high energies. In this case the Fourier time-integrals are replaced with discrete Fourier sums, requiring measurements at frequency $2\Omega J_{max}(J_{max} + 1)$. If measurements are made with a lower frequency, errors will be introduced through aliasing except for the elements evolving with the unique lowest non-zero frequency $\rho(0, 1)$ and $\rho(1, 0)$.

3.5 Real molecules and centrifugal distortion

In the above treatment we used the rigid rotor Hamiltonian $\hat{H} = \frac{\hat{J}^2}{2I}$, whereas terms of higher order in \hat{J}^2 will be important in real molecules in highly excited rotational states. Such states may be reached in the experimental situation described in section 3.2. With the lowest order centrifugal distortion the Hamiltonian is instead:

$$\hat{H}' = \frac{\hat{J}^2}{2I} - \frac{D\hat{J}^4}{\hbar^3}.$$

The states $|J, m\rangle$ are still the energy eigenstates, but here with energy $E_J = \hbar\Omega J(J+1) - \hbar D J^2(J+1)^2$. The constant $D \propto \frac{1}{T^3\omega^2}$, where ω is the harmonic frequency of the molecular bond. The reconstruction strategy is similar to the one in Eq. (3.9):

$$I_{CD}(\alpha, \beta) = \lim_{T \rightarrow \infty} \frac{1}{T} \int_0^T dt e^{i\beta(\alpha+1)[\Omega - D\beta(\alpha+1)]t} \int_{-1}^1 dx \mathcal{P}_\alpha^0(x) \text{Pr}(x, t). \quad (3.18)$$

In this case, the conditions Eqs. (3.11) and (3.12) still apply, but Eq. (3.13) is replaced by:

$$\beta(\alpha+1) - \frac{D}{\Omega} \beta^2(\alpha+1)^2 = \Delta J(J+1) - \frac{D}{\Omega} \Delta J^2(J+1)^2. \quad (3.19)$$

Depending on the value of D/Ω , there may be more than one set of $(\Delta J, J)$ that satisfies the conditions Eqs. (3.11)-(3.12) and Eq. (3.19), but it will usually be much fewer than in the rigid rotor case. Consequently, one can often avoid the back substitution procedure above and use $I_{CD}(\alpha, \beta) = C_{\beta, \alpha}^m \rho_m\left(\frac{\alpha+\beta}{2}, \frac{\alpha-\beta}{2}\right)$.

3.6 Symmetric top states

Having treated the linear rotor, we will straightforwardly generalize the results from section 3.4 to symmetric top molecules. This class contains many more molecules than the linear class.

The eigenvectors of the Hamiltonian are in this case the set $\{|Jkm\rangle\}$ with associated energy $E = \hbar\Omega_1 J(J+1) - \hbar\Omega_2 k^2$. Here k is the quantum number for the projection of the angular momentum on the symmetry axis of the molecule, whereas we recall that m is associated with the projection on a space-fixed axis. Like m , k can assume the values $-J, -J+1, \dots, J$. For a linear molecule $k=0$, and the treatment in section 3.4 can indeed be seen as a special case of the

symmetric top. In accordance with the above treatment we shall assume that we can measure the polar angular distribution, parametrized by $x = \cos(\theta)$, for a certain value of k and m . The angular position representations of the eigenstates are:

$${}_t\langle x|Jkm\rangle = \sqrt{\frac{2J+1}{2}} d_{km}^J(x) e^{-i[\Omega_1 J(J+1) - \Omega_2 k^2]t},$$

where the $d_{km}^J(x)$ are the usual rotation matrix elements, and the eigenstates are normalized on $[-1, 1]$. The quantities $\Omega_1 = \hbar/2\mathcal{I}_x$ and $\Omega_2 = \hbar/(2\mathcal{I}_z - 2\mathcal{I}_x)$. Here we have chosen the z axis as the molecular symmetry axis, and used that the moments of inertia $\mathcal{I}_x = \mathcal{I}_y$. As in Eq. (3.3), we can safely ignore the dependence of the two other Euler angles ϕ and χ , since we are working in the subspace of fixed k and m . We can now readily generalize the treatment in section 3.4 by exchanging the functions $\mathcal{P}_J^{|m|}(x)$ with $\sqrt{(2J+1)/2} d_{km}^J(x)$ and the lower summation indices $|m|$ with $M_{km} = \max(|m|, |k|)$. In particular, Eq. (3.5) generalizes to:

$$\begin{aligned} \text{Pr}(x, t) &= {}_t\langle x|\hat{\rho}_{k,m}|x\rangle_t \\ &= \sum_{\substack{J_1= \\ M_{km}}}^{\infty} \sum_{\substack{J_2= \\ M_{km}}}^{\infty} \rho_m(J_1, J_2) d_{km}^{J_1}(x) d_{km}^{J_2}(x) \\ &\quad \times \sqrt{\frac{(2J_1+1)(2J_2+1)}{4}} e^{-i\Omega_1[J_1(J_1+1) - J_2(J_2+1)]t}. \end{aligned} \quad (3.20)$$

Products of the functions $d_{km}^J(x)$ can again be decomposed into linear combinations of single Legendre functions, again introducing $J = (J_1 + J_2)/2$ and $\Delta J = (J_1 - J_2)/2$ [17], [42]:

$$\sqrt{\frac{(2J_1+1)(2J_2+1)}{4}} d_{km}^{J_1}(x) d_{km}^{J_2}(x) = \sum_{L=|J_1-J_2|}^{J_1+J_2} C_{J,\Delta J,L}^{km} \mathcal{P}_L^0(x), \quad (3.21)$$

where

$$C_{J,\Delta J,L}^{km} = \sqrt{\frac{2}{2L+1}} C(J_1, J_2, L|m, -m, 0) C(J_1, J_2, L;k, -k, 0). \quad (3.22)$$

Proceeding as in section 3.4, we calculate the integrals $I(\alpha, \beta)$ and arrive at the

equivalent of Eq. (3.10):

$$\begin{aligned}
 I(\alpha, \beta) &= \sum_{\substack{J=M_{km} \\ \text{parity as } \alpha}}^{\infty} \sum_{\substack{J \\ \Delta J=-J \\ \text{parity as } \alpha}} \rho_{k,m} \left(\frac{J+\Delta J}{2}, \frac{J-\Delta J}{2} \right) \times \\
 &\quad \delta_{\beta(\alpha+1), \Delta J(J+1)} C_{J, \Delta J, \alpha}^{km} \sum_{L=|\Delta J|}^J \delta_{L, \alpha}. \tag{3.23}
 \end{aligned}$$

The reconstruction of the matrix elements $\rho_{k,m}(J_1, J_2)$ can therefore be done like in section 3.4.3, where one uses the $C_{J, \Delta J, L}^{km}$ defined in Eq. (3.22) instead of $C_{J, \Delta J, L}^m$.

3.7 Discussion

The method above effectively deals with a semi-continuous one-dimensional reconstruction in the space of x and J , and not with the reconstruction of a general state. The reason for this limitation is that the inversion formulas we are using are integral transformations that preserve dimensionality, like e.g. the Fourier transformation in t in Eq. (3.9). If the dimensionality of the measurements are not at least as large as the dimensionality of the quantum state, such an approach nearly always fails as we showed in chapter 2. As discussed there, in one dimension the density matrix is a two-dimensional object $\langle x | \hat{\rho}_{k,m} | x' \rangle$ which has the same dimensionality as the measurement-space $\text{Pr}(x, t)$. In contrast, the full quantum state of e.g. the linear rotor is a four-dimensional object $\langle x, \phi | \hat{\rho} | x', \phi' \rangle$, while the angular measurements $\text{Pr}(x, \phi, t)$ would be only three-dimensional. If one desired to reconstruct a full general quantum state, one would either have to be able to perform more advanced measurements or to vary the Hamiltonian – an idea suggested for reconstruction of translational states in [43]. Because of the difficulty of precisely knowing Hamiltonians arising from e.g. additional laser pulses, we have instead treated the one-dimensional system using only previously demonstrated measurements.

In spite of this limitation, the situation where the one-dimensional description is a complete characterization of the quantum system is experimentally common. Indeed, for the situation described in the introduction, there are no correlations between the different k and m quantum numbers. The question is of course whether one can perform measurements of polar angular distributions for certain k and m quantum numbers.

A conceptually straightforward solution would be to use very low-temperature samples, where only $k = m = 0$ is populated before the interaction with the pump pulse. Note that this would not imply that the created rotational state would be a pure state, due to inhomogeneities in the pump pulse focus. Such inhomogeneities could for example be caused by variation of the intensity over the pump pulse focus or shot-to-shot variation of laser intensity. Though conceptually simple, this situation is unpractical due to the smallness of the rotational energies demanding very low temperatures.

A more practical approach would be to select a certain value of k and m before interaction with the pump pulse. For polar symmetric top molecules this can be done for certain values of k and m by using the linear Stark effect through hexapole focusing techniques [44], [45]. The linear Stark shift for symmetric tops is $\Delta E^{(1)} = -\mu \varepsilon k m / J(J+1)$, where μ is the dipole moment and ε is the magnitude of the electric field. Since one starts out with a thermal sample, there are no correlations in either J , k or m in the state before interactions with the pump. Therefore, one does not discard any information about the state by picking out all sets of values of J , k and m one by one. If the molecular beam were sufficiently cold, one could select components of the beam with certain k and m values, as is required by the method above. One would then also select a certain value of J , which is not required, but on the other hand poses no problem. Furthermore, the apparent ambiguity that a change of sign of both k and m gives the same Stark shift is of no consequence, since the state created by the pump has identical matrix elements $\rho_{k,m}(J, J')$ and $\rho_{-k,-m}(J, J')$ due to the invariance of the initial state and of the pump-pulse interaction Hamiltonians under the interchange $(k, m) \rightarrow (-k, -m)$.

Most linear molecules and symmetric tops with $k = 0$ do not exhibit any linear Stark shift [46], but also here hexapole focusing techniques can be used to select specific values of J and m through the second order Stark shift. In this case, both molecules with the quantum numbers (J, m) and $(J, -m)$ are selected, but this is of no consequence since $\rho_m(J, J') = \rho_{-m}(J, J')$ in accord with the previous paragraph.

Having all cards on the table, we need consider the experimental feasibility of the above reconstruction method. It is clear that we need many accurate measurements, both in space and in time. Our method needs the cylindrically symmetrical 3D distributions which can be found from the measured 2D distributions, see section 3.2. This can be done using Abel inversion or the raw 2D data can be used, but either way requires good statistics. This is due to the rapid spatial variations we need to resolve to perform the spatial integrals in finding $I(\alpha, \beta)$, see e.g. Eq. (3.9). A more severe requirement is the neces-

sary number of time samples, which in the rigid rotor case may be of the order of 100 to 1000 for complete reconstruction in many experiments with strong pump pulses. Obtaining such data is challenging and very time-consuming with present-day techniques, but may become accessible in the future. If one uses weaker pump pulses, so as to excite only relatively low angular momentum states, one can make do with measuring at much fewer time points, making a full reconstruction more realistic.

In conclusion, we have presented a method to reconstruct the blocks $\rho_{k,m}(J, J')$ of the rotational density matrix for linear and symmetric top molecules from angular distributions at different points of time. Hereby we have also proved that the required information is present in such measurements, which may substantiate the use of approximate reconstruction methods. The reconstructed blocks amount to a complete characterization of the quantum state in a widespread experimental setup. We have suggested how the required measurements in principle could be performed with existing techniques. Finally, we have commented on which elements of the density matrix can be found in a more realistic experimental situation.

Chapter 4

Reconstruction of vibrational states excited from warm molecules probed by four-wave mixing

4.1 Synopsis

We propose a method to reconstruct the bound vibrational quantum state of gas phase molecules excited by a general excitation laser pulse. Unlike existing methods which work for pure states only, we treat also the important case of molecules being in a thermal state prior to the excitation. In addition to the excitation pulse, the method uses two incident, short laser pulses in a non-collinear geometry to create four-wave mixing in the molecules. The measurements used in the reconstruction are spectra of the outgoing four-wave mixing pulse at different time delays of the excitation laser pulse. Contrary to usual reconstruction methods, this method does not require detailed knowledge of the dynamics, but circumvents this requirement by using one or more calibration laser pulses in a separate experiment, either before or after the main data are recorded.

Finally, we discuss the extension of the reconstruction method in this chapter to more general situations, hereby presenting the new idea of Quantum State Reconstruction through perturbations with calibration.

The chapter is based on the article [47].

4.2 Introduction

Everything worth knowing about a molecule at any given time is its physical state. Hence, whether one's interest lies in interaction of radiation with the molecule, chemical reactivity or intra-molecular processes, the state contains this information. Evidently, it is of great interest to be able to determine this state. In this chapter, we propose a method to determine part of such a molecular state in a four-wave mixing experiment. The method presented could be particularly useful for determining the molecular states prepared by a single, optically tailored femtosecond laser pulse. Production of this type of laser pulses has been demonstrated [48]-[50] and they have been used to produce specific vibrational states in molecules [51], [52].

In particular, we will concentrate on finding the unknown bound vibrational state of a gas phase molecule which has been excited by a short laser pulse from an initial thermal state. Throughout the chapter, we will neglect rotational degrees of freedom. As discussed in the chapter's last section, this assumption may be serious, and we emphasize that the actual feasibility of the proposed method must be determined by experiment.

Earlier works directly related to this chapter have proposed reconstructing vibrational states for diatomic molecules using time-dependent fluorescence spectra [14], and heterodyne detection of fluorescence [53], for more general molecules using time- and frequency- resolved fluorescence [54], [55], and using time- and frequency-integrated fluorescence and a known reference state for quantum state holography [56]. Common for these proposals is the requirement that the initial state be a pure state. Realistically, fulfilling this requirement in turn demands a sufficiently low temperature of the molecules before the creation of the vibrational excitation. This initial temperature must be so low that only the lowest vibrational level is populated. For many molecules, this is unpractical. For instance, to perform such an experiment on gaseous iodine at adequately high pressure to obtain a good signal, one must have a temperature high enough to populate several vibrational states, lest the iodine is deposited [51], [57], [58]. It is important to note that even though the initial thermal state's ground vibrational state population is larger than that of all other vibrational

states, it does not guarantee that this state gives the dominating contribution to the unknown excited state. This is due to the different Franck-Condon factors involved in the formation of the unknown excited state by the excitation laser pulse. Hence, taking several initially thermally populated levels into account can be essential to understanding the excited state formed.

The chapter is arranged as follows: In section 4.3 we identify the type of quantum state being reconstructed and briefly remark on this chapter's approach to measurements, which differs from the prequel. In section 4.4 we outline an experimental implementation of the required measurements and give an overview of the energy- and time-regimes involved. In section 4.5 we show by calculation how to reconstruct the unknown vibrational quantum state. In section 4.6 we discuss the generality and feasibility of the reconstruction procedure and conclude the chapter.

4.3 States and measurements

In this section, we will more closely specify what we mean by the physical state in the context of the present chapter. Moreover, we state a point where the present approach to measurements and dynamics differ from that of chapters 1-3.

The type of state we seek in this chapter is an unknown bound vibrational state of a sample of molecules, coherently excited from an initial thermal state. Specifically, we will restrict the reconstruction of the unknown vibrational state to the electronic state it populates, denoted by the electronic index a , and thus not find correlations with the initial thermal population. This is exactly what is usually meant by the concept of an excited vibrational state. For transparency, we restrict ourselves to the most important case where the initial thermal state is limited to the electronic ground state, with possibly several vibrational levels populated. The excitation that forms the unknown vibrational state needs not be perturbative in the sense that it may transfer a large fraction of the initial thermally populated level to the electronic state a . Nevertheless, it must leave a non-vanishing population in the initial state and not transfer population back to other of the initially populated levels.

Since the initial state is a mixed state, we cannot describe it by a single wave function, and because coherent excitations preserve the mixed character, neither can we describe the excited vibrational state this way. A sufficing description is the density matrix, for which the initial thermal state would be diagonal in the energy basis, but we shall take a more transparent course: Using incoherent vec-

tor states, as explained below. This course is completely equivalent to a density matrix description, and we introduce it merely as a mathematical trick. Using this trick, we quite naturally separate the problem into pure state sub-problems with no loss of generality, but hopefully with increased clarity. In particular, it will reduce the number of terms when we use third order perturbation theory below. Without further delay, let us have a look at this trick.

As the states originating in different energy levels in the initial thermal state are quantum mechanically incoherent with respect to each other, and the vibrational state we seek is coherently excited from these, we can describe the system as an incoherent sum of vector states (corresponding to wave functions). By an incoherent sum, we mean forming a sum of the states, each with a phase factor $\exp(i\theta_k)$ labeled after the original energy level k in the initial thermal state from which the coherent excitation took place¹. These phase factors will be averaged over when taking inner products, making incoherent cross-terms vanish. In this chapter, each incoherent term will be labeled by a left subscript, such as ${}_k\beta$. To illustrate this, consider the example of a thermal state of a molecule with the only energy levels populated being the vibrational levels $k = 0$ and $k = 1$ in the electronic ground state. We then imagine applying a laser pulse to the molecule, exciting a vibrational state in another electronic level a , the vibrational eigenstates $|\phi_{a,l}\rangle$ herein being labeled by index l . The excited state will then be:

$$\begin{aligned} |\psi_a\rangle &= \sum_k |{}_k\psi_a\rangle \\ &= |{}_{k=0}\psi_a\rangle + |{}_{k=1}\psi_a\rangle \\ &= e^{i\theta_0} \sum_l {}_0\beta_l |\phi_{a,l}\rangle + e^{i\theta_1} \sum_l {}_1\beta_l |\phi_{a,l}\rangle, \end{aligned}$$

where the ${}_k\beta_l$ are expansion coefficients. What we mean by "finding the unknown excited vibrational state" is: determining all the complex expansion coefficients ${}_k\beta_l$ up to a common phase for each k . With the incoherent averaging, inner products between states originating from different levels in the initial thermal state vanish, e.g.

$$\langle {}_{k=0}\psi_a | \hat{A} | {}_{k=1}\psi_a \rangle \propto \int_0^{2\pi} d\theta_0 e^{-i\theta_0} \int_0^{2\pi} d\theta_1 e^{i\theta_1} = 0,$$

where \hat{A} can be any operator. Thus, we will not see any cross-terms between states originating in different energy levels of the initial thermal state, whence

¹In this way, we are effectively picking out each pure state component of the mixed state, labeling them by k and assuring that there are no coherences between them.

we will conveniently treat these states for different k separately. However, one should notice that it is still possible to see interference in an intensity signal between the light formed from different incoherent levels. This can be easily seen by considering the two electric fields formed by dipole transitions from level a to the electronic ground state 0:

$$\begin{aligned} {}_{k=0}E(t) &\propto d^2/dt^2 \langle {}_{k=0}\psi_0 | \hat{d} | {}_{k=0}\psi_a \rangle, \\ {}_{k=1}E(t) &\propto d^2/dt^2 \langle {}_{k=1}\psi_0 | \hat{d} | {}_{k=1}\psi_a \rangle, \end{aligned}$$

where \hat{d} is the scalar product of the dipole moment operator with the electric field's polarization vector. Although the incoherent θ_k -factors cancel in each electric field, we will still observe interference in the measurable intensity signal $I \propto [{}_{k=0}E(t) + {}_{k=1}E(t)]^2$.

Having defined the state, we turn to the measurements we will use to reconstruct it. In chapter 1, we introduced the approach of performing the same measurements at several points of time, thereby letting the dynamics reveal the quantum state. Using this approach, one is almost always forced to assume full knowledge of the dynamical laws of the physical system. Even so, we shall largely circumvent such assumptions by instead performing a calibration of the measurement apparatus. The measurements we will use are spectrograms: Spectra of four-wave mixing laser pulses, created at different times after the formation of the excited vibrational state. We will show that such a spectrogram encompasses a quorum for determining the set $\{{}_k\beta_l\}$ up to a common phase factor for each k .

4.4 Experimental implementation outline

In this section we outline a pump-probe experiment where one could record the data necessary for the vibrational state reconstruction. This is a four-wave mixing experiment, where one sends in three laser pulses 1-3 from different directions on a gaseous molecular sample, and records the spectrum of the outgoing four-wave mixing (FW) pulse [57]. For simplicity, we shall let all pulses have the same linear polarization. Laser pulse 1 reaches the molecular sample first and can be regarded as a pump pulse, since it has the effect of creating the unknown vibrational quantum state in the molecules. Pulses 2 and 3 arrive at the molecules long after pulse 1 is over, and can be regarded as a probing process. The time τ when pulse 1 creates the unknown state is varied from one experimental run to the next, retaining the timing of pulses 2 and 3. One then measures the spectrum of the resulting *FW* pulse. The time sequence of the

four laser pulses is outlined in Fig. 4.1. One should notice that even though the pulses 1-3 should individually be the same from one run to the next, there is no requirement of relative phase stabilization.

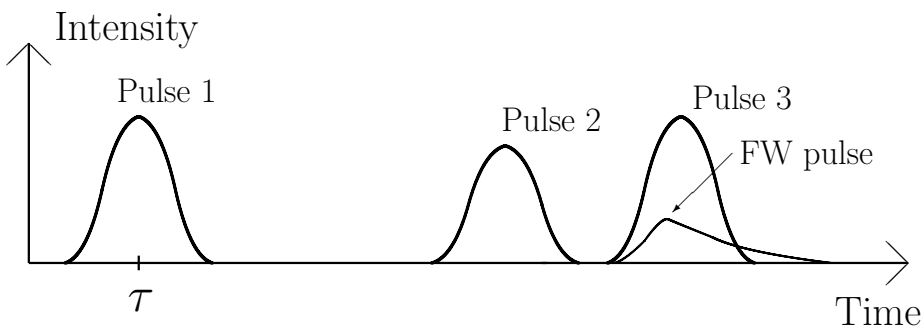


Figure 4.1: Schematic time sequence of the laser pulses. First, pulse 1 excites a bound vibrational state in a gaseous sample of initially thermal molecules at time τ . When pulse 1 is over, the molecules are probed using the pulses 2 and 3. While the pulses 1-3 are always the same, the time τ is varied from one experimental run to the next. The interaction of the three pulses 1-3 with the molecules gives rise to a four-wave mixing (FW) pulse. The spectrum of this *FW* pulse is measured together with the current value of τ . Of further note is that the emission of the coherent *FW* pulse can continue long after the incident pulses 1-3 have died out, since the emission is due to an excitation in the molecules. Because it will prove to make the reconstruction much easier, we will require that pulse 2 and 3 have no temporal overlap, as shown.

To keep the theoretical treatment transparent, we will now introduce several simplifying assumptions. With the exception of a single key requirement specified below, these assumptions are only included for clarity. Indeed, we will do away with the non-essential ones in section 4.6.

The laser pulses involved will all cause transitions in the molecules, dominated by dipole transitions. In Fig. 4.2 we shown an overview of such a series of transitions, each being accompanied by a change of the electronic state. We have sketched the four electronic states 0 and *a-c*, and within each of these several vibrational states. In the figure, we have shown the usual situation where the electronic states are energetically separated by a much larger energy than the vibrational states within them. Furthermore, the figure shows that the transitions due to pulse 2 always occur before transitions due to pulse 3. Realistically,

this could be the case if pulse 2 precedes pulse 3 so that they have no temporal overlap, as shown in Fig. 4.1. This is the key requirement mentioned above and we shall see its usefulness in section 4.5.1. These assumptions give the most transparent situation, and we shall calculate the spectrum of the FW pulse in section 4.5 using them. Finally, we must require that only a single photon from each of the pulses 2 and 3 are involved in each transition; a requirement implicit in Fig. 4.2.

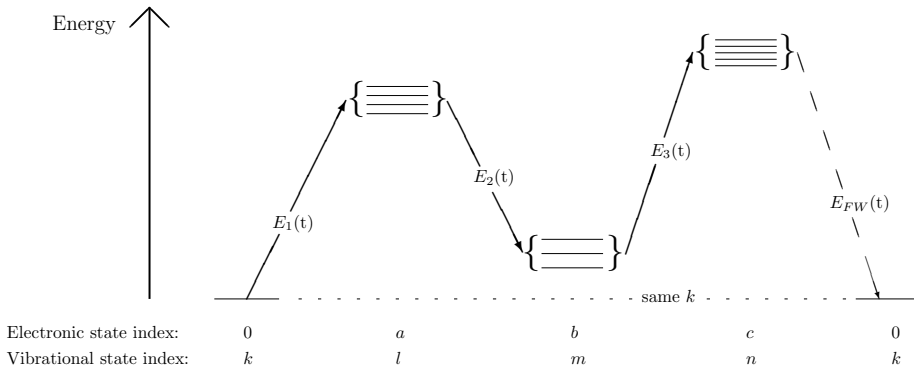


Figure 4.2: Schematic energy diagram showing the levels of the molecular system and the four laser pulses with time-dependent electric fields $E_j(t)$, $j = 1, 2, 3, FW$. Assuming the molecules are initially in a thermal state, we can consider each initially populated level k in turn, and perform an incoherent sum in the end. The system starts out in the electronic state 0, wherefrom laser pulse 1 creates a bound vibrational state in the electronic state a . After a time τ , which is varied from one experiment to the next, the state created with pulse 1 is probed through a four-wave mixing process using pulses 2 and 3 to transfer the system through electronic states b and c . Under coherent emission of an FW photon, the system finally ends up in the k where it originated. Some of these electronic states may be identical, e.g. $0 = b$ and $a = c$ in the experiment described in [58]. The delay time τ is chosen small enough for pulse 1 to be over when pulse 2 and 3 are applied.

One can experimentally justify the requirement that only a single photon from each of the incoming laser pulses is involved in each of the transitions, which together lead to coherent FW emission. Using the non-co-linear, so-called folded BOX-configuration shown in Fig. 4.3, one sends in pulses 1-3 from

three different directions. Each angle between the pulse propagation directions is small, typically a few degrees. One can select out the *FW* signal caused by precisely one-photon interactions from each pulse, simply by using pinholes to select out the appropriate phase-matched direction for the *FW* pulse.

The physical reason for the directionality of the *FW* pulse is that the molecular state is initially uncorrelated in the translational degrees of freedom. We will briefly pause to shed light on this point. This phase-matching argument is usually performed in the position basis, taking the emitting molecules to be distributed randomly over the focal volume. Instead, we shall use the momentum basis because it makes the argument more transparent, and is completely equivalent.

The total Hamiltonian for the molecule is the sum of two terms $\hat{H}_{total} = \hat{H} + \hat{H}_{CM}$. The internal part \hat{H} deals with the motion of nuclei and electrons with respect to the center of mass, and is the part we shall be mainly interested in. The other part, the center of mass motion, is governed by $\hat{H}_{CM} = \hat{\mathbf{P}}^2/2M$, where M is the molecular mass and $\hat{\mathbf{P}}$ is the center of mass momentum. The initial state of the molecule is uncorrelated in energy, and can be written as an incoherent sum of the states $|_k\Psi_{tot,0}\rangle = |_k\psi_0\rangle \otimes |_k\mathbf{P}\rangle_{CM}$. Here, $|_k\psi_0\rangle$ denotes the internal energy eigenstate and $|_k\mathbf{P}\rangle_{CM}$ denotes the momentum state of the center of mass, both labeled by the common energy index k . During the experiment, the molecule absorbs and emits radiation, changing the internal state. At the same time, momentum conservation dictates that the center of mass momentum changes. After absorption of one photon of momentum \mathbf{p}_1 from pulse 1, stimulated emission of one photon of momentum \mathbf{p}_2 along pulse 2, and finally absorption of one photon from pulse 3, the above state will have achieved a component $|_k\Psi'_{tot}\rangle = |_k\psi'\rangle \otimes |_k\mathbf{P} + \mathbf{p}_1 - \mathbf{p}_2 + \mathbf{p}_3\rangle_{CM}$. To have coherent emission of an *FW* pulse from this term, we must look at the inner product $\langle_k\Psi'_{tot}|\hat{d}|_k\Psi_{tot,0}\rangle$. This is zero unless the emitted photon has momentum $\mathbf{p}_{FW} = \mathbf{p}_1 - \mathbf{p}_2 + \mathbf{p}_3$, due to momentum conservation and the orthogonality of the states ${}_{CM}\langle_k\mathbf{P} + \mathbf{p}_1 - \mathbf{p}_2 + \mathbf{p}_3 - \mathbf{p}_{FW}|_k\mathbf{P}\rangle_{CM}$. Thereby, the momentum conservation becomes one of the four involved photons alone, and the apparent inability of the molecule to carry off momentum in the coherent *FW* mixing process can be understood as a thermal effect. In effect, we can use the direction of the outgoing *FW* pulse to select how many photons were emitted or absorbed from each of the incoming pulses 1-3. Having dealt with the mechanism that gives rise to the directionality of the *FW* pulse, we will in the following ignore the center of mass motion, and focus completely on the molecule's internal state.

Another important point, which will play a key role in the calculations below,

is that the directional selection will typically only select the number of photons involved in each transition, and thereby the electronic states, but not select which vibrational levels are involved in each transition. The reason is that the electronic states are separated by a comparatively large energy, giving rise to a realistically observable difference in angle for the *FW* pulse. In contrast, the vibrational levels within a certain electronic level are energetically so close that the transitions to these levels all give rise to *FW* photons traveling in practically indistinguishable directions; more accurately, the focusing angles of the incoming pulses are much greater than the change in angle needed to meet phase matching to one vibrational state or the other. The ensuing interference in the *FW* intensity is precisely the phase-sensitive quantities that we shall use in the reconstruction.

A final important reason to use the non-co-linear geometry is that it allows one to observe the *FW* pulse without the presence of the very powerful background from pulses 1-3.

4.5 Theory

In this section, we shall theoretically treat the situation outlined in the previous section, aiming at reconstructing the quantum state formed by pulse 1. We will accomplish this reconstruction through calculating the spectrum of the *FW* pulse, and expressing this spectrum through quantities determining the quantum state we seek to reconstruct. By inverting these relationships, we can finally find the sought quantum state from the measured intensity signal.

We recall from section 4.3 that we initially have a thermal state, where each energy level k may be treated independently on the quantum level. Concentrating on a fixed k , the total state formed by the three laser pulses can be written as:

$$\left| {}_k\psi(\tau) \right\rangle_t = \left| {}_k\psi_0^{(0)} \right\rangle_t + \left| {}_k\psi_a^{(1)}(\tau) \right\rangle_t + \left| {}_k\psi_b^{(2)}(\tau) \right\rangle_t + \left| {}_k\psi_c^{(3)}(\tau) \right\rangle_t, \quad (4.1)$$

where the superscript denotes which pulse has formed the state from the previous, the right subscript denotes the electronic state, and t is the time. In each of the perturbation orders, we shall for clarity retain only terms leading to coherent *FW* emission. The parameter τ signifies the time shown in Fig. 4.1; the time when the unknown excited state is formed. This state $\left| {}_k\psi_a^{(1)}(\tau) \right\rangle$ does not need to be formed perturbatively, as long as it leaves a non-vanishing population in the $\left| {}_k\psi_0^{(0)} \right\rangle$ -state, and it does not transfer population back to other of

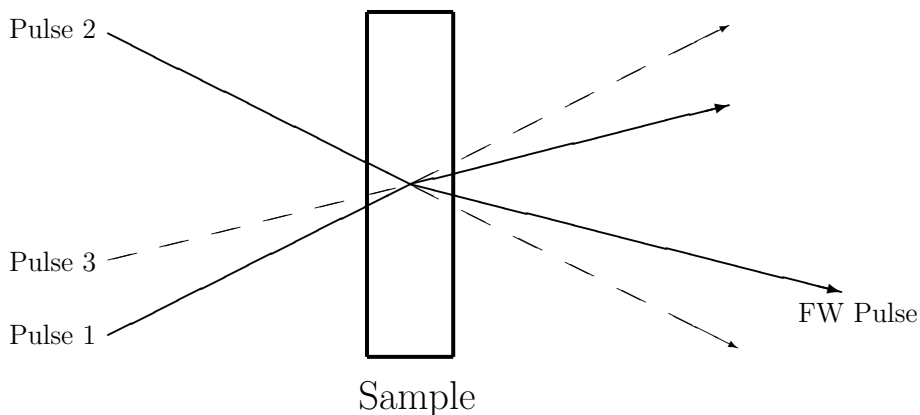


Figure 4.3: Geometric outline of the laser pulses' interactions with the molecular sample. Dashed lines signify propagation below the plane of the paper, while fully drawn lines signify propagation above. It is central to the calculations in this chapter that one uses the shown non-co-linear configuration, in which the pulses 1-3 have different propagation vectors (BOXCARS-configuration if pulses 1 and 3 are identical except for their propagation direction). As seen by the molecules, this will be similar to the pulses 1-3 approaching from three of the four corners in a rectangle. By using a pinhole, one may separate out the *FW* pulse, hereby ensuring that the measured interaction in the molecular sample has involved precisely one photon from each of the pulses 1-3. It should be noticed that, in contrast to usual four-wave mixing with narrow band pulses, the BOX configuration gives only state-selectivity of the electronic state, but not of the vibrational states herein. This practical inability to tell apart vibrational levels by the angle of the *FW* photon arises due to the energetic closeness of the vibrational levels compared to the energetic distance between the different electronic states. Thus, transition to a certain electronic state gives rise to a easily detectable angular difference, whereas the transition to different vibrational states herein does not; see also Fig. 4.2.

the thermally populated levels (i.e. other k -indices). We expand the unknown state $\left| {}_k\psi_a^{(1)}(\tau) \right\rangle$ on the bound vibrational eigenstates $|\phi_{a,l}\rangle$ with energy $\hbar\tilde{\omega}_l^a$, belonging to the electronic level a :

$$\left| {}_k\psi_a^{(1)}(\tau) \right\rangle_{t_2} = e^{i\theta_k} \sum_l {}_k\beta_l |\phi_{a,l}\rangle e^{i\tilde{\omega}_{l,k}^{a,0}\tau} e^{-i\tilde{\omega}_l^a t_2}, \quad (4.2)$$

where the ${}_k\beta_l$ are expansion coefficients and the transition frequencies $\tilde{\omega}_{\nu,\nu'}^{\alpha,\alpha'}$ between the vibrational states ν and ν' in their respective electronic states α and α' are given by:

$$\tilde{\omega}_{\nu,\nu'}^{\alpha,\alpha'} = \tilde{\omega}_{\nu}^{\alpha} - \tilde{\omega}_{\nu'}^{\alpha'}.$$

Unlike pulse 1, the probing pulses 2 and 3 must be perturbative. Using the electric field $E_2(t)$ of pulse 2, we find:

$$\left| {}_k\psi_b^{(2)}(\tau) \right\rangle_{t_3} = -\frac{i}{\hbar} \int_{-\infty}^{t_3} dt_2 e^{-i\hat{H}(t_3-t_2)/\hbar} E_2(t_2) \hat{d} \left| {}_k\psi_a^{(1)}(\tau) \right\rangle_{t_2}, \quad (4.3)$$

where \hat{H} is the field-free, molecular Hamiltonian and \hat{d} is the scalar product of the dipole moment operator and the electric field's polarization vector. The corresponding expression for $\left| {}_k\psi_c^{(3)}(\tau) \right\rangle_t$ can be found similarly:

$$\begin{aligned} \left| {}_k\psi_c^{(3)}(\tau) \right\rangle_t = & -\frac{1}{\hbar^2} \int_{-\infty}^t dt_3 \int_{-\infty}^{t_3} dt_2 e^{-i\hat{H}(t-t_3)/\hbar} E_3(t_3) \hat{d} \\ & \times e^{-i\hat{H}(t_3-t_2)/\hbar} E_2(t_2) \hat{d} \left| {}_k\psi_a^{(1)}(\tau) \right\rangle_{t_2}. \end{aligned} \quad (4.4)$$

We introduce the Fourier transforms of the electric fields:

$$E_r(t_r) = \int_{-\infty}^{\infty} d\omega_r \mathcal{E}_r(\omega_r) e^{-i\omega_r t_r}, \quad r = 2, 3. \quad (4.5)$$

Furthermore, we use partial identities resolved on the vibrational states ν of the electronic state α , including both bound and continuum states:

$$\hat{I}_{\alpha} = \sum_{\nu} |\phi_{\alpha,\nu}\rangle \langle \phi_{\alpha,\nu}|. \quad (4.6)$$

To be a full identity, the sum should have also included all other electronic states. However, we can make this restriction because we demanded that the pulses 2-3 are spectrally narrow enough to cause transitions only into the certain

electronic states shown in Fig. 4.2. For example, a partial identity \hat{I}_b could be inserted immediately to the left of the operator \hat{d} in Eq. (4.3).

Finally, we denote the dipole transition moments between the vibrational levels ν and ν' in their respective electronic states α and α' :

$$\mathfrak{D}_{\nu,\nu'}^{\alpha,\alpha'} = \langle \phi_{\alpha,\nu} | \hat{d} | \phi_{\alpha',\nu'} \rangle. \quad (4.7)$$

We use Eqs. (4.5)-(4.7) with Eq. (4.4) and perform the time integrals. To accomplish this, we make use of the usual trick of letting $\tilde{\omega}_{m,l}^{b,a}$ and $\tilde{\omega}_{n,l}^{c,a}$ have a small negative imaginary part caused by decays, whereby the integrals converge.

$$\begin{aligned} \left| {}_k\psi_c^{(3)}(\tau) \right\rangle_t &= e^{i\theta_k} \frac{1}{\hbar^2} \sum_{l,m,n} \mathfrak{D}_{m,l}^{b,a} \mathfrak{D}_{n,m}^{c,b} \int_{-\infty}^{\infty} d\omega_2 \int_{-\infty}^{\infty} d\omega_3 \\ &\quad \times \frac{\mathcal{E}_2(\omega_2) \mathcal{E}_3(\omega_3) e^{-i(\omega_2+\omega_3+\tilde{\omega}_l^a)t}}{(\omega_2 + \tilde{\omega}_{l,m}^{a,b}) (\tilde{\omega}_{n,l}^{c,a} - \omega_2 - \omega_3)} e^{i\tilde{\omega}_{l,k}^{a,0}\tau} {}_k\beta_l |\phi_{a,l}\rangle, \end{aligned}$$

One may note in passing that if the dominating effect of pulse 2 is to stimulate emission as shown in Fig. 4.2, the transition frequencies $\tilde{\omega}_{l,m}^{a,b}$ are positive and the negative frequency components of $\mathcal{E}_2(\omega_2)$ will give the dominating contribution to the ω_2 -integral.

The electric field of the *FW* pulse is proportional to the second time derivative of the dipole moment

$$\begin{aligned} E_{FW}(t, \tau) &= \sum_k {}_kE_{FW}(t, \tau) \\ &\propto \sum_k \frac{d^2}{dt^2} [{}_kd(t, \tau)]. \end{aligned}$$

This yields for the contribution caused by the k 'th initially populated level:

$$\frac{d^2}{dt^2} [{}_kd(t, \tau)] = \frac{d^2}{dt^2} \left\langle {}_k\psi_c^{(3)}(\tau) | \hat{d} | {}_k\psi_0^{(0)} \right\rangle_t. \quad (4.8)$$

Please note that we only have to use the same k 'th vibrational state from the initial thermal state, since inner products with all other terms vanish (see section 4.3). Using this result, we can find the frequency dependence of the *FW*

pulse's electric field:

$$\begin{aligned}
\frac{{}_k\mathcal{E}_{FW}(\omega, \tau)}{\omega^2} &\propto {}_k\tilde{d}(\omega, \tau) \\
&= \frac{1}{2\pi} \int_{-\infty}^{\infty} dt e^{i\omega t} {}_k d(t, \tau) \\
&= \sum_l {}_k C_l^*(\omega) e^{i\tilde{\omega}_{k,l}^{0,a} \tau} {}_k \beta_l^*, \tag{4.9}
\end{aligned}$$

where the mapping coefficients ${}_k C_l(\omega)$ (and their complex conjugates) depend upon the lifetime of the energy levels and the detailed electric fields of the pulses 2 and 3:

$$\begin{aligned}
{}_k C_l^*(\omega) &= \frac{1}{\hbar^2} \sum_{m,n} \frac{\mathfrak{D}_{l,m}^{a,b} \mathfrak{D}_{m,n}^{b,c} \mathfrak{D}_{n,k}^{c,0}}{\omega + \tilde{\omega}_{n,k}^{c,0}} \\
&\quad \times \int_{-\infty}^{\infty} d\omega_2 \frac{\mathcal{E}_2^*(\omega_2) \mathcal{E}_3^*(\tilde{\omega}_{k,l}^{0,a} - \omega_2 - \omega)}{\omega_2 + \tilde{\omega}_{l,m}^{a,b}}. \tag{4.10}
\end{aligned}$$

This expression clearly shows the transitions $a \rightarrow b \rightarrow c \rightarrow 0$ through the \mathfrak{D} -factors and the resonance frequencies in the ω -dependent denominators. The apparent divergencies are not realistic, but a usual artifact of applying perturbation theory. We used non-overlapping pulses 2 and 3 here, but had these pulses been overlapping, Eq. (4.10) would be supplemented by a term from another process stated in section 4.6. The most important characteristic of Eq. (4.9) is its linearity in our sought coefficients ${}_k \beta_l^*$, and the exponential τ -dependence.

It is instructive to consider the limit where there is no decay and all incoming pulses are well separated in time as shown in Fig. 4.1:

$$\begin{aligned}
{}_k C_l^*(\omega) &= \frac{-(2\pi)^3}{\hbar^2} \sum_{m,n} \mathfrak{D}_{l,m}^{a,b} \mathfrak{D}_{m,n}^{b,c} \mathfrak{D}_{n,k}^{c,0} \\
&\quad \times \mathcal{E}_2^*(\tilde{\omega}_{m,l}^{b,a}) \mathcal{E}_3^*(\tilde{\omega}_{n,m}^{c,b}) \delta(\omega - \tilde{\omega}_{n,k}^{c,0}), \tag{4.11}
\end{aligned}$$

clearly showing the transitions shown schematically in Fig. 4.2. Rather than containing δ -functions in a realistic setting, the finite decay times will give mapping coefficients peaked close to the transition frequencies $\omega = \tilde{\omega}_{n,k}^{c,0}$. Physically, the part of the unknown state labeled by the index k can only give *FW* emission close to the frequencies $\tilde{\omega}_{n,k}^{c,0}$ because the molecule is certain to return to the original k -level after the coherent emission as shown in Fig. 4.2. Thus, if we

fix k and let $k' \neq k$, n and n' be free, a well-resolved peak at the unique frequency $\tilde{\omega}_{n,k}^{c,0} \neq \tilde{\omega}_{n',k'}^{c,0}$ will tell us about the unknown state component k without interference from other k' components. Obviously, this requires that n denotes a bound (i.e. non-continuum) vibrational state. We can now see why it is practical for the pulses not to overlap in time: Overlapping pulses 2 and 3 would give rise to another contributing FW-process described in section 4.6. This additional process turns out to cause non- k -specific emission near the frequencies $\tilde{\omega}_{l,m}^{a,b}$, potentially overlapping with the conveniently k -specific frequencies $\tilde{\omega}_{n,k}^{c,0}$. Thus, to profit from the ability to select ω to gain information about a single k -component of the unknown state, the pulses should be separated in time. These observations will be very useful in the reconstruction strategy treated in subsections 4.5.1-4.5.3.

A final observation made from Eqs. (4.10) and (4.11) is that the pulses 2 and 3 must be spectrally broad for all nonzero ${}_k\beta_l$ to give rise to an emitted field that may be measured; a requirement that is apparent from Fig. 4.2.

The measurements at our disposal are spectral intensities for each delay τ , i.e. a two-dimensional spectrogram. The measured intensity signal is found from squaring the electric field² $S(\omega, \tau) \propto |\mathcal{E}_{FW}(\omega, \tau)|^2$. Therefore, dividing the signal by ω^4 , we can find the following quantities:

$$\begin{aligned} \frac{S(\omega, \tau)}{\omega^4} &= N \left| \tilde{d}(\omega, \tau) \right|^2 \\ &= N \sum_{\substack{l,l' \\ k,k'}} {}_k C_l(\omega) {}_{k'} C_{l'}^*(\omega) {}_k \beta_l {}_{k'} \beta_{l'}^* e^{i(\tilde{\omega}_{l,l'}^{a,a} - \tilde{\omega}_{k,k'}^{0,0})\tau}, \end{aligned} \quad (4.12)$$

where the overall positive factor N is introduced for two reasons: First, we do not know the absolute populations created by the pulses, and second, we wish to avoid the difficulties connected with measuring absolute signal strengths. Eq. (4.12) is the promised relationship between the measured signal and the desired coefficients ${}_k\beta_l$. Unfortunately, we cannot write down a general formula for the inversion of Eq. (4.12), because it depends on both the physical system through its energies and decay times, and on the incoming pulses 2 and 3. Fortunately though, an inversion is often possible and we shall spend the remaining part of this section doing so.

To extract the ${}_k\beta_l$'s, a first step is to isolate single terms ${}_k C_l(\omega) {}_{k'} \beta_{l'}^*$ from the sum in Eq. (4.12). We can use Fourier transformation with respect to τ

²This surprising result is a many-particle effect - a direct consequence of the large number of uncorrelated molecules emitting the *FW*-pulse [59], [60].

to extract a single or a few terms of this type. The number of terms found from such a procedure equals the number of recurrences in the transition frequencies at the chosen frequency Ω :

$$\begin{aligned}
 F(\Omega, \omega) &= \frac{1}{2\pi} \int_{-\infty}^{\infty} d\tau \frac{S(\omega, \tau)}{\omega^4} e^{-i\Omega\tau} \\
 &= N \frac{1}{2\pi} \int_{-\infty}^{\infty} d\tau \left| \tilde{d}(\omega, \tau) \right|^2 e^{-i\Omega\tau} \\
 &= N \sum'_{k, l, k', l'} C_l(\omega)_{k, l} \beta_l C_{l'}^*(\omega)_{k', l'} \beta_{l'}^*, \tag{4.13}
 \end{aligned}$$

with the primed sum running over indices (k, k', l, l') so that $\Omega = \tilde{\omega}_{l, l'}^{a, a} - \tilde{\omega}_{k, k'}^{0, 0}$. Moreover, because we required that pulse 1 preceded pulse 2, we must understand $S(\omega, \tau) = 0$ for values of τ greater than the onset time of pulse 2, see Fig. 4.1. Even though the τ -integral in Eq. (4.13) runs over all values of τ , one cannot achieve this in real experiments. Both the inevitable truncation of the τ -interval and decay processes will cause a broadening of the peaks in $F(\Omega, \omega)$ as a function of Ω , in turn leading to an increased number of frequency recurrences. Although a valid concern, we will postpone a discussion to section 4.6, and assume for now that it is possible to use Eq. (4.13) to find sums with just a single or a few terms. We will aim to extract single terms from these sums. Obviously, choosing $\Omega = 0$ gives many terms, among them the ones with $l = l'$, making it difficult to extract any single one. Fortunately, it will turn out that we will not need these, so we shall henceforth look for terms with $l \neq l'$.

To select out a single or a few terms from the function $F(\Omega, \omega)$ in Eq. (4.13) we must make appropriate choices of the variables Ω and ω . In the following subsection 4.5.1, we shall present a method to do this when proper choices of ω can select out a certain k : case (I). Furthermore, the methods developed in this subsection will allow us to treat the more complicated situations that follow. In subsection 4.5.2 we describe the reconstruction method for case (I), which involves introducing a calibration pulse. In subsection 4.5.3 we present how to deal with the remaining k through making a weak assumption on the spectrum - case (II). Finally, in subsection 4.5.4, we propose to use spectrograms at different temperatures if the two above methods fail.

4.5.1 Case (I) : Emission due to a single initially populated level k

We turn our focus to the group of k states that belong to case (I). Expressing the situation physically, case (I) is when we can find values of ω for which the

signal is the same as if the initial state was the pure state $|\psi_0^{(0)}\rangle$, see Eq. (4.1). Recalling Eqs. (4.10) and (4.11), one would seek such ω close to the frequencies $\tilde{\omega}_{n,k}^{c,0}$, where k is fixed and n is free. In the decay-free language of Eq. (4.11) and Fig. 4.2, we look among the transition frequencies for transitions from a bound vibrational state n in the electronic state c to the vibrational state k in the electronic state 0. If decoherence processes are not too fast, one can still find such ω in the general case, illustrated in Fig. 4.4.

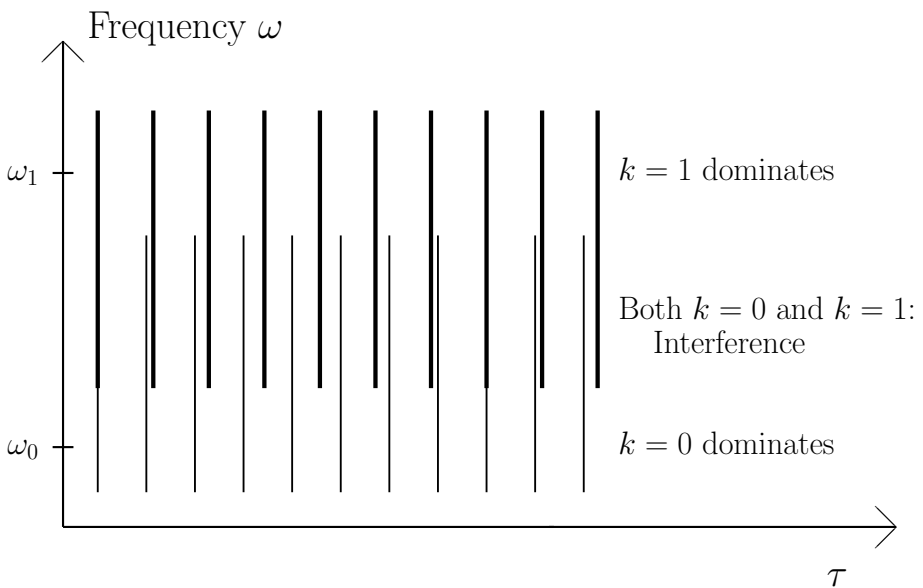


Figure 4.4: Schematic illustration of part of a spectrogram Eq. (4.13) in case (I): There are regions of ω where only a single k contributes. The vertical lines signify maxima in the signal $S(\omega, \tau)/\omega^4$, with contributions from different initial levels explicitly shown. To extract the numbers ${}_k\beta_l$ from the sum Eq. (4.13), one can choose ω to select k . In the example shown in this figure, one can extract information about $k = 0$ from using the data with $\omega = \omega_0$. Thus, the one-dimensional data $S(\omega_0, \tau)/\omega^4$ can be used in Eq. (4.13) to find ${}_0\beta_l$. Similarly, fixing the frequency at $\omega = \omega_1$ allows one to obtain information about the coefficients ${}_1\beta_l$.

Having identified a set of candidate frequencies for ω , it may be possible to

reduce this further if the central frequency and spectral width of the pulses 1-3 are known. Considering Fig. 4.2 or Eq. (4.11), one can get at good idea of the spectral range of the FW radiation. Whatever the set of frequencies one ends up with, it is necessary to have a way to test whether only one k contributes at each of them. In the usual experimental situation where the signal $S(\omega, \tau)$ is simultaneously recorded for all frequencies ω in a wide range, we also know $F(\Omega, \omega)$ for this range of ω . To find out if only one k contributes at a fixed ω , one simply tests whether $F(\tilde{\omega}_{l,l'}^{a,a} - \tilde{\omega}_{k,k'}^{0,0}, \omega) = 0$ for all $k' \neq k$. Such a test was used for a similar purpose in [57].

Though one such ω could be enough, we will see below that more may be required. Before going further, one should note the remarkable in that emission at as little as a single frequency can contain all information about the complex unknown vibrational state excited from the initial state k . Dissimilarly, the identity of this unknown state is contained in the one-frequency emission's variation with the delay τ , or equivalently Ω . Having chosen the proper ω , we proceed to reconstruct the unknown state by looking at the Ω -dependence of Eq. (4.13).

Let us choose the frequency $\Omega = \tilde{\omega}_{l,l'}^{a,a}$, whereby the primed sum Eq. (4.13) runs over only l and l' and $k' = k$ is fixed due to our choice of ω . If there are degeneracies in the frequencies $\tilde{\omega}_{l,l'}^{a,a}$, it can still be possible to find the elements indirectly. Since the details depend on the problem at hand, we illustrate this with an example.

Say, $\tilde{\omega}_{l_1,l'_1}^{a,a} = \tilde{\omega}_{l_2,l'_2}^{a,a}$, and we have Fourier transformed the signal to find the following sum, suppressing the k -index and ω -variable for clarity:

$$F(\Omega) = NC_{l_1}\beta_{l_1}C_{l'_1}^*\beta_{l'_1}^* + NC_{l_2}\beta_{l_2}C_{l'_2}^*\beta_{l'_2}^*. \quad (4.14)$$

Provided that we can find each of the following coefficients and that none of them are zero, we can form the quotient:

$$\frac{NC_{l_1}\beta_{l_1}C_{l'_3}^*\beta_{l'_3}^* \times NC_{l'_3}\beta_{l'_3}C_{l'_1}^*\beta_{l'_1}^*}{NC_{l'_3}\beta_{l'_3}C_{l'_3}^*\beta_{l'_3}^*} = NC_{l_1}\beta_{l_1}C_{l'_1}^*\beta_{l'_1}^*,$$

allowing us to extract each of the terms in Eq. (4.14). Thus, we can use intermediate levels to obtain each term in sums, otherwise hidden because of the degeneracy in the transition energies.

In principle, we could similarly find all such products $NC_l\beta_lC_{l'}^*\beta_{l'}^*$, including $l = l'$. Though having all these products would permit a nice statistical treatment through singular value decomposition of the outer product matrix, it could easily prove impossible to measure them all due to the finite spectral

width of the pulses 2 and 3. Fortunately, we can do with only a few because of our freedom of choosing normalization and phase of each $\left| {}_k\psi_a^{(1)} \right\rangle$, as will be clear below.

We have now reached the limit of what we can extract from the (ω, τ) -spectrograms. To find the unknown quantum state through the expansion coefficients β_l 's, we need to know the corresponding mapping coefficients $C_l(\omega)$'s. These are in turn both difficult to calculate, one reason being the regularization of the apparent divergencies in Eq. (4.10), and more importantly require detailed knowledge of the electric fields of the pulses 2 and 3, of the dipole matrix elements $\mathfrak{D}_{\nu, \nu'}^{\alpha, \alpha'}$ and of the transition frequencies $\omega_{\nu, \nu'}^{\alpha, \alpha'}$. One may rightly argue that with the knowledge of the dipole transition moments, it would have been easier simply to measure the field of the single pulse 1 and simply calculate the unknown quantum state by propagation using the dynamical laws. Therefore, we shall take a completely different approach which circumvents both regularizations, detailed knowledge of electric fields, and knowledge of transition matrix elements and -energies between excited states.

4.5.2 Calibration pulse

In this subsection, we introduce one or more calibration pulses aimed at creating excited quantum states in the electronic level a with known calibration expansion coefficients ${}_k\beta_l^{\text{cal}}$. This is a different approach than heterodyne detection or other reference pulse techniques, since the calibration experiment is a separate experiment from the one where the reconstruction data are recorded. Hence, by performing exactly the same experiments as above, except with the calibration pulse substituted for pulse 1, we will find products of the form $N_C {}_k C_l(\omega) {}_{k'} C_{l'}^*(\omega)$. These will in turn be used in the reconstruction experiment with pulse 1 to find the coefficients ${}_k\beta_l$. Let us consider this in detail.

Contrary to pulse 1, we will require that the calibration pulse(s) be perturbative, because this gives simple expressions for the state created in the calibration. We find this state similarly to Eq. (4.3), letting the upper limit in the integration tend to infinity since the electric field $E_{\text{cal}}(t' + \tau)$ vanishes for

times long before the pulses 2 and 3 are turned on:

$$\begin{aligned}
|{}_k\psi_a^{\text{cal}}(\tau)\rangle_{t_2} &= -\frac{i}{\hbar} e^{i\theta_k} \int_{-\infty}^{\infty} dt' e^{-i\hat{H}_a(t_2-t')/\hbar} E_{\text{cal}}(t' - \tau) \\
&\quad \times \hat{d} e^{-i\hat{H}_0(t'-0)/\hbar} |{}_k\psi_0^{(0)}\rangle_0 \\
&= -\frac{i}{\hbar} e^{i\theta_k} \sum_l \mathfrak{D}_{l,k}^{a,0} \mathcal{E}(\tilde{\omega}_{l,k}^{a,0}) |\phi_{a,l}\rangle e^{i\tilde{\omega}_{l,k}^{a,0}\tau} e^{-i\tilde{\omega}_l^a t_2}. \quad (4.15)
\end{aligned}$$

Comparing Eq. (4.15) to Eq. (4.2), we see that the expansion coefficients of the calibration state are

$${}_k\beta_l^{\text{cal}} = -\frac{i}{\hbar} \mathfrak{D}_{l,k}^{a,0} \mathcal{E}(\tilde{\omega}_{l,k}^{a,0}). \quad (4.16)$$

Thus, by knowing the dipole transition elements $\mathfrak{D}_{l,k}^{a,0}$ and the frequency components of the electric field of a calibration pulse, we can calculate the expansion coefficients of the vibrational calibration state created in the electronic state a . For convenience, one can merely use a calibration pulse that has a constant spectrum over the relevant frequencies $\tilde{\omega}_{l,k}^{a,0}$, giving calibration expansion coefficients of the levels according to the values of the dipole transition matrix elements. It is therefore not necessary to have detailed information about the calibration pulses, but we must know the transition dipole matrix elements between the electronic states 0 and a . Fortunately, these are typically readily measured, e.g. by fluorescence spectroscopy, or calculated. In contrast, we do not need to know the similar elements between two excited states.

In the remaining part of this subsection we will be considering a single k , and we shall suppress this index for clarity.

For the calibration to be useful, the calibration data recorded must enable us to determine the β_l 's up to a common non-zero complex factor. We will accomplish this by determining products $\beta_l\beta_{l'}^*$ up to an overall complex factor, common for all products. The measurements with pulse 1 gives quantities $N_1 C_l(\omega)\beta_l C_{l'}^*(\omega)\beta_{l'}^*$, precisely allowing us to determine $N_1\beta_l\beta_{l'}^*$ if we know $C_l(\omega)C_{l'}^*(\omega)$. These mapping coefficient products can in turn be found, up to a common factor N_C , from the calibration data $N_C C_l(\omega)\beta_l^{\text{cal}} C_{l'}^*(\omega)\beta_{l'}^{\text{cal},*}$, where the β_l^{cal} 's are known. By division, we can then find products of the form $N'\beta_l\beta_{l'}^*$. To determine the β_l 's individually, we simply set one of these equal to one, use the products to determine the rest, and finally normalize. Therefore, there is no benefit in knowing one of these products where neither l or l' enter in another product. Consequently, we must know the range of l 's that are populated by

pulse 1 (an estimate can be found from its spectral center and width) and be able to find products $N_l \beta_l \beta_l^*$, where all populated l 's enter, and no product has both an l and an l' that do not enter in another. To accomplish this, one is free to use data from more than one value of ω , as long as each data set can be related to data at all other values of ω . This is sufficiently fulfilled if one can determine a product $N_C C_l(\omega) C_{l'}^*(\omega)$ at one value of ω that contains an l also contained at in a product at another value of ω .

In case it is not convenient to populate all these levels with a single calibration pulse, more can be used in subsequent calibrations. Since we can allow for only a single undetermined overall complex factor, it is necessary to relate the data from one calibration pulse to the others. For instance, it is sufficient to determine a single $N_{C1} C_l(\omega) C_{l'}^*(\omega)$ from one calibration $C1$ which can also be determined in another calibration $C2$ to find the ratio N_{C1}/N_{C2} .

All this having been said, we illustrate the procedure with a brief example. Let us say that we are interested in reconstructing the vibrational state originating in a certain k (which we suppress for clarity), and we desire the expansion coefficients β_l with $l \in \{1, 2, 3, 4, 5\}$. We employ two calibration pulses $C1$ and $C2$. $C1$ has a constant spectrum in a range sufficient to populate levels 1-4 and $C2$ similarly populates levels 3-5. Measuring at the two frequencies ω_a and ω_b where other $k' \neq k$ give only negligible contributions, it is found that there is good signal strength for the following terms:

$$\left. \begin{array}{l} N_{C1} C_1(\omega_a) C_2^*(\omega_a) \\ N_{C1} C_2(\omega_a) C_4^*(\omega_a) \\ N_{C1} C_3(\omega_b) C_4^*(\omega_b) \end{array} \right\} \text{pulse } C1$$

$$\left. \begin{array}{l} N_{C2} C_3(\omega_b) C_4^*(\omega_b) \\ N_{C2} C_3(\omega_b) C_5^*(\omega_b) \end{array} \right\} \text{pulse } C2$$

where we have already divided out the known calibration expansion coefficients $\beta_l^{\text{cal}} \beta_{l'}^{\text{cal},*}$, up to a factor absorbed in the N_C 's. The element $C_3(\omega_b) C_4^*(\omega_b)$ recurring in both pulses serves the special purpose of relating the two pulses by showing us the ratio of the numbers N_{C1} and N_{C2} . Hereafter, the actual experiment is performed with pulse 1. In the table below, we show how one obtains the products $N_l \beta_l \beta_l^*$ from measurements and calibration data.

Measurement:	Used calibration:	We find:
$N_1 C_1(\omega_a) \beta_1 C_2^*(\omega_a) \beta_2^*$	$N_{C1} C_1(\omega_a) C_2^*(\omega_a)$	$N' \beta_1 \beta_2^*$
$N_1 C_2(\omega_a) \beta_2 C_4^*(\omega_a) \beta_4^*$	$N_{C1} C_2(\omega_a) C_4^*(\omega_a)$	$N' \beta_2 \beta_4^*$
$N_1 C_3(\omega_b) \beta_3 C_4^*(\omega_b) \beta_4^*$	$N_{C1} C_3(\omega_b) C_4^*(\omega_b)$	$N' \beta_3 \beta_4^*$
$N_1 C_3(\omega_b) \beta_3 C_4^*(\omega_b) \beta_4^*$	$N_{C2} C_3(\omega_b) C_4^*(\omega_b)$	$N' \beta_3 \beta_4^*$
$N_1 C_3(\omega_b) \beta_3 C_5^*(\omega_b) \beta_5^*$	$N_{C2} C_3(\omega_b) C_5^*(\omega_b)$	$N' \beta_3 \beta_5^*$

Since we have the freedom of choosing the normalization constant N' , we can arbitrarily set $\beta_1 = 1$, from which we can use the following lines in the table to find (in order) $N' \beta_2$, $N' \beta_4$, $N' \beta_3$, and from the last line $N' \beta_5$. Finally, the state can be normalized by appropriately choosing N' . We have thus found the set of complex numbers $\{\beta_i\}$, both their magnitude and phase, and we have thereby performed the reconstruction of the state formed by pulse 1.

Having been concerned with how to use small sets of measurements, it should be said that an experiment may well yield much more data than is minimally required. Such an abundance of data can be used to further improve the statistics of the reconstructed values.

Finally, it may be of note that we can easily find the individual mapping coefficients $C_l(\omega)$ from the calibration data, up to a common factor, rather than just products of two coefficients. This is done in the exact same way as finding the $\{\beta_i\}$, i.e. by setting one of the $C_l(\omega) = 1$, and using the products to find the rest. Thereby dynamical information about the molecule can be obtained.

4.5.3 Case (II) : Interference between different initial vibrational states

We turn our attention to case (II) where the contribution from all initial vibrational states, labeled by each their k , cannot be isolated from Eq. (4.13) by proper choice of the emitted FW frequency ω . This situation is illustrated in Fig. 4.5 for two initially populated k -levels. Here the wave-packet originating in $k = 1$ cannot be found by the above procedure.

However, if just a single k can be isolated by choosing $\omega = \omega_0$, we can by the above method find the ${}_0\beta_i$'s for this $k = 0$ up to a common phase factor³. In this subsection we describe how the ${}_{k \neq 0}\beta_i$ can be found if the spectrum fulfills certain conditions. For transparency, we initially focus on the situation

³It is assumed here, for clarity, that the $\{\beta_i\}$ can be reconstructed from the measurements at the frequency ω_0 . More generally, we can think of a set of frequencies $\{\omega_0\}$ wherefrom the $\{\beta_i\}$ can be reconstructed.

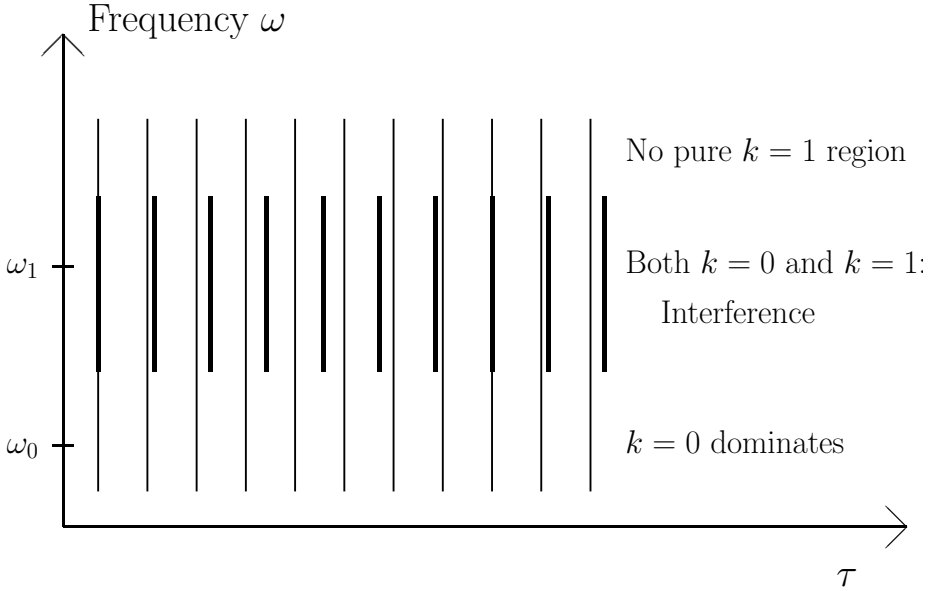


Figure 4.5: Schematic illustration of a part of a spectrogram Eq. (4.13) in case (II). The vertical lines signify maxima in the signal $S(\omega, \tau)/\omega^4$, with contributions from different initial levels explicitly shown. In contrast to Fig. 4.4, we cannot find values of ω for which only $k = 1$ contributes. However, one can find the ${}_0\beta_l$'s through the procedure described in section 4.5.2. These coefficients can afterwards be used to extract the ${}_1\beta_l$ by using the frequencies $\Omega = \tilde{\omega}_{l,l'}^{a,a} - \tilde{\omega}_{k=0,k'=1}^{0,0}$ in Eq. (4.13), provided that enough of these frequencies can be spectrally resolved from the frequencies $\tilde{\omega}_{l,l'}^{a,a}$. Explicitly, the extracted terms in $F(\Omega, \omega)$ arise from optical interferences between the $k = 0$ and $k' = 1$ signals. If there are more overlapping k' signals than the two shown, it may be possible to extract these ${}_{k'}\beta_l$ by similar means.

in Fig. 4.5 where we seek the coefficients ${}_1\beta_l$. For our method to work, we demand that some of the frequencies $\Omega_{l,l'}^{0,1} = \tilde{\omega}_{l,l'}^{a,a} - \tilde{\omega}_{k=0,k'=1}^{0,0}$, arising from optical interferences between $k = 0$ and $k = 1$, must be spectrally resolved from the pure $k = 0$ and $k = 1$ signals having $\Omega_{l,l'}^{k,k} = \tilde{\omega}_{l,l'}^{a,a}$. Having this requirement fulfilled, we can extract the quantities $F(\Omega_{l,l'}^{0,1}, \omega_1) = {}_0C_l(\omega_1) {}_0\beta_l {}_1C_{l'}^*(\omega_1) {}_1\beta_{l'}^*$. In the calibration experiment, we can hence determine the mapping coefficient product ${}_0C_l(\omega_1) {}_1C_{l'}^*(\omega_1)$ up to a common multiplicative factor and, by using the ${}_0\beta_l$ found in the experiment (using $\omega = \omega_0$), we can find ${}_1\beta_{l'}$ (using $\omega = \omega_1$).

Similarly to case (I), we do not require spectral resolution of all frequencies $\Omega_{l,l'}^{0,1}$ and $\Omega_{l,l'}^{k,k}$. Indeed, to determine all ${}_1\beta_{l'}$, we may need as little as one resolvable $\Omega_{l,l'}^{0,1}$ for each l' at some ω_1 , and that the corresponding ${}_0\beta_l$ is non-zero.

If more than two values of k overlap, these can be found through similar means; either by their interference with $k = 0$ or recursively, i.e. $k + 1$ is found from k . In conclusion, it is with these assumption possible to reconstruct the state in case (II) also.

4.5.4 Case (III) : Variation of temperature

The treatments of the cases (I) and (II) above were based on the assumption that at least a single k can be isolated from $F(\Omega, \omega)$ by appropriately choosing ω . If such an ω cannot be found, the situation is radically different. Still maintaining that we wish to avoid making assumptions about the mapping coefficients ${}_kC_l(\omega)$, one idea to a solution is to perform several experimental runs at different temperatures of the initial state. Still neglecting rotations, there are two main effects that change the spectrograms as the temperature is varied: Temperature dependent decoherence processes and thermal populations in the initial state. The most important decoherence process will usually be collisional decoherence (pressure broadening), with a smaller contribution from Doppler broadening. In any case, these two effects broaden the spectral lines, scaling as \sqrt{T} for fixed particle density, where T is the absolute temperature. For moderate temperature ranges, this is only a small effect; indeed we can ignore it altogether as long as the required spectral resolution is not washed out. In contrast, the initial state populations scale exponentially with $1/T$, possibly greatly changing the spectrogram. It is exactly this change we could use to our advantage. Thus, the terms in Eq. (4.13) having $k = k'$ will scale differently with temperature for each k , and differently from terms with $k \neq k'$. These variations with temperature simply follow the Boltzmann distribution

corresponding to the energy of the k 'th level in the initial thermal state. By forming linear combinations of $F(\Omega, \omega)$ recorded at different temperatures with weights calculable from the corresponding Boltzmann distributions, one can separate out the terms for each $k = k'$ and each $k \neq k'$. For example, if k_1 and k_2 both enters in Eq. (4.13), one could find all the terms individually; i.e. terms containing (k_1, k_1) , (k_2, k_2) and (k_1, k_2) . Consequently, it could be possible to modify the above reconstruction method so it can be used, even if all k cannot be selected individually by choosing special values of ω .

4.6 Discussion

Having presented above a specific implementation of the reconstruction method, we will in subsection 4.6.1 discuss the validity of neglecting rotations. Hereafter, we will in subsection 4.6.2 discuss the assumptions made in section 4.4 and possible generalizations of the method.

4.6.1 Rotations

We completely neglected rotations in the above. Nevertheless, if more than a single vibrational level is initially thermally populated, many rotational levels herein will be too. This comes about because rotational energy levels are much more closely spaced in energy than vibrational levels. For concreteness, we will use the example of a diatomic molecule where the rotational energy in the electronic state α is $E_{rot,\alpha} = B_\alpha J(J+1)$. Here, J is the angular momentum quantum number and B_α is the rotational constant. If rotational states up to a certain J_{max} are initially appreciably populated, the number of rotational states involved is circa $(J_{max} + 1)^2$. In the experiments on gaseous iodine in [57] and [58] where the two lowest vibrational states are appreciably populated, the number of entering rotational states will be large - of the order $N_{rot} \approx 10^4$, and $J_{max} \approx 100$. All the ro-vibrational levels are initially incoherently populated, and we can label each of them after their initial quantum number J and its projection M ; The initial state is therefore incoherent in all of the indices k, J and M . Thus, by analogy with Eq. (4.8), the dipole moment leading to coherent FW emission only contains contributions of the form ${}_{k,J,M}d(t, \tau) = {}_t\langle {}_{k,J,M}\psi_c^{(3)}(\tau) | \hat{d} | {}_{k,J,M}\psi_0^{(0)} \rangle_t$. For linearly polarized pulses, each of the one-photon transitions shown in Fig. 4.2 changes J by 0 or ± 1 while M

is conserved⁴. Both such J -changing transitions and the difference in rotational constants B_α in the different electronic states will lead to a splitting of the frequencies $\tilde{\omega}_{l,l'}^{a,a} - \tilde{\omega}_{k,k'}^{0,0}$ in Eq. (4.12) into many $\tilde{\omega}_{(l,J_1),(l',J'_1)}^{a,a} - \tilde{\omega}_{(k,J_2),(k',J'_2)}^{0,0}$, where J_1 and J_2 differ by at most 1, likewise J'_1 and J'_2 . Due to the closeness of the rotational levels, these will often not be experimentally resolved by their values of J -indices, but will rather give a considerable broadening of the Ω -peaks near $\tilde{\omega}_{l,l'}^{a,a}$ in our data $F(\Omega, \omega)$. Even if we assume the mapping coefficients to depend negligibly on the rotational indices, these broadenings could be as large as the frequency difference between neighboring $\tilde{\omega}_{l,l'}^{a,a}$, impairing our ability to extract certain (l, l') -terms in Eq. (4.13) by choosing certain values of Ω .

Similarly, the frequencies $\tilde{\omega}_{(n,J),(k,J')}^{c,0}$ we used to select k will have many rotational contributions. Even if they are not experimentally resolved, they may well be distinguishable in principle, disallowing optical interferences. This was observed in the iodine experiment [57] due to long decay times. Like in case (I), the consequence is that the sum Eq. (4.13) has nonzero terms for initial indices $(k, J) = (k', J')$ only. Equivalently, the measured signal appears as if one added intensities for different initial levels rather than electric fields. Even though this greatly reduces the number of terms in Eq. (4.13), the lines close to $\tilde{\omega}_{n,k}^{c,0}$ could be broadened to the extent of considerably overlapping with its neighbours, impairing our ability to extract a certain k by choosing certain values of ω .

Conclusively, rotational degrees of freedom lead to broader lines in both arguments of our data $F(\Omega, \omega)$, Eq. (4.13), possibly to the point of preventing reconstruction through the methods in subsections 4.5.1-4.5.4. Therefore, an experiment would be required to prove the practical feasibility of our proposed reconstruction method.

4.6.2 Generalizations of the method

Neglecting rotations again, we turn to the other assumptions made in section 4.4 and the possible generalizations of the method. All of these generalizations are centered around the use of calibration and around the linearity in expansion coefficients arising because of the perturbative character of the pulses 2 and 3, see e.g. Eq. (4.9).

First, is easy to see that this structure will be the same regardless of whether

⁴Whether $\Delta J = 0$ is allowed depends on the symmetry of the electronic states $0 - c$. In the diatomic case, $\Delta J = 0$ requires one of the involved states in a one-photon transition to have non-zero electronic angular momentum.

we are restricted to dipole transitions or also include higher multi-pole transitions. While this may not be of much relevance in four-wave mixing experiments, it shows the general principle: While the mapping coefficients ${}_k C_l(\omega)$ become more complicated, they are still fully accounted for because of the use of calibration pulses.

Second, we turn to the assumption made in Fig. 4.2 and in section 4.5 that the photon from pulse 2 enters the interaction before the photon from pulse 3. If there were temporal overlap of the probe pulses 2 and 3, a major contribution to the *FW* electric field can be caused by an inner product of the form $\langle {}_k \psi_a^{(1)}(\tau) | \hat{d} | {}_k \psi_b^{(2)} \rangle$. Here, $| {}_k \psi_b^{(2)} \rangle$ is independent of τ , and is formed from the initial state by absorption of a photon from pulse 2 followed by stimulated emission of a photon to pulse 3⁵. This poses no problem for the structure of Eq. (4.9): Like other energetic paths, this preserves the linearity in the ${}_k \beta_l$'s and the signal's dependence on τ . Nonetheless, as we remarked in subsection 4.5.1, the process can cause difficulties in the reconstruction procedure of case (I) and (II). These difficulties arise because this process will lead to non- k -specific *FW* emissions with frequencies close to $\tilde{\omega}_{l,m}^{a,b}$. If these frequencies are too close to the frequencies $\tilde{\omega}_{n,k}^{c,0}$ to be resolved, we cannot use the latter as fingerprints of individual k labels, and the methods of section 4.5.1 and 4.5.3 fail. An important example of this is the experiments in [57] and [58], where the electronic levels $0 = b$ and $a = c$. Therefore, whether the assumption of separated pulses can be relaxed depends on the transition frequencies of the physical system.

Third, if the molecular electronic levels are conveniently spaced, one can use another number of pulses for the above procedure, down to a minimum of two (one for excitation and one for probing). The special importance of the *FW* situation is that it uses the smallest number of pulses in the widespread situation where only two electronic levels $0 = b$ and $a = c$ are used. Though our method allows for different numbers of incoming pulses, the non-co-linear geometry still plays an important role. Its advantage lies not in selecting certain electronic states, but rather in avoiding the strong background from pulses 1-3 and in giving a reasonably simple way of finding the ω that allows us to select a certain $k' = k$ in Eq. (4.13).

Fourth, it is unnecessary that the electronic indices 0 and $a-c$ denote single electronic states. These could as well be groups of states, well separated

⁵One might be surprised that an *FW* process where photons are absorbed from the pulses 1 and 2, and a photon is emitted to pulse 3, can give emission in the same direction as the process treated in section 4.5 (absorption from pulses 1 and 3, emission to pulse 2). The correctness of this can be found from considerations identical to those near the end of section 4.4, where the center of mass' translational state is taken into account.

in energy, where the vibrational indices k - n simply denotes all the close-lying states in these groups. With this generalization it also becomes apparent that we do not need to make the Born-Oppenheimer approximation to maintain Eq. (4.9). Without this approximation, we cannot speak of vibrational and electronic states, but we make instead the more general statement that we find the quantum state in the group of energy levels labeled by a .

Fifth, the unknown state does not need to be formed by a single laser pulse. What made it convenient to use the single laser pulse 1 above, was that the BOX-configuration made it possible to distinguish the signal from the states having interacted with pulse 1 by the direction of the FW -pulse. Nevertheless, any coherent process forming an unknown state in the group of levels a will work, provided that there remains population in the original group 0 levels (i.e. the states labeled by k), and no population is transferred back to these levels by the excitation process.

Sixth and finally, there is no requirement that the different k refers to the same molecule. If one wanted to examine a weak emission from a molecule A , it could be possible to perform the above experiment on a mixture of A with another, more strongly emitting molecule B . In the spectrogram region where the signals from A and B overlap, the strong electric field from B amplify the signal from A rather like the idea of mixing a weak signal with that of a strong local oscillator in heterodyne detection. The basic principle behind this was demonstrated in [61].

By discussing these generalizations, we hope to have given the reader the impression that doing Quantum State Reconstruction by perturbative processes with calibration is a general approach with wider applicability.

In conclusion, we have proposed a method to reconstruct an unknown vibrational quantum state, coherently excited from an initial thermal state. By using one or more calibration pulses, we have shown how to circumvent knowledge of the perturbative probing process, and we have suggested that this idea may be of wider applicability in Quantum State Reconstruction.

Chapter 5

Tomographic reconstruction of quantum correlations in excited Bose-Einstein condensates

5.1 Synopsis

This chapter introduces the reader to the use of Maximum Entropy (MAXENT) density operators for Quantum State Reconstruction. In contrast to former uses of MAXENT reconstruction on single particles, we generalize the method to a many particle system: a Bose-Einstein condensate. The condensate is treated using the Bogoliubov approximation, amounting to assuming only small perturbations from a uniform cold condensate. Only single-particle measurements are performed on the condensate, so rather than a full many-particle reconstruction, we limit the reconstruction to second moments of the atomic ladder operators of the form $\langle \hat{\psi}^\dagger(x)\hat{\psi}(x') \rangle$, i.e. the one-body density operator, and $\langle \hat{\psi}(x)\hat{\psi}(x') \rangle$, anomalous second moments. We test the methods reliability and amount of data needed for reconstruction on three very different types of quantum states.

The chapter is based on the article [62].

5.2 Introduction

Bose-Einstein condensates offer countless demonstrations of macroscopic quantum effects [63], [64]. Recently, there has been growing interest in the use of condensates as quantum optical components and as atom laser beam sources. The effective use of very many of these applications requires knowledge of certain aspects of the condensate's quantum state, and several articles have dealt with theoretical calculations of the states obtained by various perturbations of a condensate.

We present here a method by which experimental data can be used to estimate characteristics of the system's quantum state. For this purpose we generalize the application of the Jaynes principle of maximum entropy (MAXENT) [29] for quantum-state tomography, as proposed in [30] and applied to single atoms in [5] and [8], to the dynamics of a condensate described in the Bogoliubov approximation. We assume that the fraction of particles in the zero-wave-number mode and the position distributions at different times after preparation of the system have been measured. It is important to note that we are not claiming that the MAXENT density operator is an approximation to the true many-body operator of the quantum state; indeed, this would surely require more than just density measurements (one-body operators). Instead, we seek to correctly predict the second moments of the atomic creation and annihilation operators $\hat{\psi}(x)$ and $\hat{\psi}^\dagger(x)$. Because these second moments of the ladder operators will be discussed extensively below, we shall call second moments of the form $\langle \hat{\psi}^\dagger(x)\hat{\psi}^\dagger(x') \rangle$ and $\langle \hat{\psi}(x)\hat{\psi}(x') \rangle$ anomalous second moments, while second moments of the form $\langle \hat{\psi}^\dagger(x)\hat{\psi}(x') \rangle$ will be referred to as normal second moments.

As examples of applying the method, three types of quantum mechanically very different states will be studied. First, we study states characterized by a single Gross-Pitaevskii wave function with small deviations from the constant value attained by the ground-state homogeneous condensate. Then, second, we apply our method to an incoherently excited system, modeled by the addition of a localized thermal component to the homogeneous condensate. Finally, as a third case, we study the method's fidelity for a system with a localized amplitude squeezed atomic field.

This chapter is organized as follows. In section 5.3 we give a description of the procedure for reconstructing the density operator of a quantum system by use of the Jaynes principle of maximum entropy. In section 5.4 we specify our assumptions about the condensate, and we introduce the Bogoliubov approximation and the general para-unitary transformation procedure. In section 5.5

we will combine the MAXENT and Bogoliubov theories. In section 5.6, we apply the machinery to the three different trial states. In section 5.7 we discuss the applicability of the method and we finally conclude the chapter in section 5.8.

5.3 The MAXENT principle in Quantum State Reconstruction

The method we use to estimate the quantum state of our system at hand is by finding the MAXENT density operator as suggested by Jaynes [29], [65].

The MAXENT principle for Quantum State Reconstructions (QSR) was used by Buzěk and Drobný to numerically show that a good approximation to the density matrix for the one-particle harmonic oscillator can be achieved using the MAXENT principle with the observations of just a few quadrature distributions¹ and the mean oscillator excitation number [30]. Later, they used the same method to reconstruct the motional state of neutral Cs atoms in an optical lattice [5]. Juhl investigated the applicability of the method to free particles [66] and recently, with Skovsen *et al.*, used MAXENT tomography to reconstruct the one-body density matrix for relative motion of a dissociating diatomic molecule from experimental data [8].

In this chapter we will extend the scope of MAXENT quantum tomography by using it to approximately reconstruct the second moments of the ladder operators, including the one-body density matrix, of a many-particle system: a condensate treated in the Bogoliubov approximation. The present chapter thus describes the first extension of MAXENT tomographic methods to systems with more than one particle.

5.3.1 The MAXENT principle for the reconstruction of density operators

The goal of the MAXENT method is to find a density operator that exactly reproduces the knowledge one has about the system while making as few assumptions as possible about degrees of freedom one has no knowledge about. A proposal for this is the maximum entropy density operator $\hat{\rho}_{ME}$ chosen for having maximal von Neumann entropy $S = -\text{Tr}(\hat{\rho} \ln \hat{\rho})$. We make this more

¹In the language of chapter 2, a few quadrature distributions means a few values of θ , see Eq. (2.4).

rigorous in the following way²:

Let a set of observables $\{\hat{G}_\nu\}$, $\nu \in \{1, 2, \dots, n\}$ be associated with a quantum system prepared in an unknown state $\hat{\rho}$. We imagine an ensemble of these quantum systems wherein there are no correlations between the subsystems of the ensemble, and we assume to have measured the ensemble expectation values $\{\bar{G}_\nu\}$ of the observables $\{\hat{G}_\nu\}$.

Unless the set of observables $\{\hat{G}_\nu\}$ constitutes the quorum there will in general be many density operators $\hat{\rho}_{\{\hat{G}\}}$ that satisfy the normalization condition $\text{Tr}(\hat{\rho}_{\{\hat{G}\}}) = 1$ and predict the measured values:

$$\text{Tr}(\hat{\rho}_{\{\hat{G}\}} \hat{G}_\nu) = \bar{G}_\nu, \quad \nu \in \{1, 2, \dots, n\}. \quad (5.1)$$

The MAXENT principle says that the most unbiased guess for the density operator approximating $\hat{\rho}$ and fulfilling these conditions is the one with maximal von Neumann entropy:

$$S(\hat{\rho}_{ME}) = \max [S(\hat{\rho}_{\{\hat{G}\}}); \forall \hat{\rho}_{\{\hat{G}\}}], \quad (5.2)$$

$$S(\hat{\rho}) = -\text{Tr}(\hat{\rho} \ln \hat{\rho}). \quad (5.3)$$

As shown by Jaynes [29] this implies a density operator of the form:

$$\hat{\rho}_{ME} = \frac{1}{Z_{\{\hat{G}\}}} \exp \left(- \sum_{\nu=1}^n \lambda_\nu \hat{G}_\nu \right), \quad (5.4)$$

with the generalized partition function

$$Z_{\{\hat{G}\}} = \text{Tr} \left[\exp \left(- \sum_{\nu=1}^n \lambda_\nu \hat{G}_\nu \right) \right], \quad (5.5)$$

and with the $\{\lambda_\nu\}$ being a set of Lagrange multipliers chosen so that $\hat{\rho}_{ME}$ in Eq. (5.4) fulfills the conditions Eqs. (5.1). Using these λ_ν 's we have the explicit form of the MAXENT density operator Eq. (5.4).

A technical difficulty arises because, in all but the most trivial circumstances, it is not feasible to analytically invert the conditions Eqs. (5.1) given Eq. (5.4) to obtain the set $\{\lambda_\nu\}$. The difficulty arises because of these equations' nonlinearity in the Lagrange multipliers $\{\lambda_\nu\}$. For implementation it is more convenient –

²The statement of the MAXENT procedure in this chapter is very similar to the one given in [5].

and we shall indeed use this procedure – to minimize the norm of the differences between measured values and values predicted by $\hat{\rho}_{ME}$ with respect to $\{\lambda_\nu\}$:

$$\begin{pmatrix} Tr \left[\hat{\rho}_{ME}(\{\lambda_\nu\}) \hat{G}_1 \right] - \bar{G}_1 \\ \vdots \\ Tr \left[\hat{\rho}_{ME}(\{\lambda_\nu\}) \hat{G}_n \right] - \bar{G}_n \end{pmatrix}. \quad (5.6)$$

This procedure was also used in [5], [8] and [30]. Here, we have given the same weight to all components of the vector of errors. One may wish to modify this if, for instance, some observations are made with a much better precision than others.

Another advantage of minimizing the norm of Eq. (5.6), allowing for a small non-zero minimal norm, is that it allows us to find an approximate density operator in the presence of small experimental errors – errors that could otherwise result in no density operator being compatible with the measured (noisy) data.

5.4 Description of the condensate

5.4.1 The Bogoliubov Hamiltonian

Let us consider a three-dimensional cold gas of atoms having mass m , occupying a volume V , and dominated by s -wave collisions where $U(r, r') = U_0 \delta(r - r')$ is the interparticle potential. Such a gas is well represented by the Hamiltonian:

$$\hat{H}_{full} = \sum_k \varepsilon_k \hat{a}_k^\dagger \hat{a}_k + \frac{g}{2} \sum_{k, k', q} \hat{a}_{k+q}^\dagger \hat{a}_{k'-q}^\dagger \hat{a}_{k'} \hat{a}_k, \quad (5.7)$$

where $\varepsilon_k = \frac{\hbar^2 k^2}{2m}$ is the free-particle energy and $g = \frac{U_0}{V}$ is the coupling constant. The operators \hat{a}_k and \hat{a}_k^\dagger are the usual boson ladder operators annihilating and creating a particle with wave vector k and having the commutation relations

$$[\hat{a}_k, \hat{a}_{k'}^\dagger] = \delta_{k, k'}, \quad (5.8)$$

$$[\hat{a}_k, \hat{a}_{k'}] = 0. \quad (5.9)$$

A Hamiltonian similar to Eq. (5.7) applies in one and two spatial dimensions with suitable redefinitions of g , depending on the confinement of the remaining coordinates [67], [68]. For simplicity, only one spatial dimension will be used in this chapter. The wave vectors k are then simply scalars and will in the following be referred to as wave numbers.

Due to the complicated dynamics of the Hamiltonian Eq. (5.7), it is often necessary to use an approximate Hamiltonian to make analytical calculations possible. We will employ the so-called Bogoliubov approximation, which is valid when the vast majority of the particles are in the zero-wave-number mode [69]:

$$\langle \hat{a}_0^\dagger \hat{a}_0 \rangle \gg \sum_{k \neq 0} \langle \hat{a}_k^\dagger \hat{a}_k \rangle. \quad (5.10)$$

Having this condition fulfilled, it is legitimate to approximate the Hamiltonian Eq. (5.7) by³

$$\begin{aligned} \hat{H} = \frac{1}{2} \sum_{k \neq 0} \left[(\varepsilon_k + gN_{tot}) (\hat{a}_k^\dagger \hat{a}_k + \hat{a}_k \hat{a}_k^\dagger) \right. \\ \left. + gN_{tot} (\hat{a}_k \hat{a}_{-k} + \hat{a}_{-k}^\dagger \hat{a}_k^\dagger) \right], \end{aligned} \quad (5.11)$$

where N_{tot} is the total number of particles in the gas. This operator is bilinear in the ladder operators and can be diagonalized by a change of basis. We will do this by using elementary linear algebra.

5.4.2 Discretization of position and momentum

We will now specify some useful technical details of our treatment. We consider an odd number ($N > 1$) of evenly spaced points in 1D coordinate space, symmetrically distributed around (and including) the origin, on an interval of length $L = N\Delta x$:

$$x_n = n\Delta x, \quad n = -M, -M+1, \dots, M, \quad (5.12)$$

where $M = \frac{N-1}{2}$. We assume that the spatial atomic density is measured on this grid; i.e., our observations will be of the form $\langle \hat{\psi}^\dagger(x_n, t) \hat{\psi}(x_n, t) \rangle$. Due to the form of the Hamiltonian Eq. (5.11), it is convenient to introduce the discrete wave numbers corresponding to the spatial discretization above:

$$k_q = q\Delta k, \quad \Delta k = \frac{2\pi}{L}, \quad (5.13)$$

where q can assume the same values as n above.

³Going directly from Eq. (5.7), we have subtracted a constant, having no physical significance.

The usual discrete Fourier transform from coordinate space $(\hat{\psi}(x_n)$ and $\hat{\psi}^\dagger(x_n))$ to wave number space $(\hat{a}(k_q)$ and $\hat{a}^\dagger(k_q))$ reads

$$\hat{a}(k_q) = \frac{1}{\sqrt{N}} \sum_{n=-M}^M \hat{\psi}(x_n) \exp(ik_q x_n), \quad (5.14)$$

$$\hat{a}^\dagger(k_q) = \frac{1}{\sqrt{N}} \sum_{n=-M}^M \hat{\psi}^\dagger(x_n) \exp(-ik_q x_n). \quad (5.15)$$

All the ladder operators in coordinate space can be arranged in a $2N \times 1$ column vector,

$$\boldsymbol{\psi} = \begin{pmatrix} \hat{\psi}(x_{-M}) \\ \vdots \\ \hat{\psi}(x_M) \\ \hat{\psi}^\dagger(x_{-M}) \\ \vdots \\ \hat{\psi}^\dagger(x_M) \end{pmatrix}, \quad (5.16)$$

and, correspondingly,

$$\boldsymbol{\psi}^\dagger = \left(\hat{\psi}^\dagger(x_{-M}), \dots, \hat{\psi}^\dagger(x_M), \hat{\psi}(x_{-M}), \dots, \hat{\psi}(x_M) \right). \quad (5.17)$$

In this chapter, we shall denote vectors of this type by bold letters. Similarly, we can construct the column vector \boldsymbol{a} from the operators in wave number space $\hat{a}(k_q)$ and $\hat{a}^\dagger(k_q)$:

$$\boldsymbol{a} = \begin{pmatrix} \hat{a}(k_{-M}) \\ \vdots \\ \hat{a}(k_M) \\ \hat{a}^\dagger(k_{-M}) \\ \vdots \\ \hat{a}^\dagger(k_M) \end{pmatrix}, \quad (5.18)$$

Using these vectors, we can write the Fourier transformation Eqs. (5.14) and (5.15) as a matrix multiplication by a $2N \times 2N$ matrix:

$$\boldsymbol{a} = \mathcal{A} \cdot \boldsymbol{\psi}, \quad \text{whereby} \quad \boldsymbol{a}^\dagger = \boldsymbol{\psi}^\dagger \cdot \mathcal{A}^\dagger. \quad (5.19)$$

Here and in the following, we shall use script letters to denote matrices of dimension $2N \times 2N$.

The matrix \mathcal{A} has the form

$$\mathcal{A} = \begin{pmatrix} F & 0 \\ 0 & F^* \end{pmatrix} \quad (5.20)$$

and F is the usual $N \times N$ discrete Fourier transformation matrix, whose q th row is:

$$F(q, :) = \frac{1}{\sqrt{N}} [\exp(ik_q x_{-M}), \dots, \exp(ik_q x_M)], \quad (5.21)$$

from which Eqs. (5.14) and (5.15) are easily recovered.

It is straightforward to see that the operators $\hat{a}(k_q)$ and $\hat{\psi}(x_n)$ obey similar commutation relations Eqs. (5.8) and (5.9). In this chapter we shall exclusively deal with transformations to new sets of operators that conserve this property.

5.4.3 Diagonalization of the Bogoliubov Hamiltonian

Using the notation developed in the preceding section, we can write the Bogoliubov Hamiltonian Eq. (5.11) in a compact form:

$$\hat{H} = \mathbf{a}^\dagger \mathcal{H} \mathbf{a}. \quad (5.22)$$

As shown in, e.g., [70], this Hamiltonian can be diagonalized to the matrix \mathcal{E} by transforming to new boson operators:

$$\mathbf{b} = \mathcal{B} \mathbf{a}, \quad (5.23)$$

$$\begin{aligned} \hat{H} &= \mathbf{a}^\dagger \mathcal{H} \mathbf{a} \\ &= \mathbf{a}^\dagger \mathcal{B}^\dagger (\mathcal{B}^\dagger)^{-1} \mathcal{H} \mathcal{B}^{-1} \mathcal{B} \mathbf{a} \\ &= \mathbf{b}^\dagger (\mathcal{B}^\dagger)^{-1} \mathcal{H} \mathcal{B}^{-1} \mathbf{b} \\ &= \mathbf{b}^\dagger \mathcal{E} \mathbf{b}, \end{aligned} \quad (5.24)$$

$$\mathcal{E} = (\mathcal{B}^\dagger)^{-1} \mathcal{H} \mathcal{B}^{-1}. \quad (5.25)$$

The matrix \mathcal{H} only has elements different from zero in the two diagonals $\mathcal{H}(k_q, k_q)$ and $\mathcal{H}(k_q, k_{-q})$, giving the matrix an "X structure". In addition,

all elements are real. Therefore the matrix \mathcal{B}^{-1} that diagonalizes \mathcal{H} also only has elements different from zero with these indices and can be chosen real. The upper-left to lower-right diagonal elements are denoted $u(k_q)$, while the upper-right to lower-left diagonal elements are denoted $v(k_q)$. The elements can be found in, e.g., [71]:

$$u(k_q) = \begin{cases} 1 & \text{for } q = 0, \\ \sqrt{\frac{q^2/4 + \gamma/2}{\epsilon(q)/E_0} + \frac{1}{2}} & \text{for } q \neq 0, \end{cases}$$

$$v(k_q) = \begin{cases} 0 & \text{for } q = 0, \\ -\sqrt{\frac{q^2/4 + \gamma/2}{\epsilon(q)/E_0} - \frac{1}{2}} & \text{for } q \neq 0. \end{cases}$$

The diagonalized form \mathcal{E} has elements $\epsilon(q)$:

$$\epsilon(q) = E_0 \sqrt{\gamma q^2 + q^4/4}, \quad (5.26)$$

where $E_0 = \frac{(2\pi\hbar)^2}{mL^2}$, $\gamma = \frac{gN_{tot}}{E_0}$, and gN_{tot} has the same meaning as in Eq. (5.11).

By diagonalizing the Hamiltonian we have found a basis of noninteracting modes with a simple time evolution:

$$\hat{b}_q(t) = \hat{b}_q(0) \exp[-i\epsilon(q)t/\hbar].$$

By defining the para-identity matrix $\hat{\mathcal{J}}$, which will play an important role in the next section,

$$\hat{\mathcal{J}} = \text{diag}(\underbrace{1, \dots, 1}_N, \underbrace{-1, \dots, -1}_N), \quad (5.27)$$

we can write the vector of operators \mathbf{b} at time t as

$$\mathbf{b}(t) = \exp(-i\hat{\mathcal{J}}\mathcal{E}t/\hbar)\mathbf{b}(0) = \mathcal{U}(t)\mathbf{b}(0). \quad (5.28)$$

The changes of basis can be summarized,

$$\begin{aligned} \boldsymbol{\psi}(t) &= \mathcal{A}^{-1}\mathbf{a}(t) \\ &= \mathcal{A}^{-1}\mathcal{B}^{-1}\mathbf{b}(t) \\ &= \mathcal{A}^{-1}\mathcal{B}^{-1}\mathcal{U}(t)\mathbf{b}(0), \end{aligned} \quad (5.29)$$

whereby we can find the time evolution of the $\hat{\psi}(x_n, t)$ and $\hat{\psi}^\dagger(x_n, t)$:

$$\boldsymbol{\psi}(t) = \mathcal{A}^{-1}\mathcal{B}^{-1}\mathcal{U}(t)\mathcal{B}\mathcal{A}\boldsymbol{\psi}(0). \quad (5.30)$$

5.4.4 General para-unitary diagonalization

All the vectors of operators Eq. (5.16), Eq. (5.18), and Eq. (5.23) are examples of a vector of general boson ladder operators,

$$\boldsymbol{\alpha} = \begin{pmatrix} \hat{\alpha}_{-M} \\ \vdots \\ \hat{\alpha}_M \\ \hat{\alpha}_{-M}^\dagger \\ \vdots \\ \hat{\alpha}_M^\dagger \end{pmatrix}, \quad (5.31)$$

fulfilling the commutation relations

$$[\hat{\alpha}_q, \hat{\alpha}_{q'}^\dagger] = \delta_{q,q'}, \quad (5.32)$$

$$[\hat{\alpha}_q, \hat{\alpha}_{q'}] = 0. \quad (5.33)$$

Both the Fourier transformation Eq. (5.19) and the Bogoliubov transformation Eq. (5.23) are examples of changes of basis, known as para-unitary transformations, which conserve the boson commutation relations between the operators. All the transformations to new sets of operators in this chapter conserve this property. In our present treatment, there are two main reasons for making these transformations. First, the measurements we will consider are in coordinate space and wave number space at different times, but the operators corresponding to these measurements have complicated time evolutions. Working instead in the \mathbf{b} basis Eq. (5.28) the time evolution is simple, and the exponent in Eq. (5.4) can be easily calculated. Second, to perform the traces in Eq. (5.6), it is convenient to shift to a basis where the density operator is diagonal, and this can be done by a para-unitary transformation. We recall that there are $2N$ ladder operators, regardless of basis (e.g. the set $\{\hat{\psi}(x_n)\} \cup \{\hat{\psi}^\dagger(x_n)\}$), which will make the transformation matrices $2N \times 2N$.

The commutation relations demand that in a transformation from one set of boson operators to another,

$$\boldsymbol{\beta} = \mathcal{T} \boldsymbol{\alpha}, \quad (5.34)$$

the $2N \times 2N$ matrix \mathcal{T} must be para-unitary - i.e. satisfy the condition⁴

$$\hat{\mathcal{J}} = \mathcal{T} \hat{\mathcal{J}} \mathcal{T}^\dagger, \quad (5.35)$$

⁴To follow [70] we use the, in matrix algebra unusual, prefix "para-" instead of "pseudo-".

with the diagonal matrix $\hat{\mathcal{S}}$ defined in Eq. (5.27)⁵. From the definition it is seen that the product of two para-unitary matrices is again para-unitary.

The matrices we will diagonalize in this chapter will all be Hermitian, positive definite, and have the structure⁶

$$\mathcal{X} = \begin{pmatrix} P & Q \\ Q^* & P^* \end{pmatrix}. \quad (5.36)$$

Let \hat{X} be a Hermitian operator in the α basis with coefficient matrix \mathcal{X} . Such a Hermitian matrix \mathcal{X} can be diagonalized by the para-unitary matrix \mathcal{T} to a new set of operators $\{\beta_n\}$ and $\{\beta_n^\dagger\}$:

$$\begin{aligned} \hat{X} &= \alpha^\dagger \mathcal{X} \alpha & (5.37) \\ &= \alpha^\dagger \mathcal{T}^\dagger (\mathcal{T}^\dagger)^{-1} \mathcal{X} \mathcal{T}^{-1} \mathcal{T} \alpha \\ &= \beta^\dagger (\mathcal{T}^\dagger)^{-1} \mathcal{X} \mathcal{T}^{-1} \beta \\ &= \beta^\dagger \mathcal{L} \beta. & (5.38) \end{aligned}$$

Because \mathcal{X} is positive definite the para-eigenvalues $\mathcal{L}_{i,i}$ will also be positive by Sylvester's law of inertia⁷. The matrix \mathcal{T} can be chosen to have the structure

$$\mathcal{T} = \begin{pmatrix} U & V^* \\ V & U^* \end{pmatrix}, \quad (5.39)$$

giving \mathcal{L} the form

$$\mathcal{L} = \text{diag}(\mathcal{L}_{1,1}, \mathcal{L}_{2,2}, \dots, \mathcal{L}_{N,N}, \mathcal{L}_{1,1}, \dots, \mathcal{L}_{N,N}). \quad (5.40)$$

This general procedure will become useful in the following section, where we will need to evaluate expectation values of the observed densities within a quantum state of the form Eq. (5.4), facilitated by a para-unitary diagonalization of the exponent $\sum_\nu \lambda_\nu \hat{G}_\nu$.

⁵Had we been treating fermion- instead of boson operators, the matrix \mathcal{T} would have been unitary.

⁶A bilinear, Hermitian operator can always be brought to this form by adding a scalar constant which is determined by the diagonal of the matrix.

⁷Sylvester's law of inertia states that any conjunctivity diagonalization $\mathcal{T}^\dagger \mathcal{X} \mathcal{T} = \mathcal{L}$ of the Hermitian matrix \mathcal{X} by the non-singular matrix \mathcal{T} gives the same number of positive, negative and zero diagonal values in the diagonal matrix \mathcal{L} . Therefore, the positive definiteness of a matrix is conserved under conjunctivity transformations.

5.5 Using MAXENT with the Bogoliubov approximation

Now we are ready to use the MAXENT formalism on the condensate in the Bogoliubov approximation. As the set of observables $\{\hat{G}_\nu\}$ we use measurements of particle numbers at coordinate space points at different times t , and of the occupation of wave number modes at times t' . The times t can, but need not, be equal to the times t'

$$\begin{aligned} \{\hat{G}_\nu\} = & \{\hat{\psi}^\dagger(x_n, t)\hat{\psi}(x_n, t) + \hat{\psi}(x_n, t)\hat{\psi}^\dagger(x_n, t)\} \cup \\ & \{\hat{a}^\dagger(k_q, t')\hat{a}(k_q, t') + \hat{a}(k_q, t')\hat{a}^\dagger(k_q, t')\}. \end{aligned} \quad (5.41)$$

Specifically, we shall in the numerical examples of section 5.6 use measurements of particle numbers at all spatial points n for a few different points of time, and some or all of the wave number, k_q , occupation numbers at a single point of time. For now, though, our general formulation does not require a closer specification of the used measurements: We are merely showing how to include the measurements conveniently in the MAXENT density operator, Eq. (5.4).

On a practical note, the reason for using the symmetrical form of the observables in Eq. (5.41) is that it leads to the favorable structure Eq. (5.36) of the matrix in the exponent of Eq. (5.4).

The task is now to put these observables into the MAXENT density operator Eq. (5.4) and perform traces like Eqs. (5.1). To do this we will use the same method as in section 5.3 to diagonalize the matrix in the exponent into a set of new, noninteracting quasi-particles.

Let \mathcal{W}_n be the $2N \times 2N$ matrix with the elements

$$\mathcal{W}_n(r, s) = \begin{cases} 1 & \text{for } r = s = n + M + 1, \\ 1 & \text{for } r = s = n + N + M + 1, \\ 0 & \text{otherwise,} \end{cases} \quad (5.42)$$

so that (using Eq. (5.29) for the first part):

$$\begin{aligned} \hat{\psi}^\dagger(x_n, t)\hat{\psi}(x_n, t) + \hat{\psi}(x_n, t)\hat{\psi}^\dagger(x_n, t) &= \boldsymbol{\psi}^\dagger(t)\mathcal{W}_n\boldsymbol{\psi}(t) \\ &= \mathbf{b}^\dagger(0)\mathcal{U}^\dagger(t)(\mathcal{B}^{-1})^\dagger(\mathcal{A}^{-1})^\dagger\mathcal{W}_n\mathcal{A}^{-1}\mathcal{B}^{-1}\mathcal{U}(t)\mathbf{b}(0), \end{aligned} \quad (5.43)$$

and

$$\begin{aligned} \hat{a}^\dagger(k_q, t')\hat{a}(k_q, t') + \hat{a}(k_q, t')\hat{a}^\dagger(k_q, t') &= \mathbf{a}^\dagger(t')\mathcal{W}_q\mathbf{a}(t') \\ &= \mathbf{b}^\dagger(0)\mathcal{U}^\dagger(t')(\mathcal{B}^{-1})^\dagger\mathcal{W}_q\mathcal{B}^{-1}\mathcal{U}(t')\mathbf{b}(0). \end{aligned} \quad (5.44)$$

The operator $\sum_\nu \lambda_\nu \hat{G}_\nu$, with \hat{G}_ν being operators of the form Eq. (5.43) and Eq. (5.44), is hence expressed in terms of the Bogoliubov eigenmode operators, and we can write the MAXENT density operator Eq. (5.4) in a compact form:

$$\hat{\rho}_{ME} = \frac{1}{Z} \exp(-\mathbf{b}^\dagger(0) \mathcal{P} \mathbf{b}(0)), \quad (5.45)$$

where

$$\begin{aligned} \mathcal{P} &= \sum_t \sum_{\{n(t)\}} \lambda(n, t) \mathcal{U}^\dagger(t) (\mathcal{B}^{-1})^\dagger (\mathcal{A}^{-1})^\dagger \mathcal{W}_n \mathcal{A}^{-1} \mathcal{B}^{-1} \mathcal{U}(t) \\ &+ \sum_{t'} \sum_{\{q(t')\}} \lambda(q, t') \mathcal{U}^\dagger(t') (\mathcal{B}^{-1})^\dagger \mathcal{W}_q \mathcal{B}^{-1} \mathcal{U}(t'). \end{aligned} \quad (5.46)$$

In Eq. (5.46), the set $\{n(t)\}$ are the spatial measurements made at time t and the set $\{q(t)\}$ are the wave number measurements made at time t' .

Since the structures of $\mathcal{U}(t)$, \mathcal{A} , and \mathcal{B} are all like that of Eq. (5.39) and the structure of \mathcal{W}_q is like that of Eq. (5.36), so is the structure of \mathcal{P} . We can therefore diagonalize it to a diagonal matrix \mathcal{L} by a para-unitary change of basis to new Boson operators $\mathbf{c} = \mathcal{C} \mathbf{b}(0)$:

$$\mathbf{b}^\dagger(0) \mathcal{P} \mathbf{b}(0) = \mathbf{c}^\dagger \mathcal{L} \mathbf{c} \quad (5.47)$$

$$= \sum_{j=1}^N \mathcal{L}_{j,j} (\hat{c}_j^\dagger \hat{c}_j + \hat{c}_j \hat{c}_j^\dagger). \quad (5.48)$$

Remembering that the $\mathcal{L}_{j,j}$ are all positive, the partition function Eq. (5.5) becomes

$$\begin{aligned} Z &= \text{Tr} \left\{ \exp \left[- \sum_{j=1}^N \mathcal{L}_{j,j} (\hat{c}_j^\dagger \hat{c}_j + \hat{c}_j \hat{c}_j^\dagger) \right] \right\} \\ &= \prod_{j=1}^N \left[\frac{1}{\exp(\mathcal{L}_{j,j}) - \exp(-\mathcal{L}_{j,j})} \right], \end{aligned} \quad (5.49)$$

and we can readily determine the corresponding set of expectation values:

$$\begin{aligned}
\langle \hat{c}_m^\dagger \hat{c}_n \rangle &= \frac{1}{Z} \text{Tr} \left\{ \hat{c}_m^\dagger \hat{c}_n \exp \left[- \sum_{j=1}^N \mathcal{L}_{j,j} \left(\hat{c}_j^\dagger \hat{c}_j + \hat{c}_j \hat{c}_j^\dagger \right) \right] \right\} \\
&= -\frac{1}{2} \left(1 + \frac{\partial \ln Z}{\partial \mathcal{L}_{n,n}} \right) \delta_{m,n} \\
&= \frac{1}{\exp(2\mathcal{L}_{n,n}) - 1} \delta_{m,n}, \tag{5.50}
\end{aligned}$$

$$\langle \hat{c}_m \hat{c}_n \rangle = \langle \hat{c}_m^\dagger \hat{c}_n^\dagger \rangle = 0. \tag{5.51}$$

Knowing these expectation values, it is easy to find the expectation values of all the second moments in any basis – for example,

$$\begin{aligned}
\langle \boldsymbol{\psi}(t) \boldsymbol{\psi}^\dagger(t) \rangle &= \begin{pmatrix} \langle \hat{\psi}(x_{-M}) \hat{\psi}^\dagger(x_{-M}) \rangle & \cdots & \langle \hat{\psi}(x_{-M}) \hat{\psi}(x_{-M}) \rangle & \cdots \\ \vdots & \ddots & \vdots & \ddots \\ \langle \hat{\psi}^\dagger(x_{-M}) \hat{\psi}^\dagger(x_{-M}) \rangle & \cdots & \langle \hat{\psi}^\dagger(x_{-M}) \hat{\psi}(x_{-M}) \rangle & \cdots \\ \vdots & \ddots & \vdots & \ddots \end{pmatrix} \\
&= \mathcal{A}^{-1} \langle \mathbf{a}(t) \mathbf{a}^\dagger(t) \rangle (\mathcal{A}^{-1})^\dagger \\
&= [\mathcal{C} \mathcal{U}^{-1}(t) \mathcal{B} \mathcal{A}]^{-1} \langle \mathbf{c} \mathbf{c}^\dagger \rangle \left\{ [\mathcal{C} \mathcal{U}^{-1}(t) \mathcal{B} \mathcal{A}]^{-1} \right\}^\dagger. \tag{5.52}
\end{aligned}$$

In passing, it is noted that the lower right $N \times N$ submatrix of the matrix $\langle \boldsymbol{\psi}(t) \boldsymbol{\psi}^\dagger(t) \rangle$ is the one-body density matrix.

As a final point we give a comment on the requirement of the positive definiteness of \mathcal{P} . It is clearly seen here that we must require the diagonal elements of \mathcal{L} to be strictly positive for the geometrical series summed to find Eq. (5.49) to be convergent. Therefore, by Sylvester's law of inertia, \mathcal{P} must also be positive definite. In addition, for this condition to be fulfilled, the number of observables in $\{\hat{G}_\nu\}$ must be at least as large as N . The reason for this is that in Eq. (5.46) the matrices \mathcal{W}_n have dimensionality 2 in the $2N$ space, the dimensionality of course being conserved under the para-unitary changes of basis. So to span the $2N$ space, at least N observables of dimensionality two must be included. In the present chapter, however, we will have many more observations than N , and linear dependences between them are highly unlikely to reduce the dimensionality below $2N$.

5.6 Tomography on three quantum states

To examine the reliability of the MAXENT technique, regarding reconstruction of the correct second moments of the ladder operators, we study three very different types of condensate quantum states with nearly the same density distribution at $t = 0$: namely, a Gaussian perturbation on top of a flat condensate. Apart from serving for testing the method's reliability, these examples are of practical interest and their implementations are discussed in subsection 5.7.1 below.

5.6.1 Initial excited states

Even though the three states we will study have nearly the same initial spatial density distribution, they will be created with different initial coherences. As the time evolution, Eq. (5.30), remembers the initial coherence, their spatial distributions will differ at later times, allowing the MAXENT procedure to tell them apart.

Recalling that we are not attempting to reconstruct the full many-particle quantum state, but only the second moments of the ladder operators, let us look at their value at time t , given their value at $t = 0$:

$$\langle \psi(t)\psi^\dagger(t) \rangle = \mathcal{A}^{-1}\mathcal{B}^{-1}\mathcal{U}(t)\mathcal{B}\mathcal{A} \langle \psi(0)\psi^\dagger(0) \rangle [\mathcal{A}^{-1}\mathcal{B}^{-1}\mathcal{U}(t)\mathcal{B}\mathcal{A}]^\dagger. \quad (5.53)$$

Hence, due to the simple dynamics given by Eq. (5.11), the second moments at all times are uniquely specified by their values at $t = 0$. We will use these $t = 0$ values from the three states below for two purposes. The first is to generate the measurement data, which, being second moments themselves, are all formed by appropriate linear combinations of the spatial $t = 0$ moments in Eq. (5.53). The second purpose is that the second moments at $t = 0$ are precisely what we will reconstruct by the procedure described in section 5.3.

1. **Coherent state.** This is a pure state of all the particles, representable as a product state with all the particles in the same one-particle state. The assumption of this particular type of product state is exactly what is used to derive the Gross-Pitaevskii equation:

$$-i\hbar \frac{\partial \psi(x, t)}{\partial t} = \left(-\frac{\hbar^2}{2m} \frac{\partial^2}{\partial x^2} + gN_{tot} |\psi(x, t)|^2 \right) \psi(x, t). \quad (5.54)$$

We choose the one-particle state to be a constant with a Gaussian perturbation in coordinate space:

$$|State 1\rangle = (\hat{\psi}_g^\dagger)^{N_{part}} |0\rangle, \quad \text{where} \quad (5.55)$$

$$\hat{\psi}_g^\dagger = \sum_{x_n} \phi_{gauss}(x_n) \hat{\psi}^\dagger(x_n), \quad (5.56)$$

and ϕ_{gauss} is a constant plus a Gaussian with standard deviation σ , centered at the origin: $\phi_{gauss} \propto \left\{ 1 + \eta \exp \left[-\frac{1}{2} \left(\frac{x_n}{\sigma} \right)^2 \right] \right\}$. N_{part} is the total number of particles. We can envision this state formed in a uniform system with a negative potential dip, having *State 1* as its ground state. The spatial evolution of the state after abruptly turning off the potential at $t = 0$ is what is usually handled with the Gross-Pitaevskii equation.

2. **Thermal perturbation.** This state is a flat condensate with a thermal Gaussian perturbation superposed hereupon. The Gaussian perturbation is treated as originating from a thermal boson gas in a harmonic trap, and we have assumed no initial correlations between the perturbation and the original flat condensate. Therefore the second moments for this state in coordinate space are simply the sum of the second moments of the thermal Gaussian and of the flat condensate.
3. **Squeezed condensate.** We get this state by applying an operator, similar to the squeezing operator known from squeezing of light, to a condensate with all N_{part} particles in the condensate mode:

$$|State 3\rangle = \exp \left[z^* (\hat{\psi}_g)^2 - z (\hat{\psi}_g^\dagger)^2 \right] (\hat{b}_0^\dagger)^{N_{part}} |0\rangle. \quad (5.57)$$

The most important difference between the two preceding states and this one is the magnitude of the anomalous second moments at $t = 0$. In *State 1* and *State 2* the anomalous second moments are all zero, while they in this state are comparable in magnitude with the normal second moments.

5.6.2 Results of tomography

We present here the results of using the MAXENT technique on the three states presented in section 5.6.1. The main points of interest are not just whether a reliable reconstruction is attained in each case, but also the amount of data

needed for this. In all the results shown in this section we have used density distributions in coordinate space at four different times and the number of particles in the zero-wave-number mode $\langle \hat{a}_0^\dagger \hat{a}_0 \rangle$. In *State 2* we have furthermore used the momentum distribution at $t = 0$, and in *State 3* we have additionally included an observation of $\langle \hat{a}_0 \hat{a}_0 + \hat{a}_0^\dagger \hat{a}_0^\dagger \rangle$.

We have used 10^5 particles in the flat part of the condensate at $t = 0$ and set $gN_{tot} = 0.1$. The population in the zero-wave-number modes is 99.5% in *State 1* and 3 and 96% in *State 2*. For the calculations we have used a grid of $N = 25$ discrete points.

In Fig. 5.1 we show the time evolution of the density distributions in coordinate space of the three different states declared in section 5.6.1. We have intentionally chosen the initial distributions to be very similar. The perturbations give rise to density variations of a magnitude readily detected [72].

Let us proceed to examine the true second moments of the ladder operators for the three states and those reconstructed using the MAXENT procedure. We will study these using surface plots of the absolute value of the second moments and of the absolute value of the difference between the true values of these moments and those predicted by MAXENT for the state at $t = 0$. In this way, errors in both magnitude and phase of the matrix elements will be visible.

For *State 1*, where we will see that the reconstruction is precise and only the normal second moments are nonzero at $t = 0$, we shall also display the phase-space Wigner function corresponding to these normal second moments. Apart from normalization, the normal second moments can be interpreted as the density matrix for any single atom in the system, and the phase-space Wigner function $W(x_n, k_q)$ is a convenient representation of this. The cited works [5], [8], [30] all show the Wigner function of the particle states, and much interest has been devoted to the fact that measurements of exclusively positive marginal distributions may be used to identify Wigner functions with domains of negative values [6], [73]. The connection between the Wigner function and the normal second moments is given in appendix A.1.

State 1

Treating first *State 1*, Fig. 5.2 presents the absolute values of the normal second moments as found from section 5.6.1. The reconstructed second moments are identical to the input values within round-off errors, which amounts to an accumulated error of 10^{-4} on each matrix element, including phase. The same is true for the anomalous second moments, all having the true value zero at $t = 0$.

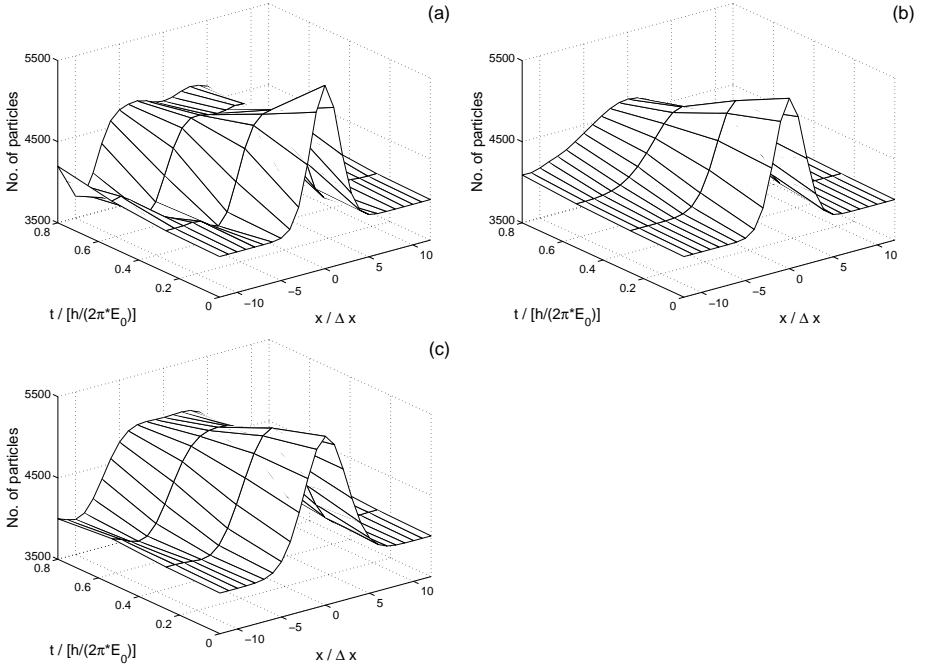


Figure 5.1: Density distributions in coordinate space at four different points of time for (a) *State 1*, (b) *State 2*, and (c) *State 3*. The data shown are those used in the reconstruction together with the zero-wave-number population $\langle \hat{a}_0^\dagger \hat{a}_0 \rangle$. For *State 2* and *State 3*, the momentum distributions at $t = 0$ were also used, and one anomalous moment for *State 3*.

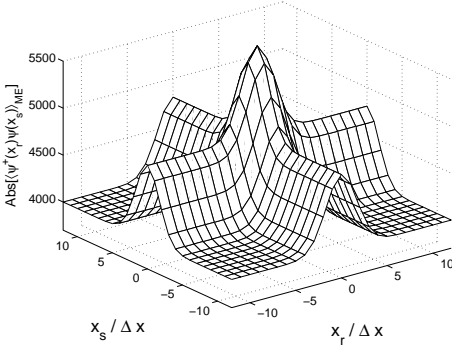


Figure 5.2: Absolute values of the reconstructed normal second moments $\langle \hat{\psi}^\dagger(x_r)\hat{\psi}(x_s) \rangle$ of *State 1*. The anomalous second moments are all zero (not shown). Both normal and anomalous moments are reconstructed to within machine precision, including complex phase, giving accumulated errors of magnitude 10^{-4} on each element. The data used for the reconstruction are four spatial density distributions and $\langle \hat{a}_0^\dagger \hat{a}_0 \rangle$. The true second moments are not shown, as they are practically identical to the reconstructed ones.

As a consequence, the Wigner function for *State 1* is also perfectly reconstructed and is presented in Fig. 5.3.

State 2

For *State 2* the true and reconstructed normal second moments are shown in Fig. 5.4. Also shown in this figure is the absolute value of the difference between the true and reconstructed normal second moments. The errors are many orders of magnitude larger than for *State 1*.

In Fig. 5.5 we display the absolute values of the reconstructed anomalous second moments, which all have the true value zero at $t = 0$.

State 3

The absolute value of the true and reconstructed second moments are shown in Fig. 5.6 together with the absolute value of the difference between these.

In *State 1* and *State 2*, the true value of the anomalous second moments have all been equal to zero at $t = 0$. In contrast, for the squeezed state, the absolute values of these elements are comparable with the normal second moments. The

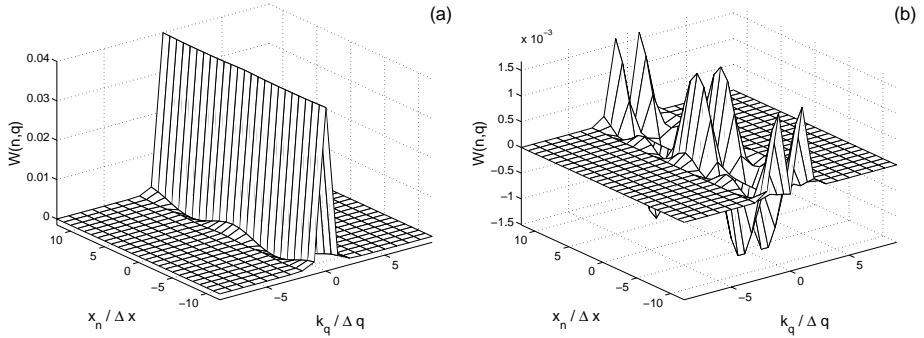


Figure 5.3: The figure (a) shows the Wigner function for the normal second moments of *State 1* - i.e., the one-body density matrix apart from normalization. In figure (b) the elements $W(n,0)$ are set equal to zero to more clearly reveal the finer structures and the negativities of the Wigner function.

absolute values of the true and reconstructed second anomalous moments are displayed in Fig. 5.7.

5.7 Discussion

Initially, a short comment on the choice of observables might be in order. If there were no constant background condensate, the momentum distribution could in principle be found from the spatial distributions at late times. Having to deal with this background, however, one has to include the additional observables in the MAXENT density operator to exclude the possibility of the flat part of the condensate being an almost even distribution of particles with all allowed types of wave numbers whirling left and right, which would otherwise be preferred by the MAXENT formalism. Recalling section 2.4.1, a similar situation led to the impossibility of finding diagonal elements of the density matrix for a free particle with periodic boundary conditions. Measurements of wave number mode populations would precisely have given these diagonal elements for the free particle, so we hoped that inclusion of such measurements in the MAXENT operator would improve reliability in the present setting too.

Indeed we find for *State 1* a very good reconstruction, the errors being of the same magnitude as computer round-off errors, from using just measurements of the distribution in coordinate space at three times and the number of particles in

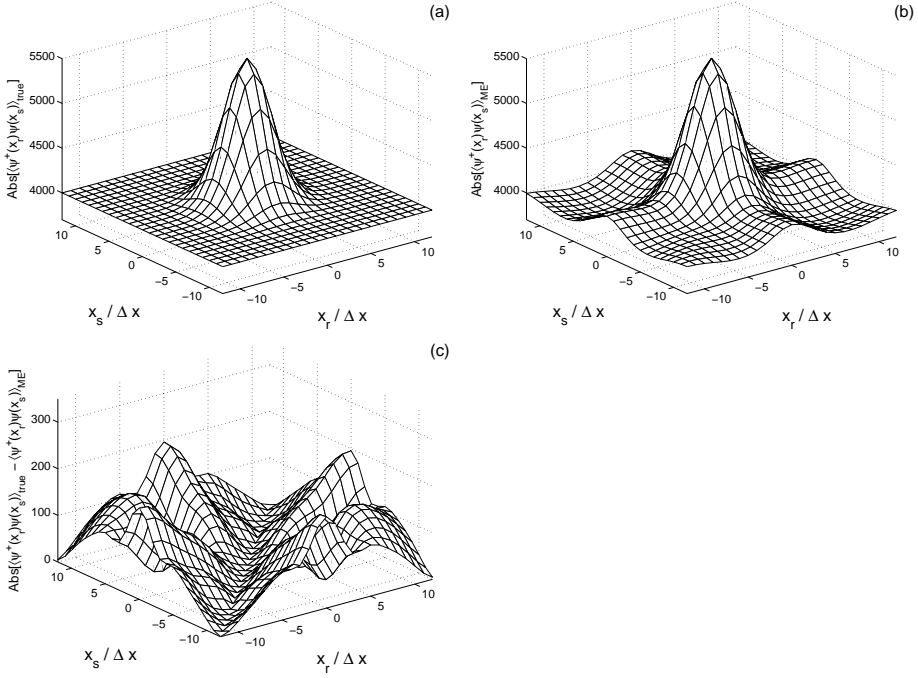


Figure 5.4: The first two graphs show the absolute values of (a) the true and (b) the reconstructed normal second moments $\langle \hat{\psi}^\dagger(x_r) \hat{\psi}(x_s) \rangle$ for *State 2*. The errors above the flat condensate are up to about 10% of the peak value. The bottom graph (c) shows the absolute value of the difference between true and reconstructed normal second moments. The data used in the reconstruction are four spatial density distributions and one momentum distribution.

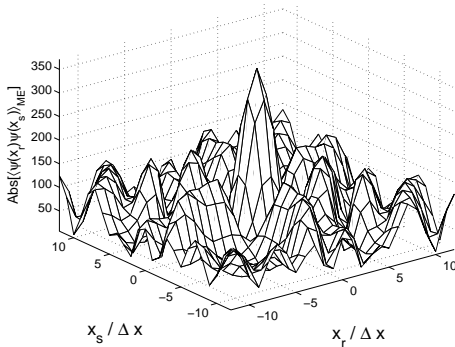


Figure 5.5: Absolute values of the reconstructed anomalous second moments $\langle \hat{\psi}(x_r)\hat{\psi}(x_s) \rangle$ for *State 2* at $t = 0$. The true values are all zero at $t = 0$. The magnitude of the errors is similar to the errors of the normal second moments for this state.

the zero-wave-number mode $\langle \hat{a}^\dagger(0)\hat{a}(0) \rangle$. In addition to *State 1* in section 5.6.2, we also tried to reconstruct states of this type with more complicated initial distributions, but still describable by a simple Gross-Pitaevskii wave function. These included perturbations with two peaks and perturbations with one peak and one hole in the flat background. In all cases the reconstruction had the same precision as *State 1*, indicating that the second moments, including the one-body density matrix, of states describable by a simple Gross-Pitaevskii equation can be completely reconstructed.

For *State 2*, we found that a wave number distribution also had to be included as observable to get a somewhat reliable reconstruction of the second moments. In the absence of such a measurement, the MAXENT formalism would fail through predicting a very large thermal-like population of high wave number modes. It is reasonable that it is difficult to tell apart whether the moving particles belong to the perturbation on top of a flat condensate or to some collective motion of the whole - for example, similar to *State 1*. Including the momentum distribution remedied this problem somewhat, but errors still persist (see Fig. 5.4). Subtracting the flat background, these errors are of magnitudes about 10% of the perturbation peak value.

For *State 3* with large numerical values of the anomalous second moments, we find a reasonable reconstruction at $t = 0$ of the normal second moments, but reconstruction of the anomalous second moments completely fails, unless

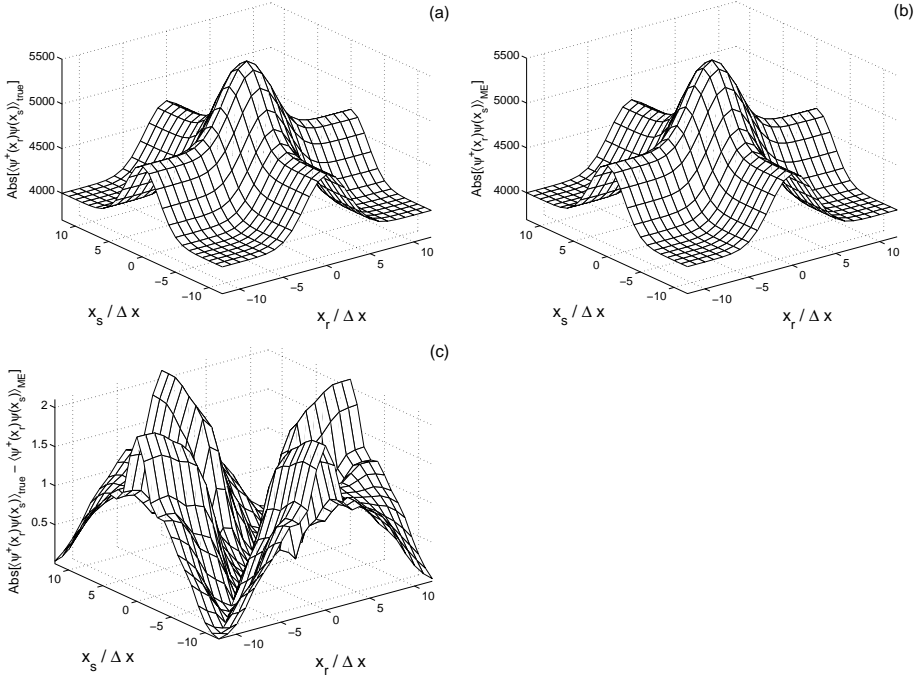


Figure 5.6: The first two graphs show the absolute values of (a) the true and (b) the reconstructed normal second moments $\langle \hat{\psi}^\dagger(x_r) \hat{\psi}(x_s) \rangle$ of *State 3*. The lowest graph (c) is the absolute value of the difference between the true and reconstructed second moments. The data used in the reconstruction are four spatial density distributions, one momentum distribution, and one anomalous moment $\langle \hat{a}_0 \hat{a}_0 + \hat{a}_0^\dagger \hat{a}_0^\dagger \rangle$.

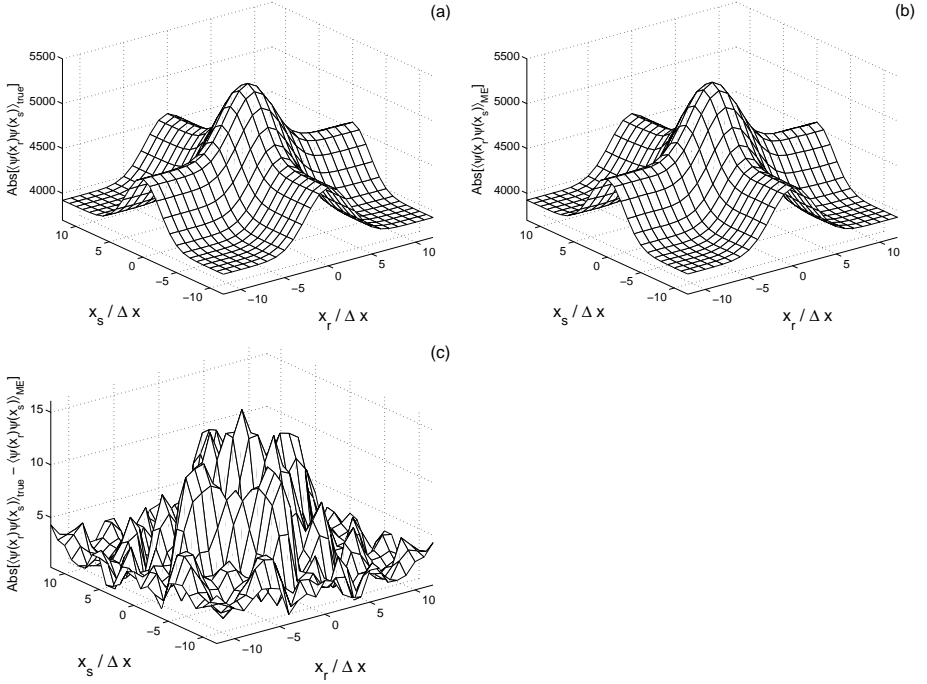


Figure 5.7: The first two graphs show the absolute values of (a) the true and (b) the reconstructed anomalous second moments $\langle \hat{\psi}(x_r) \hat{\psi}(x_s) \rangle$ of *State 3*. The lowest graph (c) is the absolute value of the difference between the true and reconstructed second moments. The data used in the reconstruction are four spatial density distributions, one momentum distribution, and one anomalous moment $\langle \hat{a}_0 \hat{a}_0 + \hat{a}_0^\dagger \hat{a}_0^\dagger \rangle$.

we additionally include the observable $\hat{a}_0\hat{a}_0 + \hat{a}_0^\dagger\hat{a}_0^\dagger$ in the MAXENT density operator, as we did in section 5.6.2.

It is also worthy of notice that there was almost no improvement in the reconstruction from including additional position and momentum distributions for more points of time, and that using also the observable $\langle\hat{a}_0\hat{a}_0 + \hat{a}_0^\dagger\hat{a}_0^\dagger\rangle$ for *State 1* and *State 2* did not change the precision of the reconstructed second moments.

As for states significantly different from the ones treated here, distributions in coordinate space at more points of time may be required for a reliable reconstruction. Since enlarging the number of measured distributions in space is rarely a problem, we suggest for specific applications to gradually include more distributions until the results have stabilized. The calculation time is quite manageable, the shown examples all taking well under an hour on an ordinary PC.

5.7.1 Practical considerations

Throughout the chapter we have assumed that experimental data provide reliable estimates of the mean values $\langle\hat{G}_\nu\rangle$ needed for state reconstruction. It is a strength of the MAXENT procedure that it minimizes the error between observed and computed mean values, and hence inaccurate data do not prevent us from obtaining a candidate density operator of the system.

Clearly, matching to erroneous data makes the reconstruction more or less invalid, and it is hence important that the measurement errors are limited. One concern is the difficulty in preparing the system many times in exactly the same quantum state, as usually required in QSR. Condensates are routinely produced in the laboratory, but the repetition rate of the trapping and cooling cycles is low, and the total number of atoms in the condensate fluctuates between experimental runs. To circumvent this problem, one may use a 2D optical lattice, which converts a 3D condensed cloud into a large array of 1D elongated condensates with well-controlled relative populations [74]. Or one may perform the experiment on one single condensate, relying on the macroscopic population of the system to be large enough to allow good counting statistics for all the observables - e.g., the spatial density.

Since we are measuring non-commuting observables on the same system, we must have adequately many particles, so that none of these measurements cause significant disturbances of the others. Nondestructive measurements at different times of the densities in coordinate space of a single condensate have already been demonstrated [75], and recent papers deal with the sensitivity of some of

these methods [76], [77]. The measurement of the number of particles in the zero-wave-number mode has traditionally been observed by absorption imaging of the expanded cloud released from the trap, but it may also be performed by Bragg interferometry or by interference with another reference condensate. Imprecision in this measurement will lead to errors of the qualitative form of a high-temperature-like component of the condensate, as described in the beginning of this section.

Finally, to reconstruct a squeezed condensate state, we assume knowledge of the anomalous moment of the zero-wave-number mode. This quantity can be measured by interfering the condensate with a macroscopic reference condensate on an atom beam splitter [78]. The number fluctuations between the two split condensate parts contain a component which is precisely the anomalous moment, $\langle \hat{a}_0 \hat{a}_0 + \hat{a}_0^\dagger \hat{a}_0^\dagger \rangle$. Probing number fluctuations by atom counting requires many experiments, which could be done at the same time on the 2D array of condensates mentioned above, but one may also imagine that the probing of collisional losses from a single condensate can provide the number fluctuations directly and thereby the anomalous moment [79]. We recall that the interest in number-squeezed condensates is intimately connected with the possibility to make use of, and hence detect, the reduced number fluctuations in an experiment. As mentioned above, the reconstruction of the anomalous second moments at $t = 0$ is highly dependent on the measured value of $\langle \hat{a}_0 \hat{a}_0 + \hat{a}_0^\dagger \hat{a}_0^\dagger \rangle$, whereas the normal second moments are more robust to errors in this parameter. We would expect measurement errors in this parameter to transfer more or less directly to the magnitude of the anomalous second moments.

5.8 Conclusion

We have shown how to combine the MAXENT principle with the Bogoliubov approximation to give reliable estimates of the normal and anomalous second moments of the ladder operators – e.g. $\langle \hat{\psi}^\dagger(x) \hat{\psi}(x') \rangle$ and $\langle \hat{\psi}(x) \hat{\psi}(x') \rangle$ – in a perturbed condensate. For states describable by a simple Gross-Pitaevskii equation, we find near perfect reconstruction from data of density distributions at a few points of time and the number of particles in the zero-wave-number mode. For states with a larger amount of particles in nonzero-wave-number modes compared to the size of the perturbation in coordinate space, we find it necessary to include a momentum distribution in the measurement set to obtain a somewhat reliable reconstruction. Errors in this case are less than 10% of the perturbation peak value (peak above the constant condensate background). Thus, the

method makes it possible to distinguish between a thermal and a coherent perturbation of the condensate. Finally, we find that by measurement of a single observable related to squeezing, apart from measurements of momentum and coordinate space distributions, the method is able to correctly reconstruct all second moments of the ladder operators for squeezed states.

Chapter 6

Potential-laser effects in laser-assisted photo-ionization

6.1 Synopsis

This chapter deals with ionization of a molecule or an atom by an ultrashort extreme-ultra violet laser pulse in the presence of a moderately strong infrared laser field. We introduce and improve on the widespread strong field approximation by using eikonal states to approximate the true continuum functions. Hereby, we will find the photoelectron spectrum and also quantify the range of applicability of the commonly used separable Coulomb-Volkov functions. Using these results, we can resolve an ambiguity in existing approximate models of interference in high harmonic generation experiments, thereby laying the theoretical foundation for a key ingredient in Quantum State Reconstruction of molecular orbitals using high harmonic generation.

This chapter is based on the paper [80].

6.2 Introduction

Manipulating atoms and molecules with intense laser pulses has become ubiquitous in present day laboratories. These strong field interactions play a key role

in many areas, including plasma physics, micro machining and high harmonic generation (HHG) [81]. The two main features of laser pulses used for these purposes are their temporal shortness and their high intensities [82]. The duration spans from timescales of nuclear motion (hundreds of femtoseconds) and down to timescales of electronic motion (hundreds of attoseconds). The high intensities can produce electric fields comparable to or even surpassing those between electrons and nuclei in atoms. Due to the strength of these laser fields, the continuum can become strongly distorted. Thus, in the limit where the field is much stronger than the molecular- or atomic potential (M/A-potential), the continuum is describable by Volkov states, which we treat in section 6.3.1. Conversely, when the laser field and M/A-potential have comparable strength, there is no known closed analytical form of the wave function of electrons in the continuum. Nevertheless, precisely describing the behavior of ionized electrons in the simultaneous presence of strong fields and M/A-potentials is a key ingredient for a theoretical description of the interaction of intense pulses with matter.

Although not the main focus here, we shall often encounter HHG in this chapter and the next. Therefore, we briefly state the meaning of HHG: The process of forming harmonics of laser light through interaction between the incoming light pulse and molecules or atoms. By nonlinear processes, harmonics of the incoming light are formed, easily reaching the 100'th order and beyond. While the incoming pulse is of femtosecond duration, the outgoing HHG light usually consists of a train of attosecond pulses, but the formation of a single attosecond pulse is also possible [83]. The main features of the nonlinear process forming HHG can be understood as the strong incoming field transferring many low-energy photons to an electron in a molecule or atom, and the HHG light being formed through the recombination of this energetic electron with its parent ion into their original state [81]. This coherently emitted HHG photon has all the energy the molecule or atom received from the many incident low energy photons, and therefore has a frequency that is a harmonic of the incoming light - somewhat similar to the coherent emission process in chapter 4. This last recombination step will be of interest to us later.

Directly connected to this chapter, there has recently been increased interest in the behavior of ionized electrons near the parent ion for the purpose of understanding both interference effects in the HHG signal from diatomic molecules [84]-[87], and also the tomographic reconstruction of electronic orbitals from observed high harmonic radiation [35]. In the latter work, the experimental reconstruction of an orbital of N_2 depends critically on the spatial shape of the continuum wave functions, which were approximated to be plane waves. Explic-

itly, the measurements used for the reconstruction were HHG spectra, where the frequency of the emitted HHG light was assumed to stem from the recombination of a certain continuum component with the bound molecular orbital. A key point is thus how to translate a certain measured HHG frequency to the spatial shape of a continuum wave function. Considering the approximations made, the precision of the observed reconstruction is remarkable, especially when the many-electron nature of the nitrogen molecule is taken into account [88]. In this chapter, we aim to clarify why and when such continuum approximations are precise, and which correspondence to use between the frequency of HHG radiation and the spatial shape of a continuum wave function. For this purpose, we will study the time inverse of the process responsible for the high harmonic emission. To be exact, we will consider the time inverse of the recombination of an energetic electron from the continuum to a bound state [87].

Specifically, we focus on the ionization of an atom by an ultrashort laser pulse of extreme ultra violet (XUV) frequency in the presence of a moderately strong infrared (IR) laser field. The latter field is too weak to produce any significant ionization on its own. Our aim is to find an analytic expression for the photoelectron spectrum produced in such an experiment.

Previous investigations have in most cases used the strong field approximation (SFA), completely neglecting the M/A-potential in the propagation of the free electron; thorough introductions can be found in [89], [90]. In contrast, we will include the M/A-potential partially to all orders of perturbation by using the semiclassical Coulomb-Eikonal-Volkov (CEV) states, which have previously been shown to be well suited to calculate photoelectron spectra from laser assisted XUV ionization [91] as well as strong field ionization [92]. These numerical investigations show that including the M/A-potential in the propagation of the ionized electrons largely amounts to a small shift of the photoelectron peaks, approximately retaining their shape. In spite of their name, the potential in the CEV functions is not restricted to the Coulomb type, and we shall indeed postpone a specification of a certain potential to the very last.

A recent study [93] treats the same experimental situation as the one in the present chapter, but only for Coulomb potentials, and examines the applicability of a widespread approximation of separating the spatial continuum wave functions $\psi_C(\mathbf{r}, t)$ into two parts [94], [95]:

$$\psi_C(\mathbf{r}, t) \approx \psi_{\mathbf{k}}(\mathbf{r}) \phi(\mathbf{k}, t). \quad (6.1)$$

The first part $\psi_{\mathbf{k}}(\mathbf{r})$ is a spatial function which intricately depends on the final, field-free asymptotic momentum \mathbf{k} and the Coulomb potential, but only trivially on the field. The second is a time-dependent factor $\phi(\mathbf{k}, t)$, depending on the

aforementioned momentum and the field. The present chapter improves upon this approximation and will be seen to have a broader range of validity. With reference to separating the continuum in a M/A-potential-dependent coordinate part and a laser field-dependent time part, the treatment in this chapter can be seen as a coupling between these two parts, i.e. a measure of the non-separability of the continuum wave functions into this form.

It is important to note that our treatment below ignores polarization effects of the bound state by the IR laser field. Polarization effects can be taken into account at a later stage by using polarized bound states [91].

The chapter is organized as follows: In section 6.3.1 we review how to calculate the photoelectron spectrum in the SFA case. In section 6.3.2 we include the potential, through the CEV functions, as a perturbation to the SFA result. In section 6.4 we discuss the implications of the results.

6.3 Theory

We undertake calculating the photo-ionization spectrum in the experiment briefly described above. We imagine that an XUV pulse ionizes a molecule or an atom at the time t_X in the presence of an IR laser field. The ionized electron's state is then propagated to the time t_m , when its momentum spectrum is recorded. In the calculation, we shall make use of different approximate continuum states to propagate the ionized electron and we shall invoke the method of stationary phase. Throughout the chapter we shall use atomic units and work in n -dimensional space.

Proceeding with the calculation in detail, the time evolution is governed by the Hamiltonian:

$$\hat{H}(t) = \hat{H}_0 + \hat{V}(t) = \hat{H}_0 + \hat{H}_{IR}(t) + \hat{H}_X(t),$$

where \hat{H}_0 is the time-independent field-free Hamiltonian of the molecular or atomic system under consideration and $\hat{H}_{IR}(t)$ is the Hamiltonian due to a moderately strong IR laser field with associated vector potential $\mathbf{A}(t)$. $\hat{H}_X(t)$ is due to an ionizing XUV laser pulse with duration much shorter than the inverse highest frequency component of the IR laser pulse. The field free Hamiltonian \hat{H}_0 can be further resolved into a kinetic energy part \hat{K} and a potential energy part \hat{U} with the spatial representation $\langle \mathbf{r} | \hat{U} | \mathbf{r}' \rangle = U(\mathbf{r})\delta(\mathbf{r} - \mathbf{r}')$. Our final goal is to find the effects on the photoelectron spectrum of taking this potential in account.

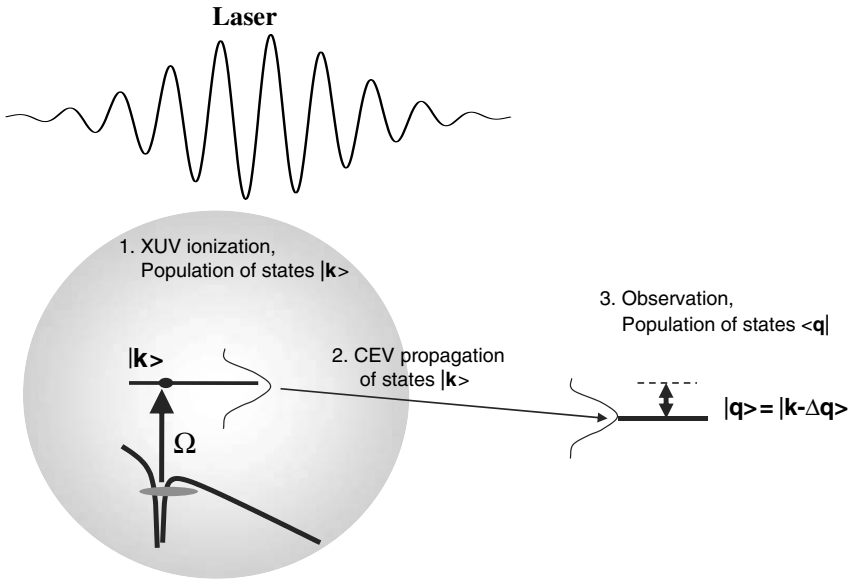


Figure 6.1: XUV ionization in the presence of a moderately strong IR laser field. The XUV pulse with central frequency Ω ionizes an electron, originally in a bound state of the molecule or atom, into a continuum state with asymptotic canonical momentum \mathbf{k} . This \mathbf{k} is conserved during the continuum propagation in SFA, making it the measured photoelectron momentum at the time t_m long after the passage of the pulse, $\mathbf{A}(t_m) = \mathbf{0}$. Our goal shall be to find corrections to this result. The (length gauge) IR dipole potential $\mathbf{r} \cdot \mathbf{E}_{IR}$ is added to the M/A-potential, becoming approximately linear at distances larger than a few atomic units. In this chapter however, the effect of the IR field on the bound state is ignored. In contrast, the effect of the M/A-potential is approximately included in the continuum propagation. We use the CEV propagator, which will affect a shifting of the photoelectron peak by an amount $-\Delta\mathbf{q}$ with respect to the SFA result. The value of $\Delta\mathbf{q}$ is found in section 6.3.2.

We will treat both the IR and XUV field in the dipole approximation, i.e. the fields are constant in space. Furthermore, we will use the length gauge for both fields, and conveniently choose $\mathbf{A}(t_m) = \mathbf{0}$, where t_m is the time where the photoelectron momentum is measured [96]¹. This choice is convenient because the measured kinetic momentum of the electron at time t_m will equal the canonical momentum, which is a conserved quantity in SFA, see Fig. 6.1. In practice, it is always the case that the IR pulse has died out long before the photoelectron spectrum is measured since the duration of moderately strong IR pulses in experiments is at most a few picoseconds, whereas photoelectrons are detected at least hundreds of picoseconds after ionization.

To solve the time-dependent Schrödinger equation we use the time-evolution operators defined by:

$$\begin{aligned} \frac{d}{dt}\hat{U}(t, t') &= -i\hat{H}(t)\hat{U}(t, t'), & \hat{U}(t, t) &= 1 & \text{and} \\ \hat{U}_0(t', t_0) &= e^{-i\hat{H}_0(t'-t_0)}, \end{aligned}$$

whereby the solution fulfilling $|\psi(0)\rangle = |\psi_0\rangle$ is:

$$|\psi(t)\rangle = -i\int_{t_0}^t dt' \hat{U}(t, t') \hat{V}(t') \hat{U}_0(t', t_0) |\psi_0\rangle + \hat{U}_0(t, t_0) |\psi_0\rangle. \quad (6.2)$$

We choose the initial state $|\psi_0\rangle$ to be the ground state of \hat{H}_0 with energy $-I_p$. Our specific interest goes to ionization from this bound state to field free energy eigenstates of \hat{H}_0 with asymptotic momentum \mathbf{q} . Denoting such a state by $|\mathbf{q}\rangle$, we are aiming to find the expansion coefficient $c_{\mathbf{q}} = \langle \mathbf{q} | \psi(t_m) \rangle$ at time t_m long after the IR laser field has died out.

Assuming negligible ionization by the IR laser field, we approximate $\hat{V}(t') \approx \hat{H}_X(t')$. Additionally, we insert two identities² resolved on position states $|\mathbf{r}\rangle$ and on eigenstates $|\mathbf{k}\rangle$ of the Hamiltonian with asymptotic canonical momentum \mathbf{k} :

$$\begin{aligned} c_{\mathbf{q}}(t_m) &= -i \int d\mathbf{k} \int d\mathbf{r} \int_{t_0}^{t_m} dt' \langle \mathbf{q} | \mathbf{r} \rangle \langle \mathbf{r} | \hat{U}(t, t') | \mathbf{k} \rangle \\ &\quad \times \langle \mathbf{k} | \hat{H}_X(t') | \psi_0 \rangle e^{iI_p(t'-t_0)}. \end{aligned} \quad (6.3)$$

¹By choosing the length gauge, the vector potential $\mathbf{A}(t)$ should be understood as $\mathbf{A}(t) = -\int_{-\infty}^t dt' \mathbf{E}_{IR}(t')$, where $\mathbf{E}_{IR}(t')$ is the electric field of the IR laser at time t' .

²Strictly speaking, one must include the bound states also to comprise the full identity. However, since we assume negligible ionization by the IR field, we can restrict this identity to continuum states only.

Note that there is no contribution from the final term in Eq. (6.2) due to $|\mathbf{q}\rangle$ being an eigenstate of \hat{H}_0 .

The XUV laser pulse is assumed to have a Gaussian envelope with duration τ , be centered at time t_X and have carrier frequency Ω . The electric field has the amplitude \mathcal{E}_X along the unit polarization vector $\boldsymbol{\epsilon}$. Furthermore, we use the rotating wave approximation for $H_X(t')$, restricting our attention to absorption:

$$\hat{H}_X(t') = \mathcal{E}_X e^{-\left(\frac{t'-t_X}{\tau}\right)^2} e^{-i\Omega(t'-t_X)} \boldsymbol{\epsilon} \cdot \hat{\mathbf{r}}, \quad (6.4)$$

that is, we omit the complex conjugate of Eq. (6.4) because such a term would be responsible for XUV emission.

We will first illustrate how to find the photoelectron spectrum using the Strong Field Approximation (SFA) and further below consider the effects of including the potential.

6.3.1 The Strong Field Approximation

Neglecting the influence of the potential on the continuum, we approximate the continuum states with Volkov states [90]:

$$\langle \mathbf{r} | \mathcal{U}_{SFA}(t, t') | \mathbf{k} \rangle = \frac{1}{(2\pi)^{\frac{n}{2}}} e^{i\mathbf{p}(t) \cdot \mathbf{r}} e^{-\frac{i}{2} \int_{t'}^t d\xi \mathbf{p}(\xi)^2}, \quad (6.5)$$

where we have introduced the kinetic momentum $\mathbf{p}(t) = \mathbf{k} + \mathbf{A}(t)$. We shall also need $\langle \mathbf{k} | \mathbf{r} \rangle = \langle \mathbf{r} | \mathcal{U}_{SFA}(t', t') | \mathbf{k} \rangle^*$. For the purpose of approximately evaluating the t' -integral, we expand the exponent to second order in $(t' - t_X)$. Since τ is much shorter than the time of variation of $\mathbf{A}(t)$, and by letting the XUV pulse be fired well inside the time-boundaries of the low-frequency pulse, it is legitimate to extend the limits in the t' -integration: $t_0 \rightarrow -\infty$, $t_m \rightarrow \infty$. Hereby, we can perform the t' -integral analytically:

$$c_{\mathbf{q}} = \frac{-i\mathcal{E}_X}{\sqrt{2}(2\pi)^{\frac{n}{2}}} \int d\mathbf{k} \int d\mathbf{r} \frac{1}{\sqrt{1+iF_2}} e^{i[\mathbf{k}-\mathbf{q}] \cdot \mathbf{r}} \times e^{-\frac{i}{2} \int_{t_X}^{t_m} d\xi \mathbf{p}(\xi)^2} e^{-\frac{F_1^2}{1+iF_2}} \boldsymbol{\epsilon} \cdot \langle \mathbf{k} | \hat{\mathbf{r}} | \psi_0 \rangle, \quad \text{where} \quad (6.6)$$

$$F_1 = \frac{\tau}{2} \left[\frac{1}{2} \mathbf{p}(t_X)^2 - (\Omega - I_p) \right],$$

$$F_2 = \frac{\tau^2}{2} \mathbf{p}(t_X) \cdot \boldsymbol{\mathcal{E}}_{IR}(t_X), \quad (6.7)$$

and we have introduced the electric field of the IR laser pulse $\mathcal{E}_{IR}(t) = -\partial\mathbf{A}(t)/\partial t$ and used $\mathbf{A}(t_m) = \mathbf{0}$. Thus, it is seen in Eq. (6.6) that F_1 determines energy conservation within the width determined by τ^{-1} , the spectral width of the XUV pulse, and by F_2 . Please note, that the operator $\hat{\mathbf{r}}$ appearing in the transition matrix element $\langle \mathbf{k} | \hat{\mathbf{r}} | \psi_0 \rangle$ does not depend on the integration variable \mathbf{r} ; it is just the position operator.

We proceed to evaluate the \mathbf{r} - and \mathbf{k} -integrals in Eq. (6.6). This is completely straightforward: The \mathbf{r} -integral yields $(2\pi)^n \delta(\mathbf{q} - \mathbf{k})$, making the \mathbf{k} -integral trivial:

$$c_{\mathbf{q}} = -i \frac{(2\pi)^{\frac{n}{2}} \mathcal{E}_X}{\sqrt{2}\sqrt{1+iF_2}} e^{-\frac{i}{2} \int_{t_X}^{t_m} d\xi [\mathbf{q} + \mathbf{A}(\xi)]^2} e^{-\frac{F_1^2}{1+iF_2}} \boldsymbol{\epsilon} \cdot \langle \mathbf{q} | \hat{\mathbf{r}} | \psi_0 \rangle, \quad (6.8)$$

where the functions F_1 and F_2 are evaluated with $\mathbf{k} = \mathbf{q}$. Apart from phase space factors, the photoelectron spectrum is proportional to:

$$|c_{\mathbf{q}}|^2 = \frac{(2\pi)^n \mathcal{E}_X^2}{2\sqrt{1+F_2^2}} e^{-2\frac{F_1^2}{1+F_2^2}} |\boldsymbol{\epsilon} \cdot \langle \mathbf{q} | \hat{\mathbf{r}} | \psi_0 \rangle|^2. \quad (6.9)$$

It is well-known that this result can differ from both experimental results and from precise numerical simulations, by several orders of magnitude [89], so we should not put much faith in the numerical factors in Eq. (6.9). Conversely, the relative magnitudes are more precise, and with the proper scaling, the photoelectron spectrum generally approximately follows the functional form of Eq. (6.9).

Looking more closely at the spectrum, it is peaked near the values $\mathbf{q} = \mathbf{p}^{(0)}(t_X) - \mathbf{A}(t_X)$ where $|\mathbf{p}^{(0)}(t_X)| = \sqrt{2(\Omega - I_p)}$, as expected from energy conservation. Thus, the M/A-potential is already manifestly included in the SFA model to some extent, demonstrated by the appearance of I_p in the expression for the location of the peak.

For completeness, we consider the two limits $|\mathbf{p}^{(0)}(t_X)| \gg 1/\sqrt{\tau}$; the prevalent experimental situation where the mean energy given to the electron by the XUV pulse at the moment of excitation is much greater than the spread of energies - and the opposite situation $|\mathbf{p}^{(0)}(t_X)| \ll 1/\sqrt{\tau}$. In the first limit, the spectrum is approximately Gaussian in \mathbf{q} :

$$|c_{\mathbf{q}}(t_m)|^2 \sim \exp \left\{ -\frac{[\mathbf{q} - \mathbf{p}^{(0)}(t_X) + \mathbf{A}(t_X)]^2}{2\sigma_{SFA}^2} \right\}, \quad \text{where}$$

$$\sigma_{SFA} = \frac{\sqrt{1 + [\tau^2 \mathbf{p}^{(0)}(t_X) \cdot \mathcal{E}(t_X)/2]^2}}{\tau |\mathbf{p}^{(0)}(t_X)|}.$$

In contrast, in the more hypothetical situation where the mean energy given to the photoelectrons is much smaller than the spectral width of the XUV pulse, the spectrum approximately becomes:

$$|c_{\mathbf{q}}(t_m)|^2 \sim \exp \left\{ -\frac{1}{2} \left[\frac{\mathbf{q} + \mathbf{A}(t_X)}{\sqrt{\tau}} \right]^4 \right\}.$$

Leaving the SFA result behind and returning to the details of the calculation, Eq. (6.6), one notices that we could have omitted introducing the \mathbf{r} -identity all together, instead merely noticing that $\hat{\mathcal{U}}_{SFA}(t, t')$ is diagonal in the canonical momentum base. The reason we introduced this identity anyhow is that we in the following will use a more complicated approximate expression for $\langle \mathbf{r} | \hat{\mathcal{U}}(t, t') | \mathbf{k} \rangle$, preventing an exact evaluation of the \mathbf{k} - and \mathbf{r} -integrals. To clarify this method in a reasonably simple situation, we will evaluate the integrals in Eq. (6.6) once again: This time approximately using the method of stationary phase (MSP). This will serve both as a appetizer on what is to come, and allow us to assess the applicability of MSP for the present problem.

Let $f(\mathbf{y})$ and $\theta(\mathbf{y})$ be real, well-behaved functions of the $2n$ -vector \mathbf{y} and let $\{\mathbf{y}_0\}$ be the set of points where $\theta(\mathbf{y})$ is stationary with respect to its argument, i.e. $\nabla\theta(\mathbf{y}_0) = \mathbf{0}$. Then, MSP says:

$$\int d\mathbf{y} e^{i\theta(\mathbf{y})} f(\mathbf{y}) \approx \sum_{\{\mathbf{y}_0\}} \frac{(2\pi)^n}{\sqrt{|\mathcal{H}(\mathbf{y}_0)|}} f(\mathbf{y}_0) e^{i\theta(\mathbf{y}_0) + i\frac{\pi}{4} \sum_{p=1}^{2n} \text{sgn}\{\lambda_p[\mathcal{H}(\mathbf{y}_0)]\}}, \quad (6.10)$$

where $\mathcal{H}(\mathbf{y})$ is the Hessian of $\theta(\mathbf{y})$, $\lambda_p[\mathcal{H}(\mathbf{y}_0)]$ is the p 'th eigenvalue of $\mathcal{H}(\mathbf{y}_0)$ and sgn denotes the Signum-function³ [97]. The method relies on a so-called asymptotic expansion, and its precision relies on the function $f(\mathbf{y})$ varying slowly with its argument compared to the phase function $\theta(\mathbf{y})$. Therefore, we shall be on the lookout for a small scale parameter in the phase to justify the application of MSP.

Equation (6.6) is already on the form of the left hand side of Eq. (6.10) with $\mathbf{y} = (\mathbf{k}, \mathbf{r})$. To ease the evaluation by MSP, however, we make two additional approximations:

Firstly, the non-constancy of the imaginary part of the factor $1/(1 + iF_2)$ can be ignored at our current level of approximation, both in the exponential and non-exponential factor of Eq. (6.6). When we apply the method of stationary phase, it will be seen that this approximation is sound because we will be

³We can ignore contributions to the integrals from the boundary at infinity due to the F_1 -containing real part decreasing exponentially.

concerned with points close to the zero point of F_1 , and because of the slow variation of this function.

Secondly, we shall neglect the slow variation with \mathbf{k} of the matrix element $\epsilon \cdot \langle \mathbf{k} | \hat{\mathbf{r}} | \psi_0 \rangle$, corresponding to a strongly peaked ground state wave function.

To identify the small parameter, we first consider the energy conserving factor, i.e. the real part of the integrand. This factor varies on a scale, denoted by σ_k , which is independent of $(t_m - t_X)$. To illustrate this, we introduce $\delta \mathbf{k} = \mathbf{k} - \mathbf{p}^{(0)}(t_X) + \mathbf{A}(t_X)$ and consider the limit $|\mathbf{p}^{(0)}(t_X)| \gg 1/\sqrt{\tau}$, where the real part is approximately Gaussian in $\delta \mathbf{k}$:

$$e^{[-F_1^2/(1+F_2^2)]} \approx e^{-\frac{\delta \mathbf{k}^2}{2\sigma_k^2}}, \quad \text{varying on the scale}$$

$$\sigma_k = \sqrt{2} \frac{\sqrt{1 + [\tau^2 \mathbf{p}^{(0)}(t_X) \cdot \mathcal{E}(t_X)/2]^2}}{\tau |\mathbf{p}^{(0)}(t_X)|}.$$

In the opposite limit $|\mathbf{p}^{(0)}(t_X)| \ll 1/\sqrt{\tau}$, the real part varies on a scale of $2/\sqrt{\tau}$, likewise independent of $(t_m - t_X)$.

Next, we consider the phase $\theta(\mathbf{k}, \mathbf{r})$ of the integrand in Eq. (6.6) with the approximations introduced above:

$$\theta(\mathbf{k}, \mathbf{r}) = [\mathbf{k} - \mathbf{q}] \cdot \mathbf{r} - \frac{1}{2} \int_{t_X}^{t_m} d\xi \mathbf{p}(\xi)^2. \quad (6.11)$$

Taking the gradient with respect to \mathbf{k} of the phase $\theta(\mathbf{k}, \mathbf{r})$, we find:

$$\nabla_{\mathbf{k}} \theta(\mathbf{k}, \mathbf{r}) = \mathbf{r} - \mathbf{k}(t_m - t_X) - \int_{t_X}^{t_m} d\xi \mathbf{A}(\xi). \quad (6.12)$$

The phase thus varies with \mathbf{k} on a typical scale of $1/|\nabla_{\mathbf{k}} \theta(\mathbf{k}, \mathbf{r})| \sim 1/[\sigma_k(t_m - t_X)]$, whereas the scale of variation of the real part remains constant with $(t_m - t_X)$ as we saw above. Fortunately, we are precisely interested in the regime of small $1/(t_m - t_X)$, since the measurement of the photoelectron spectrum takes place a macroscopic span of time after the excitation by the XUV pulse. Conclusively, the phase of the integrand varies rapidly with \mathbf{k} compared to the real part, except at the stationary point, validating the use of MSP in this variable. The stationarity condition for \mathbf{k} is obtained from $\nabla_{\mathbf{k}} \theta(\mathbf{k}, \mathbf{r}) = \mathbf{0}$, yielding:

$$\mathbf{0} = \mathbf{r} - \mathbf{k}(t_m - t_X) - \int_{t_X}^{t_m} d\xi \mathbf{A}(\xi). \quad (6.13)$$

Finally, we must justify the use of MSP for \mathbf{r} also. For this purpose we take the \mathbf{r} -gradient of Eq. (6.11):

$$\nabla_{\mathbf{r}}\theta(\mathbf{k}, \mathbf{r}) = \mathbf{k} - \mathbf{q}. \quad (6.14)$$

Using the condition Eq. (6.13) in the real part of the integrand (i.e. putting it into F_1 in the exponent), we find that this part varies with \mathbf{r} on a scale $\sigma_r \propto (t_m - t_X)$ near the stationary point of \mathbf{k} . Conversely, the phase varies with \mathbf{r} on the scale $1/|\nabla_{\mathbf{r}}\theta(\mathbf{k}, \mathbf{r})| \sim \sigma_k$, independent of $(t_m - t_X)$. Once more, the macroscopic time $(t_m - t_X)$ serves to validate the method of stationary phase: This time for the \mathbf{r} -integral⁴.

Having validated MSP for all variables, we simultaneously use the two stationarity conditions $\nabla_{\mathbf{r}}\theta(\mathbf{k}, \mathbf{r}) = \mathbf{0}$:

$$\mathbf{k} = \mathbf{q}, \quad (6.15)$$

and Eq. (6.13) to evaluate the integrals in Eq. (6.6)⁵. Noticing that $|\mathcal{H}| = 1$, the MSP yields the same result as the exact calculation, Eq. (6.8).

As a final note, the expressions Eq. (6.13) and (6.15) give the classical path of a free electron in the field, and predict the electron having the position $\mathbf{r} = \mathbf{0}$ at the moment of ionization t_X .

$$\mathbf{r}_{SFA}(t) = [\mathbf{q} - \mathbf{A}(t_X)](t - t_X) + \int_{t_X}^t d\xi \mathbf{A}(\xi). \quad (6.16)$$

What distinguishes the origin is our neglect of variation of $\epsilon \cdot \langle \mathbf{k} | \hat{\mathbf{r}} | \psi_0 \rangle$, predicting a ground state wave function $\psi_0(\mathbf{r}) \propto \delta(\mathbf{r})/\epsilon \cdot \mathbf{r}$, which is strongly peaked at the origin. We will have more to say about this in the discussion, section 6.4.

6.3.2 The M/A-potential corrected case

In the calculations of the SFA photoelectron spectrum, Eq. (6.9) above, we completely ignored the effects of the M/A-potential on the continuum. In this subsection, we will semiclassically include the potential and find the consequent modifications to the photoelectron spectrum. To accomplish this, we shall make

⁴Hearing the term "Strong Field Approximation", one might initially had expected that the small parameter validating MSP was connected with $1/|\mathbf{A}|$. On the contrary, the small parameter is $1/(t_m - t_X)$, independent of the magnitude of \mathbf{A} , precisely as in the exact calculation, Eq. (6.8). One must remember, though, that we used the strongness of the field at a much earlier stage, namely in using the approximation Eq. (6.5).

⁵Due to the form of $\theta(\mathbf{k}, \mathbf{r})$, the condition Eq. (6.13) plays no role in this particular case. In general, however, all stationarity conditions must be included simultaneously.

use of the CEV-functions instead of Volkov-waves as approximations to the continuum eigenfunctions of the Hamiltonian. These functions are of the eikonal form [17]:

$$\psi(\mathbf{r}, t) = e^{i\Theta(\mathbf{r}, t)}. \quad (6.17)$$

The CEV-functions are found through inserting Eq. (6.17) in the Schrödinger equation, whereby one arrives at a partial differential equation for the phase $\Theta(\mathbf{r}, t)$. Apart from the usual approximation of neglecting a term of the form $\nabla_{\mathbf{r}}^2 \Theta(\mathbf{r}, t)$, the equation for the phase is expanded around the Volkov-phase, keeping only first order correction terms in $U(\mathbf{r})/\mathbf{k}^2$. With appropriate boundary conditions, this leads to the CEV states below [91].

As in subsection 6.3.1, we start from Eq. (6.3), where now the true continuum states $|\mathbf{k}\rangle$ will be approximated by CEV-states [80]:

$$\begin{aligned} \langle \mathbf{r} | \hat{\mathcal{U}}_{CEV}(t, t') | \mathbf{k} \rangle &= \frac{1}{(2\pi)^{\frac{n}{2}}} e^{i\mathbf{p}(t) \cdot \mathbf{r}} e^{-\frac{i}{2} \int_{t'}^t d\xi \mathbf{p}(\xi)^2} \\ &\times e^{-i \int_{t'}^t d\xi U[\mathbf{r}_{IR}(\xi, t)]} e^{-\frac{i}{|\mathbf{p}(t')|} \int_{\mathbf{r}_0}^{\mathbf{r}_{IR}(t', t)} dl U[\mathbf{r}'(l)]}, \end{aligned} \quad (6.18)$$

where \mathbf{r}_0 is an arbitrary reference point, and the path parameterized by l must be specified. This path is most conveniently chosen to be the classical path followed by an electron in the absence of the potential U , as in the classical eikonal approximation [17]. The classical trajectory of the electron \mathbf{r}_{IR} appearing in Eq. (6.18) is given by an equation like Eq. (6.16):

$$\mathbf{r}_{IR}(t_1, t_2) = \mathbf{r} + \mathbf{k}(t_1 - t_2) + \int_{t_2}^{t_1} dt'' \mathbf{A}(t''),$$

i.e. we will need the trajectory $\mathbf{r}_{IR}(t', t_m)$ for which the electron arrives at the point \mathbf{r} at time $t' = t_m$ with kinetic momentum $\mathbf{k} + \mathbf{A}(t_m) = \mathbf{k}$. From this equation and Eq. (6.18), we see that $\langle \mathbf{q} | \mathbf{r} \rangle = \frac{1}{(2\pi)^{n/2}} e^{-i\mathbf{q} \cdot \mathbf{r} + \frac{i}{|\mathbf{q}|} \int_{\mathbf{r}_0}^{\mathbf{r}} dl U[\mathbf{r}'(l)]}$.

The CEV functions contain the Volkov function in the first three factors, i.e. the first line of Eq. (6.18), and the second line are corrections to the Volkov function stemming from the M/A-potential. The reference point \mathbf{r}_0 is set by the aforementioned appropriate boundary conditions, and signify a point where the Volkov and CEV phases coincide when $t = t'$.

Throughout the rest of the calculation, we shall consistently use the same strategy as in the SFA case, but keeping only corrections to first order in U/\mathbf{k}^2 . Like before, we shall make use of MSP, the applicability of which follows from arguments completely analogous to the ones given in section 6.3.1.

As in the SFA-case, we expand the exponent to second order in $(t' - t_X)$ and perform the t' -integral. Because the overall normalization of $c_{\mathbf{q}}$ is incorrect, we shall not write out overall numerical factors:

$$\begin{aligned}
c_{\mathbf{q}}(t_m) &\propto \mathcal{E}_X \int d\mathbf{k} \int d\mathbf{r} \boldsymbol{\epsilon} \cdot \langle \mathbf{k} | \hat{\mathbf{r}} | \psi_0 \rangle \frac{1}{\sqrt{1 + iF'_2}} e^{i[\mathbf{k} - \mathbf{q}] \cdot \mathbf{r}} \\
&\times e^{\frac{i}{|\mathbf{q}|} \int_{\mathbf{r}_0}^{\mathbf{r}} dU[\mathbf{r}'(l)] - \frac{i}{2} \int_{t_X}^{t_m} d\xi \mathbf{p}(\xi)^2 - i \int_{t_X}^{t_m} d\xi U[\mathbf{r}_{IR}(\xi, t_m)]} \\
&\times e^{-\frac{i}{|\mathbf{p}(t_X)|} \int_{\mathbf{r}_0}^{\mathbf{r}_{IR}(t_X, t_m)} dU[\mathbf{r}'(l)]} e^{\left[-\frac{F_1'^2}{1 + iF_2'} \right]}, \tag{6.19}
\end{aligned}$$

where

$$\begin{aligned}
F_1' &= \frac{\tau}{2} \left\{ \frac{1}{2} \mathbf{p}(t_X)^2 - (\Omega - I_p) - \frac{\boldsymbol{\mathcal{E}}_{IR}(t_X) \cdot \mathbf{p}(t_X)}{|\mathbf{p}(t_X)|^3} \int_{\mathbf{r}_0}^{\mathbf{r}_{IR}(t_X, t_m)} dl U[\mathbf{r}'(l)] \right\}, \\
F_2' &= \frac{\tau^2}{2} \left\{ \mathbf{p}(t_X) \cdot \boldsymbol{\mathcal{E}}_{IR}(t_X) \left[1 + \frac{U[\mathbf{r}_{IR}(t_X, t_m)]}{\mathbf{p}(t_X)^2} \right] \right. \\
&\quad \left. + \left[\frac{\partial \boldsymbol{\mathcal{E}}_{IR}(t_X) \cdot \mathbf{p}(t_X)}{\partial t_X} - \boldsymbol{\mathcal{E}}_{IR}^2 \right] \frac{1}{|\mathbf{p}(t_X)|^3} \int_{\mathbf{r}_0}^{\mathbf{r}_{IR}(t_X, t_m)} dl U[\mathbf{r}'(l)] \right\}.
\end{aligned}$$

A striking thing about these expressions is that they would appear to depend on the reference point \mathbf{r}_0 . The situation is less dire than this, but we must take care in choosing this point most conveniently. The apparent problem arises because the placidly looking matrix element $\langle \mathbf{k} | \hat{\mathbf{r}} | \psi_0 \rangle$ is different from the one in subsection 6.3.1, which involved a Volkov state. Here, $\langle \mathbf{k} |$ is a CEV bra and contains the reference phase connected to the point \mathbf{r}_0 .

Had we been dealing with scattering, it would probably have been most clear to let $\mathbf{r}_0 = -\alpha \mathbf{k}$, where α is a asymptotically large positive number, i.e. fix the phase of the CEV functions to incoming plane wave scattering states. The present situation is much different, however, in that we wish to compare the behavior of electrons excited into the continuum near the molecule or atom using the SFA- contra the CEV approximation. Thus, maintaining that we wish to ignore the non-constancy with \mathbf{k} of $\langle \mathbf{k} | \hat{\mathbf{r}} | \psi_0 \rangle$ and examine the different behaviors from the semi-classical point of ionization to the detector, we must choose the reference point to coincide with the ionization point $\mathbf{r}_0 = \mathbf{r}_{IR}(t_m, t_X)$. To first order in U/\mathbf{k}^2 , this is the origin as in the SFA treatment, see Eq. (6.16). We stress again that this whole business with choosing \mathbf{r}_0 arose due to the approximation on the dipole transition moment, and would be absent if this

was taken fully into account⁶.

With the choice $\mathbf{r}_0 = \mathbf{r}_{IR}(t_m, t_X)$, the expressions for F'_1 and F'_2 are considerably simplified. Moreover, since $\mathbf{r}_{IR}(t_X, t_m)$ enters only in the potential function U , first order contributions uses the trajectory from SFA for the electron and thus set $\mathbf{r}_{IR}(t_X, t_m) = \mathbf{0}$. This also makes good physical sense, since the electron must be liberated where the ground state wave function is non-zero. Because the point of ionization $\mathbf{r}_{IR}(t_X, t_m)$ will appear several times, we will abbreviate it as:

$$\mathbf{r}_{poi} \equiv \mathbf{r}_{IR}(t_X, t_m), \quad (6.20)$$

remembering that $\mathbf{r}_{poi} = \mathbf{0}$ at our current level of approximation, but may be different in more advanced treatments, e.g. if the non-constancy of the transition dipole moment is taken in to account.

With these choices, we shall hereafter use for the functions F'_1 and F'_2 :

$$\begin{aligned} F'_1 &= \frac{\tau}{2} \left[\frac{1}{2} \mathbf{p}(t_X)^2 - (\Omega - I_p) \right] = F_1, \\ F'_2 &= \frac{\tau^2}{2} \mathbf{p}(t_X) \cdot \mathcal{E}_{IR}(t_X) \left[1 + \frac{U(\mathbf{r}_{poi})}{\mathbf{p}(t_X)^2} \right]. \end{aligned}$$

We proceed to approximately evaluate the \mathbf{k} - and \mathbf{r} -integrals in Eq. (6.19) using MSP. Once again, we neglect the slow variation with \mathbf{k} of the matrix element $\langle \mathbf{k} | \hat{\mathbf{r}} | \psi_0 \rangle$ and of the phase of $e^{-F'_1/(1+iF'_2)}$.

The first step in MSP is to find the stationary point. By taking the \mathbf{k} -gradient of the phase in Eq. (6.19), we obtain the first n stationarity conditions:

$$\mathbf{0} = \mathbf{k} - \mathbf{q} - \Delta \mathbf{q}(\mathbf{k}, \mathbf{r}) + \mathbf{w}_{\mathbf{k}}(\mathbf{k}, \mathbf{r}), \quad \text{where} \quad (6.21)$$

$$\Delta \mathbf{q}(\mathbf{k}, \mathbf{r}) = \int_{t_X}^{t_m} d\xi \nabla U[\mathbf{r}_{IR}(\xi, t_m)] + \frac{\mathbf{p}(t_X)}{\mathbf{p}(t_X)^2} U(\mathbf{r}_{poi}), \quad (6.22)$$

$$\mathbf{w}_{\mathbf{k}}(\mathbf{k}, \mathbf{r}) = \frac{\mathbf{q}}{q^2} U(\mathbf{r}),$$

and ∇U means the gradient of U with respect to its argument. Using the SFA trajectory Eq. (6.16), we see that $|\mathbf{r}| \rightarrow \infty$ for $(t_m - t_X) \rightarrow \infty$. Since $\lim_{|\mathbf{r}| \rightarrow \infty} U(\mathbf{r}) = 0$, we can ignore the term $\mathbf{w}_{\mathbf{k}}(\mathbf{k}, \mathbf{r})$, and the whole correction with respect to SFA is $\Delta \mathbf{q}(\mathbf{k}, \mathbf{r})$.

⁶A quick-'n-dirty argument to arrive immediately at the right result would be that the physical results must be independent of the choice of reference point, so the quantities explicitly containing \mathbf{r}_0 must add to zero.

Taking the \mathbf{k} -gradient of the phase in Eq. (6.19) leads us to the last n stationarity conditions:

$$\begin{aligned} \mathbf{0} &= \mathbf{r} - (t_m - t_X)\mathbf{k} - \int_{t_X}^{t_m} d\xi \mathbf{A}(\xi) \\ &\quad + (t_m - t_X)\mathbf{R} + \mathbf{w}_r(\mathbf{k}, \mathbf{r}), \quad \text{where} \quad (6.23) \\ \mathbf{w}_r(\mathbf{k}, \mathbf{r}) &= - \int_{t_X}^{t_m} d\xi \nabla U[\mathbf{r}_{IR}(\xi, t_m)](\xi - t_X), \end{aligned}$$

and we have used $\mathbf{r}_0 = \mathbf{r}_{poi}$. The term $\mathbf{w}_r(\mathbf{k}, \mathbf{r})$ grows at most as rapidly⁷ as $\ln(t_m - t_X)$ when $(t_m - t_X)$ grows large, and can thus be neglected compared to the other terms, which are asymptotically proportional to $(t_m - t_X)$ in the same limit⁸.

The equations (6.21) and (6.23) are not easily solved simultaneously for \mathbf{k} and \mathbf{r} . However, since we are calculating the correction to first order only, we will use the results from the SFA calculation in the correction term $\Delta\mathbf{q}(\mathbf{k}, \mathbf{r})$. From this point on, we will therefore use $\mathbf{k} = \mathbf{q}$ from Eq. (6.15) wherever \mathbf{k} appears in $\Delta\mathbf{q}(\mathbf{k}, \mathbf{r})$ and use the trajectory from SFA, Eq. (6.16), in place of $\mathbf{r}_{IR}(\xi, t_m)$. With these approximations, we obtain:

$$\mathbf{k} = \mathbf{q} + \Delta\mathbf{q}^{(1)}, \quad \text{where} \quad (6.24)$$

$$\Delta\mathbf{q}^{(1)} = \int_{t_X}^{t_m} d\xi \nabla U[\mathbf{r}_{SFA}(\xi)] + \frac{\mathbf{p}^{(1)}(t_X)}{\mathbf{p}^{(1)}(t_X)^2} U(\mathbf{r}_{poi}), \quad (6.25)$$

and $\mathbf{p}^{(1)}(t_X) = \mathbf{q} + \Delta\mathbf{q}^{(1)} + \mathbf{A}(t_X)$.

With these approximations, we can evaluate the integrals in Eq. (6.19) using MSP and find the photoelectron spectrum apart from phase space factors. To first order, we can use the Hessian determinant $|\mathcal{H}| = 1$ from SFA, and we obtain:

$$|c_{\mathbf{q}}|^2 \propto \frac{\mathcal{E}_X^2}{\sqrt{1 + F_2'^2}} \left| \boldsymbol{\epsilon} \cdot \langle \mathbf{q} + \Delta\mathbf{q}^{(1)} | \hat{\mathbf{r}} | \psi_0 \rangle \right|^2 e^{\left[-2 \frac{F_1^2}{1 + F_2'^2} \right]}, \quad (6.26)$$

where F_1 and F_2' are evaluated with $\mathbf{k} = \mathbf{q} + \Delta\mathbf{q}^{(1)}$. Comparing this result with the SFA spectrum, Eq. (6.9), we see three main differences. Firstly, the width

⁷The logarithmic growth is for potentials of the large- \mathbf{r} asymptotic form $U(\mathbf{r}) \sim -Z/|\mathbf{r}|$. For short range potentials, $\mathbf{w}_r(\mathbf{k}, \mathbf{r})$ approaches a constant for $(t_m - t_X) \rightarrow \infty$.

⁸One could say the same about $\int_{t_X}^{t_m} d\xi \mathbf{A}(\xi)$, but we retain this for cosmetic purposes, i.e., its appearance in the exact SFA result, Eq. (6.13).

function F_2' is multiplied by the small correction factor $1 + U(\mathbf{r}_{poi})/\mathbf{p}^{(1)}(t_X)^2$. Secondly, as already touched upon, the bra $\langle \mathbf{k} |$ entering in the transition dipole matrix element $\langle \mathbf{k} | \hat{\mathbf{r}} | \psi_0 \rangle$ denotes a CEV state rather than a Volkov state. Thirdly and most importantly, the form of the spectrum is approximately retained, but is shifted an amount $\Delta \mathbf{q}^{(1)}$ compared to the SFA spectrum. The new maximum is near $\mathbf{q} = \mathbf{p}^{(0)}(t_X) - \mathbf{A}(t_X) - \Delta \mathbf{q}^{(1)}$, with $|\mathbf{p}^{(0)}(t_X)| = \sqrt{2(\Omega - I_p)}$ as before.

The momentum shift $\Delta \mathbf{q}^{(1)}$ has a simple classical interpretation, which becomes clear when we write:

$$\Delta \mathbf{q}^{(1)} = \int_{t_X}^{t_m} d\xi \nabla U[\mathbf{r}_{SFA}(\xi)] - \int_{t_X}^{t_m} d\xi \nabla U[\mathbf{p}^{(1)}(t_X)(\xi - t_X)], \quad (6.27)$$

i.e. the shift is the impulse given to the electron by the potential through following the classical path in the laser field minus the impulse that would have been experienced in the absence of the laser field. This field-free path can be written:

$$\mathbf{r}_{ff}(\xi) = \mathbf{r}_{poi} + (\xi - t_X)[\mathbf{q} + \mathbf{A}(t_X)],$$

where we used that $\Delta \mathbf{q}^{(1)}$ can be neglected in the argument of U .

One immediately sees that the shift $\Delta \mathbf{q}^{(1)}$ is characteristic of the coupling between the M/A-potential and the laser, in the sense stated towards the end of section 6.2, since it would be zero in the absence of either. This is reasonable since the ionization potential is already included in the SFA case through the energy conserving factor containing $\mathbf{p}(t_X)^2 = \Omega - I_p$. Indeed, if the ionization potential $I_p \ll \mathbf{p}(t_X)^2/2$, the consequent correction to the momentum $|d\mathbf{p}| \ll |\mathbf{p}(t_X)|$ is $d\mathbf{p} \cdot \mathbf{p}(t_X) \approx -I_p$, so $d\mathbf{p} \approx -\mathbf{p}(t_X)I_p/\mathbf{p}(t_X)^2$, which is the correction already present in the SFA treatment and the cause of the second term in Eq. (6.25). The inability of the theory presented here to differ between I_p and $U(\mathbf{r}_{poi})$ is a consequence of the semi-classical approach where the continuum electron has a semi-classical position.

Thus, the last term in the shift $\Delta \mathbf{q}^{(1)}$, Eq. (6.25) is a cancelation of the (zero order) impulse already present in the SFA result, whereas the first term is the total (zero and first order) impulse accumulated from the M/A-potential on the electron's path.

Though the second term in Eq. (6.25) does not exactly cancel the correction present in SFA due to the difference between $U(\mathbf{0})$ and $-I_p$, the result is still valid. Both U and the semi-classical path are treated in the same way in the two terms as clearly seen in Eq. (6.27).

Recalling the end of section 6.2, the continuum wave function were suggested separated into two parts. The first, $\psi_{\mathbf{k}}(\mathbf{r})$, is a coordinate function which is determined by \hat{U} because it is an eigenfunction of \hat{H}_0 with asymptotic canonical momentum \mathbf{k} . Thus, depending on the gauge, the coordinate part can depend on the laser field through its kinetic momentum $\mathbf{k} + \mathbf{A}(t)$, but only in a trivial way: The laser field supplies asymptotic kinetic momentum. The second part, $\phi(t) = e^{i \int^t d\xi [\mathbf{k} + \mathbf{A}(\xi)]^2}$ is identical to the Volkov phase, and in the case of Coulomb potentials, the total wave function approximation is known as the "Coulomb-Volkov" functions [93]:

$$\langle \mathbf{r} | \mathbf{k} \rangle_t \approx \psi_{\mathbf{k}}(\mathbf{r}) e^{i \int^t d\xi [\mathbf{k} + \mathbf{A}(\xi)]^2}. \quad (6.28)$$

Since the Volkov functions themselves were exactly of this form, it is in this respect $\Delta \mathbf{q}^{(1)}$ can be said to quantify an estimate of the extent to which this separation breaks down. For want of a better term, this breakdown is called "Potential-Laser coupling" although the Hamiltonian involves no term where both $\mathbf{A}(t)$ and \hat{U} enters.

6.4 Discussion

In this section, we will discuss the results, especially the expression for the momentum shift $\Delta \mathbf{q}^{(1)}$. In subsection 6.4.1, we illustrate the correctness of the above calculation with a numerical example. In subsection 6.4.2, we make a brief comment about a prior use of an expression similar to $\Delta \mathbf{q}^{(1)}$ in the strong field literature. In subsection 6.4.3, we discuss the problems with the above treatment for the case of singular potential functions, and why we used MSP instead of the related Method of Steepest Descent. In subsection 6.4.4, we compare our results with the related work [93] on Coulomb-Volkov functions and comment on the implications for HHG mentioned in the introduction.

6.4.1 Numerical calculations

The analytic, but approximate expression Eq. (6.25) is compared with numerical calculations in Fig. 6.2. The figure shows the shift of the photoelectron spectrum's maximum using CEV states compared to results obtained using Volkov states. For the calculations, we have chosen parameters typical of an experimental situation and used the numerical, but unpolarized, ground state for the system. The approximate analytical expression Eq. (6.25) is seen to match the numerical results well, illustrating the validity of applying MSP.

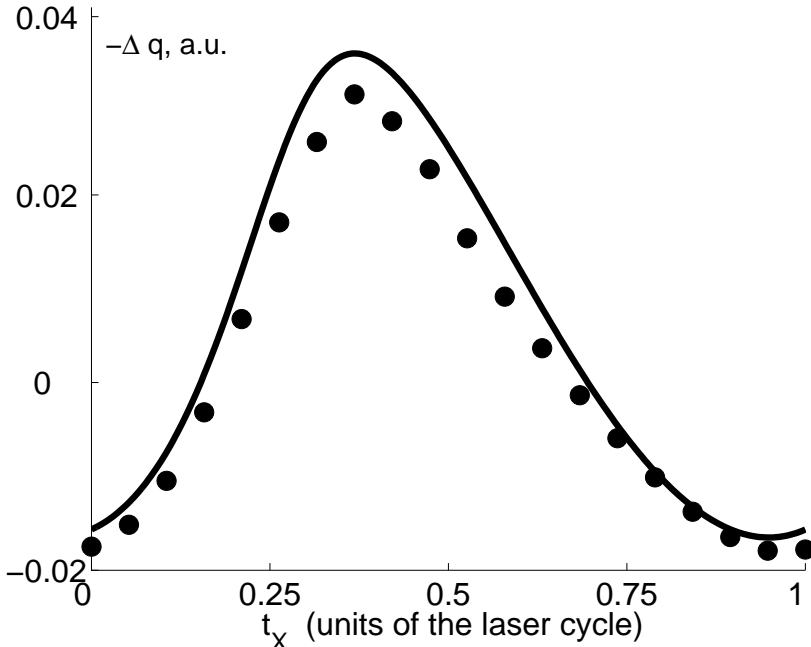


Figure 6.2: Numerical momentum shift of the photoelectron spectrum's maximum compared to the SFA-result due to the potential-laser coupling. The numerical calculation is carried out for a one dimensional model. The first axis denotes the delay of the IR electric field at the time t_X of XUV ionization, in units of the IR field's period. The second axis denotes the momentum shifts compared to the result found using SFA, where potential-laser coupling effects in the continuum are completely ignored. The solid curve is found from the analytic expression Eq. (6.25), the points show numerical calculations starting from Eq. (6.3). In these calculations, the potential is $U(x) = -1/\sqrt{x^2 + a^2}$ with $a = 1.59$, giving $I_p = 12.13$ eV. The IR field has vector potential $A(t) = 1.14 \sin(0.057t)$ corresponding to a wavelength of 800nm, and the XUV pulse has $\Omega = 3 = 81.6$ eV and a duration of 200 attoseconds. In all results, the polarization of the bound state has been neglected. While the polarization gives corrections of the same order as the potential-laser coupling, both effects are small, and their corrections are approximately additive. Therefore, polarization effects could be included at a later stage [91], and the figure shows the effects potential-laser coupling.

6.4.2 Prior uses of $\Delta\mathbf{q}^{(1)}$

Concerning existing works related to this chapter, a correction similar to Eq. (6.25) has been used to examine asymmetries in the angular distributions of ionized electrons from above threshold ionization, i.e. more photons than necessary for ionization is absorbed from the strong IR field, of xenon atoms using elliptically polarized light [98]. There, the point of ionization was taken to be the classical point of closest approach of an electron in the combined M/A-potential and slowly-varying field. However, only the first term in Eq. (6.25) was used and the treatment was completely classical. Due to the situation in [98] being very different from the present, it is difficult to make a closer comparison.

6.4.3 Divergent potentials and the Method of Steepest Descent

A problem with the momentum shift in Eq. (6.25) is that it uses $U(\mathbf{r}_{poi})$, where the treatment above yielded $\mathbf{r}_{poi} = \mathbf{0}$. If the potential function has divergencies, as, e.g., the Coulomb potential, our treatment, as it stands, crumbles away. The symptom of this is the appearance of a semiclassical position of the electron given by Eq. (6.16), rather than a wavelike behavior. The breakdown happens at a much earlier stage though, namely in the use of the eikonal technique, which requires the wave function to vary rapidly compared to the potential and that $U(\mathbf{r})/\mathbf{k}^2$ be small for all \mathbf{r} [17]. The latter requirement was also used explicitly in the derivation of the CEV functions. An often applied way to salvage the application of semi-classical approaches from such difficulties is to use a different, but similar, potential function. For instance, the commonly used soft-Coulomb potential $U(\mathbf{r}) = -1/\sqrt{\mathbf{r}^2 + a^2}$ was used in the calculations leading to Fig. 6.2.

Another route one could speculate in is using the method of steepest descent (MSD) instead of MSP in evaluating the integrals in Eq. (6.19) [99]. Here, one will often find an imaginary component of the electron's position, while only the real part varies in time, thereby avoiding the inauspicious singularity. We will give a brief summary of how one would have gone about using MSD and the considerations that led us to prefer MSP.

In the MSD, the stationarity conditions involve both the real- and imaginary parts of the exponent. For instance, one can include the transition dipole moment in the exponent through $\epsilon \cdot \langle \mathbf{k} | \hat{\mathbf{r}} | \psi_0 \rangle = \exp[\ln(\epsilon \cdot \langle \mathbf{k} | \hat{\mathbf{r}} | \psi_0 \rangle)]$, thus changing the point of ionization to:

$$\mathbf{r}_{poi} = i \frac{\nabla_{\mathbf{q}} (\epsilon \cdot \langle \mathbf{q} | \hat{\mathbf{r}} | \psi_0 \rangle)}{\epsilon \cdot \langle \mathbf{q} | \hat{\mathbf{r}} | \psi_0 \rangle}.$$

This generally contains a non-vanishing imaginary part - indeed, it is purely imaginary if $|\psi_0\rangle$ is a parity eigenstate. The MSD predicts how one can extend the integrand to accepting also complex values of the argument \mathbf{r} , rather than just the real values used in MSP. The prescription is to use the analytic continuation of the integrand and evaluate this at the stationary points. However, the use of MSD is only solidly founded for single integrals, and cannot generally be extended to multiple integrals⁹ [97], [100]. Thus, using MSD for $n = 1$, one would have to evaluate the k - and x -integrals as iterated integrals, most practically in that order. Using the Coulomb potential as an example, the analytical continuation the potential function $U(x) = -1/\sqrt{x^2}$ is:

$$U(x) = -\frac{1}{\sqrt{x^2}} = -\frac{\cos(\phi/2) + i \sin(\phi/2)}{\sqrt{\Re(x)^2 + \Im(x)^2}}, \text{ where} \quad (6.29)$$

$$x = |x|e^{i\phi},$$

\Re denotes the real part of the argument, \Im the imaginary, and one has to impose a branch cut that the zero-order path does not cross. After the field has died out, the integration path could then be brought back to the real axis.

However, because of the many difficulties with extending MSD to $n > 1$ and because of the violation of the condition $U(\mathbf{r})/\mathbf{k}^2$ on the much earlier stage of applying the CEV functions, we have preferred MSP. Consequently, we will assume that the potential $U(\mathbf{r})$ has no divergencies, or an equivalent potential without divergencies has been used in its stead.

6.4.4 On the applicability of CEV and Coulomb-Volkov states

We turn to discuss the implications of our results for the precision of the Coulomb-Volkov separation mentioned at the end of section 6.3.2, and we compare with the applicability of the CEV functions. For this, we first estimate the magnitude of the potential-laser coupling for regularized Coulomb potentials $U(\mathbf{r}) = -Z/\sqrt{\mathbf{r}^2 + a^2}$.

We rewrite Eq. (6.25) using partial integration. Requiring that $\mathbf{q} + \mathbf{A}(t) \neq \mathbf{0}$ for all $t \in [t_X, t_m]$, we find:

$$\Delta \mathbf{q}^{(1)} = -\int_{t_X}^{t_m} d\xi \frac{\mathcal{E}_{IR}(\xi)}{[\mathbf{q} + \mathbf{A}(\xi)]^2} U \left[\mathbf{r}_{poi} + \mathbf{q}(\xi - t_X) + \int_{t_X}^{\xi} dt'' \mathbf{A}(t'') \right]. \quad (6.30)$$

⁹For instance, a function of a single real variable has a unique analytic continuation to a function of a single complex variable. Such a theorem does not exist for functions of several real variables.

We can estimate the magnitude of this integral by noticing that most of it is accumulated during the time from t_X to $t_X + 2/\omega$, where ω is the central angular frequency of the IR field:

$$\begin{aligned} |\Delta \mathbf{q}^{(1)}| &\sim \frac{Z \mathcal{E}_{IR}}{|\mathbf{p}^{(0)}|^3} \ln \left(\frac{4|\mathbf{p}^{(0)}|}{a\omega} \right), \\ &= \frac{Z \mathcal{E}_{IR}}{2\sqrt{2}(\Omega - I_p)^{\frac{3}{2}}} \ln \left[4\sqrt{2} \frac{\sqrt{\Omega - I_p}}{\omega a} \right]. \end{aligned} \quad (6.31)$$

Here we have used that $2|\mathbf{p}^{(0)}|/\omega \gg a$, \mathcal{E}_{IR} is the IR laser's electric field magnitude, and $\mathbf{p}^{(0)2}/2 = \Omega - I_p$ as before. It may be noted that the dependencies on a , the potential's regularization, and ω are slow since they are only found in the logarithm, whose argument $4|\mathbf{p}^{(0)}|/(a\omega) \gg 1$. Both the use of the CEV functions and the truncation of corrections at first order requires the first order shift to be much smaller than the zero order momentum, $|\Delta \mathbf{q}^{(1)}| \ll |\mathbf{q}|$. For these two methods to be precise, Eq. (6.31) hence leads to the condition:

$$Z \mathcal{E}_{IR} \ll \frac{4(\Omega - I_p)^2}{\ln \left[4\sqrt{2} \frac{\sqrt{\Omega - I_p}}{\omega a} \right]}. \quad (6.32)$$

In contrast, for the separation of the continuum wave function into the Coulomb-Volkov form to be precise, the phase shift from Coulomb-laser coupling across the molecule or atom of size R must be small, $|\Delta \mathbf{q}^{(1)}|R \ll 1$, leading to the condition:

$$Z \mathcal{E}_{IR} R \ll \frac{2\sqrt{2}(\Omega - I_p)^{\frac{3}{2}}}{\ln \left[4\sqrt{2} \frac{\sqrt{\Omega - I_p}}{\omega a} \right]}. \quad (6.33)$$

The condition (6.33), except for the slow-varying logarithmic factor, agrees with the condition of applicability found by other means for an atom with $R \approx 1$ in [93]¹⁰. For usual experimental parameters, and the additional condition $\Omega \gg I_p$

¹⁰Actually, both [87] and [93] use the so-called "sudden approximation", where the acceleration of the electron by the IR field is ignored while the electron moves across the molecule or atom. On one hand, this acceleration is usually negligible in HHG considerations because the HHG emission takes place at times close to the zero of the generating laser's electric field [93]. On the other hand, when the electric field is not close to zero, as in general for laser-assisted XUV ionization, this acceleration effect causes phase shifts easily surpassing the ones from Coulomb-laser coupling. The sudden approximation is not made in [94] and [95].

used in [93] in particular, $|\mathbf{p}^{(0)}| \gg 1$ so the condition of separability is more restrictive than the applicability condition for the CEV functions, Eq. (6.32). As a realistic numerical example relevant for HHG, setting $Z = 1$, $\Omega - I_p = 0.74 = 20$ eV and $\mathcal{E}_{IR} = 0.05$, the Coulomb-laser phase shift is smaller than 0.05 for $R \lesssim 6 \approx 3\text{\AA}$. Thus, Coulomb-laser coupling can be ignored for very small molecules in this energy range, i.e. the Coulomb-Volkov functions are a precise description of the continuum for e.g. N_2 , while CO_2 is borderline.

Armed with these estimates, we can finally address the generation of HHG using aligned diatomic molecules - the time inverse process of XUV ionization. When there are several, well separated ionization centers, it has been proposed to view these centers as point emitters of radiation [84]-[86]. In this case, it is natural to expect interference in the HHG yield at different frequencies, the exact nature of which depends on the angle between the molecular axis and laser polarization. This interference is caused by the different quantum mechanical phases of the continuum wave function at the different ionization centers during recombination. Here, the challenging point has proven to be finding a relation between the frequency of the harmonic radiation and both the asymptotic momentum and the near-core phase variations of the continuum wave function; similar to a dispersion law. Indeed, in investigations using plane waves, it is found that the energy of the continuum state must be the asymptotic kinetic energy plus a fraction of the ionization potential, the last of which varies from case to case [84]-[86]. This ambiguity is naturally not found in numerical calculations using the full Schrödinger equation, but borne out of the desire for an physical understanding of the HHG emitting recombination process. Equally important, the full numerical calculation in three spatial dimensions is still intractable on present day computers, making physically sound approximate models vital. With the results of Coulomb-laser coupling held, we can remove the ambiguity of these former models in the situation where this coupling is negligible.

In this separable case, one may obtain an intuitive understanding by using the separable states in the final recombination step. The complicated continuum wave function is then replaced with the much better known field free state with asymptotic kinetic momentum determined by the laser field¹¹, $\mathbf{p}^2/2 = N\omega - I_p$, where N is the number of absorbed photons of angular frequency ω . Thus, the interference structures in the HHG emission should coincide with those of XUV ionization in absence of the IR field, and with an XUV photon energy of

¹¹Again, if one wishes to use the sudden approximation from footnote 10, there must be negligible acceleration of the electron as it moves across the parent ion.

$\Omega = N\omega$. This correspondence was recently found numerically in [87]. Lastly, such a correspondence between frequency of emitted HHG radiation and the spatial shape of the continuum wave function precisely forms the foundation for the tomographic reconstruction of molecular orbitals in [35], as stated in section 6.2.

Conclusively, we have calculated the photoelectron spectrum from laser-assisted XUV ionization, and in the process found an expression for, and magnitude of, potential-laser coupling. These results were used to clarify ambiguities in approximate models for interference structures in HHG emission and lay a solid foundation for a key ingredient in Quantum State Reconstruction of molecular orbitals using HHG.

Chapter 7

Effects of vibration and rotation on High Harmonic Generation and Above Threshold Ionization

7.1 Synopsis

Numerical calculation of both light generated by High Harmonic Generation in molecules and momentum spectra of electrons ionized from molecules by strong fields are computationally very heavy. To facilitate such numerics, several approximations must be made. In this chapter, we look closely at the commonly used approximation of considering the nuclei fixed during the above processes. We show how different configurations of nuclear coordinates add to the total signal at various levels of approximation.

This chapter is based on the article [101].

7.2 Introduction

We already mentioned in the previous chapter 6 that the durations of ultra-short pulses can easily be of the timescale of nuclear motion in molecules and

down to the timescale of electronic motion. For this reason, these pulses have many uses in probing dynamics of processes in molecules, and subordinately, can serve as probes for Quantum State Reconstruction (QSR). At least two such uses have already been demonstrated: the aforementioned reconstruction of a bound orbital of N_2 from High Harmonic Generation (HHG) [35], and the partial reconstruction of the motional state of electrons produced from Argon atoms by Above Threshold Ionization (ATI) [102]. The two processes of HHG (see section 6.2 for a brief introduction) and ATI (see subsection 6.4.2) will be the focus of this chapter, and we shall clarify how one can perform approximate theoretical calculations of such signals. A treatment like this is vital for extending the reconstruction procedure used in [35] to the case of non-perfect alignment, and extending the reconstruction procedure in [102] from atoms to molecules.

The precise numerical calculation of both the light produced by HHG and the state of the electrons produced from ATI are complicated businesses. For precise numerical calculations of HHG, one is forced to use approximations for such numerics to be feasible on present day computers. Even the simplest of all cases, the H_2^+ molecular ion, has not been numerically treated with all degrees of freedom included. For numerical calculations of ATI spectra too, simplifying approximations are an absolute necessity. One widespread and central approximation used in this chapter is the neglect of the movement of the nuclei during the emission of the HHG radiation and the ATI process. This approximation is fostered by the typical time intervals for nuclear particles to move appreciably within molecules being thousands of times longer than the corresponding time intervals for electrons, owing to the two kinds of particles having charge to mass ratios which differ by a factor of this order. Furthermore, we use for HHG only the dipole radiation stemming from the acceleration of electrons. This last point is barely an approximation at the high frequencies involved in HHG, where the thousands of times larger acceleration of the electrons will completely dominate the radiation stemming from acceleration of nuclei¹.

¹An order of magnitude estimate of the ratio of the nuclei's to the electrons' contribution to the HHG intensity spectrum is the ratio of their charge-to-mass ratios. This can be seen by the following classical argument, considering one atom for simplicity. An external electric field causes acceleration of one nucleus with charge q_N and mass m_N , and of q_N/q_e electrons with charge q_e and mass m_e . The emitted electric radiation field is proportional to the acceleration of the charged particles [103]. Using Newton's second law, the ratio of the magnitude of electric fields emitted from the electrons and the nucleus is approximately $m_N q_e / (m_e q_N)$. Thus, since we add electric fields and not intensities, the intensity cross terms between electronic and nucleic HHG are suppressed by a factor of at least $m_e/m_N \approx 10^{-3}$. The intensity contribution from terms with nuclei only is smaller by another factor of 10^{-3} . Though classical, the

With the use of approximate models, rather than using an exact description, comes also the risk of bewilderment on when to do what. For example, say one has an incoherent (e.g. thermal) mixed state of molecules exposed to an intense ultrashort laser pulse leading to HHG in the molecules while the nuclei are approximately stationary. We can calculate the electric fields produced from each spatial configuration of the nuclear particles. Should one then add the electric fields from the molecules with different nuclear coordinates, and then take the square to find the intensity - or should the intensities for molecules with different nuclear coordinates be added to find the signal? Does the answer depend on whether one starts out with a thermally mixed state or a pure state? The answer will turn out to be that the electric fields from molecules with different nuclear coordinates should be added, and then squared to find the intensity - regardless of whether the molecules are in a pure or mixed state of nuclear coordinates: Only the distribution of nuclear coordinates matter. An easy and correct way to immediately see this is that if the HHG is due to electronic motion alone, no measurement of the nuclei's coordinates is performed by measuring the HHG signal. Therefore, one could in principle measure the nuclear coordinates afterwards. Conclusively, different nuclear configurations are distinguishable and there cannot be quantum mechanical interference therefrom. One must remember, however, that even though there is no interference in the formation of electric fields, there will still be interference in the intensity signal from the squaring of the total electric field.

In spite of the straightforwardness of these arguments and the treatment below, a thorough treatment of these points of interference has, puzzlingly enough, not been published before. In effect, recent and otherwise excellent publications mistakenly add intensities for some or all of the nuclear coordinates to find the HHG signal [104], [105]. To prevent future misunderstandings, we give a brief, thorough and general treatment of the role played by the fixed nuclear degrees of freedom in HHG.

The related subject of ATI of molecules is also treated. Here, the molecules are ionized by an ultrashort pulse, and we consider the nuclei fixed while the electron propagates to the detector. This is certainly not literally true and requires some explanation since the time it takes an electron to reach a detector, a macroscopic distance of the order of decimeters, is certainly much greater than any rotational or vibrational period in the molecule. Nonetheless, considering the nuclei fixed is a good approximation because the time it takes the electron

argument is also valid in quantum mechanics due to Ehrenfest's theorem and Eqs. (7.3)-(7.4).

to propagate many atomic diameters away from the molecule is small compared to rotational and, often, vibrational periods. Thus, the nuclei are approximately fixed during the time where the electron is close enough to the molecule to experience complicated interactions. Conversely, at the times after ionization where the nuclei have moved appreciably, the ionized electron is so far away that only the long range centrally symmetric (monopole) terms have an effect. It is in this sense the nuclei can be considered fixed though the propagation of the electron.

The measurement performed on the ionized electron reveals its asymptotic momentum, giving no information on the behavior of the wave function close to the parent molecular ion. Therefore, by arguments similar to the HHG case above, the different nuclear configurations are distinguishable in principle, and we get no quantum mechanical interference from pure and mixed states of rotational and vibrational degrees of freedom alike. Only the distribution of internuclear distances and -angles play a role.

Having given away all the answers, let us proceed to the derivations. In section 7.3, the general situation pertaining to both HHG and ATI is stated. In section 7.4, we treat the effects of nuclear degrees of freedom on HHG spectra. In section 7.5, we give a similar treatment for the effects on ATI spectra. Finally, we briefly conclude the chapter in section 7.6.

7.3 General considerations

We consider HHG and general photo-ionization in molecules with ultrashort laser pulses. In these experiments, there are many molecules in the laser focus, and the molecules are initially in a thermal state at time $t = 0$. When the phase space density is low, and ignoring propagation effects such as phase matching for HHG, we can ignore the symmetrization of the states and merely use the single-particle density operator $\hat{\rho}(0)$ for calculation. The neglected propagation effects are often of great importance for HHG yields, but we neglect them here to clearly show the effects of the nuclear degrees of freedom. The thermal velocities in typical experiments are sufficiently small that we may neglect the doppler-shifts of both the incoming laser pulse(s) and the HHG light, and also neglect the thermal momentum shift of the photo-electrons. Therefore, we simply ignore translational degrees of freedom of the center of mass.

At time $t = 0$, the molecule is in a time-independent thermal state at temperature T . By definition, this is $\hat{\rho}(0) = \exp(-\hat{H}/k_B T)/Z$, where the partition function $Z = \text{Tr}[\exp(-\hat{H}/k_B T)]$, k_B is Boltzmann's constant and \hat{H} is the field free molecular Hamiltonian which includes all nuclear and electronic degrees of

freedom. We resolve this state on energy eigenstates $|\alpha\rangle$ with energy E_α , where $\alpha = (\varepsilon, \mathbf{n}, \mathbf{J})$ denotes the state of the molecule through electronic ε , vibrational \mathbf{n} and rotational \mathbf{J} indices. Resolving $\hat{\rho}(0)$ on these states, there are only diagonal terms:

$$\hat{\rho}(0) = \sum_{\alpha} P_{\alpha} |\alpha\rangle\langle\alpha| \quad (7.1)$$

where $P_{\alpha} = \exp(-E_{\alpha}/k_B T)/Z$ is the Boltzmann weight. The system is now excited and propagated to the time t using the Schrödinger picture. The propagation is done by a unitary operator $\hat{U}(t)$ so that $\hat{\rho}(t) = \hat{U}(t)\hat{\rho}(0)\hat{U}^\dagger(t)$. In general, this interaction can change all aspects of the state, electronic, vibrational and rotational alike $\hat{U}(t)|\alpha\rangle = |\Psi_{\alpha}(t)\rangle$:

$$\hat{\rho}(t) = \sum_{\alpha} P_{\alpha} |\Psi_{\alpha}(t)\rangle\langle\Psi_{\alpha}(t)| \quad (7.2)$$

Specifically, the evolution due to $\hat{U}(t)$ can contain both alignment pulses and subsequent ultrashort-pulse ionization and HHG; the foci of this chapter. In both cases, the task amounts to finding the expectation value of a certain operator.

7.4 Effects of nuclear degrees of freedom on HHG

Treating HHG first, the frequency dependent emitted intensity $S(\omega)$ of polarization ϵ from many uncorrelated emitters can be found through the expectation value of the one-particle dipole moment $\mathbf{d}(t) = \langle\hat{\mathbf{d}}\rangle_t$ through [59], [106]:

$$S(\omega) = \left| \int_0^{t_m} dt e^{-i\omega t} \frac{d^2}{dt^2} \epsilon \cdot \mathbf{d}(t) \right|^2, \quad \text{where} \quad (7.3)$$

$$\begin{aligned} \mathbf{d}(t) &= \text{Tr} \left[\hat{\rho}(t) \hat{\mathbf{d}} \right] \\ &= \sum_{\alpha} P_{\alpha} \langle \Psi_{\alpha}(t) | \hat{\mathbf{d}} | \Psi_{\alpha}(t) \rangle, \end{aligned} \quad (7.4)$$

and t_m is the final moment of observation. This is exactly the same expression as used in section 4.5, leading to Eq. (4.12). Just as in chapter 4, one can observe interferences in the intensity $S(\omega)$ from incoherent members of the ensemble, i.e. members belonging to different α . Here too, one must keep in mind that

this effect of intensity interferences stems from adding electric fields and is fundamentally different from coherent quantum beats.

In usual numerical studies, one finds the state as a function of the particle coordinates. To follow this approach, we will insert two identity operators in the above expression, resolved on eigenstates of all the electrons' positions \mathbf{r}_e , all vibrational coordinates \mathbf{R} and all rotational angles $\mathbf{\Omega}$. For instance, if there are n electrons in three dimensional space, the vector \mathbf{r}_e has length $3n$. Thus, the identity operator is $\hat{I} = \int d\mathbf{r}_e d\mathbf{R} d\mathbf{\Omega} \mathcal{J}(\mathbf{R}, \mathbf{\Omega}) |\mathbf{r}_e, \mathbf{R}, \mathbf{\Omega}\rangle \langle \mathbf{r}_e, \mathbf{R}, \mathbf{\Omega}|$, where $|\mathbf{r}_e, \mathbf{R}, \mathbf{\Omega}\rangle = |\mathbf{r}_e\rangle \otimes |\mathbf{R}\rangle \otimes |\mathbf{\Omega}\rangle$ and $\mathcal{J}(\mathbf{R}, \mathbf{\Omega})$ is the numerical value of the Jacobian determinant for the transformation from the nuclei's cartesian- to $(\mathbf{R}, \mathbf{\Omega})$ -coordinates. Introducing these identities and the spatial wave functions $\psi_\alpha(\mathbf{r}_e, \mathbf{R}, \mathbf{\Omega}, t) = \langle \mathbf{r}_e, \mathbf{R}, \mathbf{\Omega} | \Psi_\alpha(t) \rangle$ in Eq. (7.4), we find:

$$\begin{aligned} \mathbf{d}(t) &= \sum_{\alpha} P_{\alpha} \int d\mathbf{r}_e d\mathbf{R} d\mathbf{\Omega} d\mathbf{r}'_e d\mathbf{R}' d\mathbf{\Omega}' \mathcal{J}(\mathbf{R}, \mathbf{\Omega}) \mathcal{J}(\mathbf{R}', \mathbf{\Omega}') \langle \Psi_{\alpha}(t) | \mathbf{r}_e, \mathbf{R}, \mathbf{\Omega} \rangle \\ &\quad \times \langle \mathbf{r}_e, \mathbf{R}, \mathbf{\Omega} | \hat{\mathbf{d}} | \mathbf{r}'_e, \mathbf{R}', \mathbf{\Omega}' \rangle \langle \mathbf{r}'_e, \mathbf{R}', \mathbf{\Omega}' | \Psi_{\alpha}(t) \rangle \\ &= \sum_{\alpha} P_{\alpha} \int d\mathbf{r}_e d\mathbf{R} d\mathbf{\Omega} \mathcal{J}(\mathbf{R}, \mathbf{\Omega}) |\Psi_{\alpha}(\mathbf{r}_e, \mathbf{R}, \mathbf{\Omega}, t)|^2 \mathbf{d}(\mathbf{r}_e, \mathbf{R}, \mathbf{\Omega}). \end{aligned} \quad (7.5)$$

So far, everything is exact, but the above formula is numerically daunting. To remedy this insurmountable computational complexity, we introduce several, commonly used approximations. The first of these, already discussed in section 7.2, is the assumption that the dipole moment leading to HHG is vastly dominated by the electrons' contribution $\mathbf{d}(\mathbf{r}_e, \mathbf{R}, \mathbf{\Omega}) \approx \mathbf{d}(\mathbf{r}_e)$. Considering n electrons and letting q be the elementary charge, this dipole moment explicitly reads $\mathbf{d}(\mathbf{r}_e) = -q \sum_n \mathbf{r}_{e,n}$, where $\mathbf{r}_{e,n}$ is the position vector of the n 'th electron from the molecular center of mass. Second, one can use the Born-Oppenheimer approximation to separate out the relatively slow rotational movement of the nuclei, obtaining:

$$\Psi_{\alpha}(\mathbf{r}_e, \mathbf{R}, \mathbf{\Omega}, t) \approx \psi_{\alpha}(\mathbf{r}_e, \mathbf{R}, t; \mathbf{\Omega}) \phi_{\alpha}(\mathbf{\Omega}, t),$$

where $\phi_{\alpha}(\mathbf{\Omega}, t)$ is the rotational part of the wave function, and $\psi_{\alpha}(\mathbf{r}_e, \mathbf{R}, t; \mathbf{\Omega})$ is the vibronic wave function for fixed rotational coordinates. This separation much eases the numerical propagation while the molecule is field-free, and also calculations of rotational excitations with non-ionizing laser pulses, for instance alignment. Thirdly, for most HHG pulses of interest, the rotational motion of the nuclei is so slow that it can effectively be considered fixed during the ultra-short interaction. This allows us to propagate the vibronic part $\psi_{\alpha}(\mathbf{r}_e, \mathbf{R}, t; \mathbf{\Omega})$

of the state in the strong laser field, while keeping the rotational coordinates fixed. These points taken into account, the dipole moment Eq. (7.5) is well approximated by:

$$\begin{aligned} \mathbf{d}(t) \approx & \sum_{\alpha} P_{\alpha} \int d\Omega |\phi_{\alpha}(\Omega, t)|^2 \int d\mathbf{R} \mathcal{J}(\mathbf{R}, \Omega) \\ & \times \int d\mathbf{r}_e |\psi_{\alpha}(\mathbf{r}_e, \mathbf{R}, t; \Omega)|^2 \mathbf{d}(\mathbf{r}_e). \end{aligned} \quad (7.6)$$

For molecules with vibrational frequencies much smaller than the inverse duration of the laser pulse causing HHG, the vibrational coordinates can also be treated as fixed, further easing calculations. If the Born-Oppenheimer approximation is precise for these degrees of freedom also, one can separate out the vibrational part of the vibronic wave function $\psi_{\alpha}(\mathbf{r}_e, \mathbf{R}, t; \Omega) \approx \psi'_{\alpha}(\mathbf{r}_e, t; \mathbf{R}, \Omega) \chi_{\alpha}(\mathbf{R}, t)$, yielding:

$$\begin{aligned} \mathbf{d}(t) \approx & \sum_{\alpha} P_{\alpha} \int d\Omega |\phi_{\alpha}(\Omega, t)|^2 \int d\mathbf{R} \mathcal{J}(\mathbf{R}, \Omega) |\chi_{\alpha}(\mathbf{R}, t)|^2 \\ & \times \int d\mathbf{r}_e |\psi'_{\alpha}(\mathbf{r}_e, t; \mathbf{R}, \Omega)|^2 \mathbf{d}(\mathbf{r}_e). \end{aligned} \quad (7.7)$$

The relevance of Eqs. (7.6) and (7.7) is that the propagation during the ultrashort pulse is immensely more manageable when the dimensionality is reduced. In fact, being able to keep the nuclei fixed through the HHG process, and merely propagate the electronic wave function $\psi'_{\alpha}(\mathbf{r}_e, t; \mathbf{R}, \Omega)$ is a necessary condition for numerical simulations to be carried through on present-day computers. The ro-vibrational part $|\phi_{\alpha}(\Omega, t)|^2 |\chi_{\alpha}(\mathbf{R}, t)|^2$ weighs the HHG contribution to the electric field from all the orientations and vibrational distances of the molecule, that was initially in the state α . Since these functions vary slowly with t compared to the electronic part during the ultrashort pulse, these functions can be taken to be time-independent during this interaction.

The effect of the vibrational motion is usually of much smaller consequence than the rotational. Indeed, for small vibrational excitations, one can as a first approximation set $\mathbf{R} = \mathbf{R}_0$, the equilibrium bond distances corresponding to the vibrational index in α .

As an example, we will consider a diatomic molecule with sufficiently low temperature that only the electronic ground state g_e is populated. Then $\alpha = (\varepsilon = g_e; \mathbf{n} = n; \mathbf{J} = J, M)$, where n is the vibrational quantum number in the electronic ground state, J is the angular momentum quantum number and M its projection on a space fixed axis. Furthermore, $\mathbf{R} = R$ is the internuclear

distance, $\mathbf{\Omega} = \Omega$ is the spherical polar solid angle. If $\hat{U}(t)$ describes only a single ultrashort laser pulse, the rotational degrees of freedom are unaffected and $\phi_{JM}(\Omega, t) = Y_{JM}(\Omega, t)$, the usual spherical harmonic function. Furthermore, $P_{g_e, n, J, M} = P_{n, J}$ is independent of M , and we get:

$$\begin{aligned} \mathbf{d}(t) &\approx \sum_{n, J, M} P_{n, J} \int d\Omega |Y_{J, M}(\Omega)|^2 \\ &\quad \times \int dR R^2 |\chi_n(R)|^2 \int d\mathbf{r}_e |\psi'_{g_e}(\mathbf{r}_e, t; R, \Omega)|^2 \mathbf{d}(\mathbf{r}_e) \\ &= \frac{1}{4\pi} \sum_n P_n \int dR R^2 |\chi_n(R)|^2 \int d\Omega \int d\mathbf{r}_e |\psi'_{g_e}(\mathbf{r}_e, t; R, \Omega)|^2 \mathbf{d}(\mathbf{r}_e), \end{aligned}$$

where we have used the identity $\sum_M |Y_{J, M}(\Omega)|^2 = (2J+1)/(4\pi)$ and $\mathcal{J}(R, \Omega) = R^2$.

If, in addition, only the lowest vibrational level $n = 0$ is initially populated, and approximating this vibrational wave function $|\chi_0(R)|^2 \approx \delta(R - R_0)$, we get:

$$\mathbf{d}(t) \approx \frac{R_0^2}{4\pi} \int d\Omega \int d\mathbf{r}_e |\psi'_{g_e}(\mathbf{r}_e, t; R_0, \Omega)|^2 \mathbf{d}(\mathbf{r}_e). \quad (7.8)$$

7.5 Effects of nuclear degrees of freedom on ATI

Having treated HHG, we turn our attention to ionization. In this setting, we measure the photoelectron angular distribution $W(\mathbf{k})$: the probability of measuring an electron with asymptotic, field free wave vector \mathbf{k} . That is, we only learn about the behavior of the electron in the asymptotic region, and not anything about the appearance of its wave function close to the nuclei. The quantity $W(\mathbf{k})$ is the expectation value of the projection operator $|\psi_{\mathbf{k}}\rangle\langle\psi_{\mathbf{k}}| \otimes \hat{I}_{\mathbf{R}, \Omega}$, where $|\psi_{\mathbf{k}}\rangle$ is the exact field-free continuum eigenstate in the asymptotic region with asymptotic momentum wave vector \mathbf{k} , and $\hat{I}_{\mathbf{R}, \Omega}$ is an identity operator working on the nuclear coordinates only. Finding the expectation value of this operator in the state $\hat{\rho}(t)$ from Eq. (7.2) gives us:

$$\begin{aligned} W(\mathbf{k}) &= \text{Tr}[\hat{\rho}(t)|\psi_{\mathbf{k}}\rangle\langle\psi_{\mathbf{k}}| \otimes \hat{I}_{\mathbf{R}, \Omega}] \\ &= \sum_{\alpha} P_{\alpha} \langle\Psi_{\alpha}(t)|\psi_{\mathbf{k}}\rangle\langle\psi_{\mathbf{k}}|\Psi_{\alpha}(t)\rangle. \end{aligned} \quad (7.9)$$

For ease of notation, we will here assume the time t to be just after the ultrashort pulse has ended; projecting on $|\psi_{\mathbf{k}}\rangle$ at any time later than this yields the

same result, since it is assumed to be the exact field-free continuum solution². Introducing again the position-resolved identity operators, we find:

$$W(\mathbf{k}) = \sum_{\alpha} P_{\alpha} \int d\mathbf{R} d\Omega \mathcal{J}(\mathbf{R}, \Omega) \left| \int d\mathbf{r}_e \psi_{\mathbf{k}}^*(\mathbf{r}_e) \Psi_{\alpha}(\mathbf{r}_e, \mathbf{R}, \Omega, t) \right|^2, \quad (7.10)$$

where $\psi_{\mathbf{k}}^*(\mathbf{r}_e) = \langle \psi_{\mathbf{k}} | \mathbf{r}_e \rangle$. From Eq. (7.9) to Eq. (7.10) no approximations or new physics have been introduced - we have simply written the inner products in the position basis. Nonetheless, we must use a simpler expression for $W(\mathbf{k})$ to make the numerical calculations feasible.

We will again use the Born-Oppenheimer approximation to separate out the rotational part of the excited state $\Psi_{\alpha}(\mathbf{r}_e, \mathbf{R}, \Omega, t) \approx \psi_{\alpha}(\mathbf{r}_e, \mathbf{R}, t; \Omega) \phi_{\alpha}(\Omega, t)$. As in the case of HHG, one can here assume that during interaction with the ultrashort ionizing pulse, $\psi_{\alpha}(\mathbf{r}_e, \mathbf{R}, t; \Omega)$ is propagated using fixed Ω .

$$W(\mathbf{k}) \approx \sum_{\alpha} P_{\alpha} \int d\Omega |\phi_{\alpha}(\Omega, t)|^2 \int d\mathbf{R} \mathcal{J}(\mathbf{R}, \Omega) \times \left| \int d\mathbf{r}_e \psi_{\mathbf{k}}^*(\mathbf{r}_e) \psi_{\alpha}(\mathbf{r}_e, \mathbf{R}, t; \Omega) \right|^2. \quad (7.11)$$

If we further assume the vibrational degrees of freedom to be fixed during the ultrashort ionizing pulse, we ease the numerical calculations significantly. Even further assuming that the system is well-described separating out the vibrational motion, we can write $\psi_{\alpha}(\mathbf{r}_e, \mathbf{R}, t; \Omega) \approx \psi'_{\alpha}(\mathbf{r}_e, t; \mathbf{R}, \Omega) \chi_{\alpha}(\mathbf{R}, t)$ whereby:

$$W(\mathbf{k}) \approx \sum_{\alpha} P_{\alpha} \int d\Omega |\phi_{\alpha}(\Omega, t)|^2 \int d\mathbf{R} \mathcal{J}(\mathbf{R}, \Omega) |\chi_{\alpha}(\mathbf{R}, t)|^2 \times \left| \int d\mathbf{r}_e \psi_{\mathbf{k}}^*(\mathbf{r}_e) \psi'_{\alpha}(\mathbf{r}_e, t; \mathbf{R}, \Omega) \right|^2. \quad (7.12)$$

Looking at Eqs. (7.11) and (7.12), we see exactly the same structure as in Eqs. (7.6) and (7.7): The contribution to the signal from molecules initially in

²There is a small caveat here: $W(\mathbf{k})$ *experimentally* only tells us about the asymptotic momentum distribution, so the projector $|\psi_{\mathbf{k}}\rangle\langle\psi_{\mathbf{k}}|$ only gives us information about the asymptotic spatial region. In contrast, when we later employ the Born-Oppenheimer approximation in a *calculation*, the state $|\psi_{\mathbf{k}}\rangle$ in the above projector corresponds to the exact continuum state in all space for the given fixed nuclear coordinates. A numerical way to make the two above approaches agree is to propagate the wave function to late times, where the free electronic wave function is far away from the parent ion. Then, a suitable region around the parent ion is removed, and the remaining part of the electronic wave function is projected on exact asymptotic momentum eigenstates.

the state α is the integral of contributions $|\int d\mathbf{r}_e \psi_{\mathbf{k}}^*(\mathbf{r}_e) \psi'_{\alpha}(\mathbf{r}_e, t; \mathbf{R}, \Omega)|^2$ from all different configurations of nuclear coordinates, weighed by the probability density $|\phi_{\alpha}(\Omega, t)|^2 |\chi_{\alpha}(\mathbf{R}, t)|^2$ of finding this nuclear configuration. The similarity comes naturally because we in both cases used the approximation of fixed nuclear coordinates and measured on the state of electrons only.

For the example diatomic molecule used above with HHG (only the ground electronic state with the lowest vibrational level initially populated), we find:

$$W(\mathbf{k}) \approx \frac{1}{4\pi} \int d\Omega \int dR R^2 |\chi_0(R, t)|^2 \left| \int d\mathbf{r}_e \psi_{\mathbf{k}}^*(\mathbf{r}_e) \psi'_{g_e}(\mathbf{r}_e, t; R, \Omega) \right|^2.$$

If, additionally $|\chi_0(R)|^2 \approx \delta(R - R_0)$, we find:

$$W(\mathbf{k}) \approx \frac{R_0^2}{4\pi} \int d\Omega \left| \int d\mathbf{r}_e \psi_{\mathbf{k}}^*(\mathbf{r}_e) \psi'_{g_e}(\mathbf{r}_e, t; R_0, \Omega) \right|^2.$$

7.6 Conclusion

In conclusion, we considered some widespread approximations used in numerical calculations of HHG- and ATI spectra from molecules. Approximations along these lines are a necessity for numerical calculation of these two processes. The most important of the approximations was that of considering the nuclei fixed during the HHG forming process, and during the propagation of ionized electrons until they are far away from the parent ion. Here, "far away" meant far enough to be influenced appreciably by only centrally symmetric forces from the parent ion. We found similar results of how to include nuclear degrees of freedom in finding the electric field of HHG and the momentum spectrum from ATI: Only the distribution of nuclear coordinates in the molecular sample was of importance, while coherence in nuclear coordinates played no role with the present approximations. One must remember, however, that while the momentum spectrum of ATI is directly observed, the HHG intensity is proportional to the squared electric field, which yields optical interferences. Of particular interest to us, we saw how an HHG signal from non-perfectly aligned molecules contains optical interferences between the different nuclear orientations. This conceptual realization could play a role in the reconstruction of bound molecular orbitals from HHG spectra [35], [88]. Furthermore, we saw that ATI spectra from non-perfectly aligned molecules had to be averaged over nuclear configurations. This last result could be important for the reconstruction of motional states of continuum electrons produced from ATI of molecules [102].

Chapter 8

Summary and Goodbye

Our trip is almost over, and it is time to take a look back at what has passed.

The first thing we did was to introduce the central ideas of Quantum State Reconstruction (QSR) in chapter 1. The objective, to find a quantum mechanical state, was to be reached by carefully looking at the results of measurements on an ensemble, and therefrom deduce what the quantum state had been. In effect, the measurements were, more than anything else, the determining factor for the feasibility of QSR. A certain convenient way to perform non-identical measurements was given: Simply perform identical types of measurements, but at different times. This way, the system dynamics, in the form of the Hamiltonian, became another determining factor for the feasibility of QSR.

In chapter 2, we saw the first methods of QSR, namely for the harmonic oscillator and free particle reconstructed from measurements of spatial distributions. In spite of the neat, closed form expressions for QSR in one spatial dimension, the extension to higher dimensions was not trivial. Indeed, the form of the Hamiltonian determined whether this was at all possible. A certain case where a full QSR for both systems was possible, was when the dynamics in the different spatial dimensions evolved with mutually incommensurable revival times. Another important thing, which became apparent, was that the extraction of information from measurements to perform QSR can be complicated, even borderline troublesome.

Chapter 3 dealt with QSR of rotating molecules; an inherently multidimensional system. Taught by our experiences from chapter 2, it was clear that we needed to restrict the state space, wherefrom QSR would pick out the right, reconstructed state. We found exactly such a situation in a widespread exper-

imental setup for non-adiabatic alignment of molecules, but we had to suggest a certain refinement of the usual measurements to guarantee complete QSR.

In chapter 4, we considered another degree of freedom in molecules, namely vibrational motion. The measurements used were different from the former chapters: Instead of using spatial distributions, we used emission spectra. These spectra contained information about transitions between energy eigenstates, and we were quite naturally led to a reconstruction in the energy basis. There were two free parameters in the problem: First, there was an index pertaining to an initially thermally populated level. Second, there was another index pertaining to the vibrational level excited from each initially thermally populated level. To perform QSR, it was consequently beneficial to have measurements depending on two parameters also. We found such a situation in a four wave mixing setup with ultrashort laser pulses. Here, (frequency resolved) spectra at different delays between the pulses gave us the two-parameter data we needed to separate the contributions from the different vibrational levels. To remedy our ignorance of the detailed dynamics, we introduced a calibration experiment which made QSR possible. Throughout the chapter, we neglected rotational degrees of freedom, which could have a large impact on the method's experimental feasibility. Lastly, we suggested that the central ideas in the chapter could be of wider applicability.

Chapter 5 dealt with a Bose-Einstein condensate, treated in the Bogoliubov approximation. This many-particle system is so complicated that a complete QSR seems nigh impossible. Instead, we severely limited the state space through finding the Maximum Entropy state corresponding to a limited number of measured quantities. What is more, we did not claim that this limited state was an approximation to the true many-particle state: The only desired reconstructed quantities were the normal- and anomalous second moments of the atomic ladder operators. The quality of the reconstruction turned out to depend dramatically on the nature of the state and the amount of measured quantities. Most remarkably, a condensate described by a single Gross-Pitaevskii wave function gave almost perfectly reconstructed second moments using only a small amount of measurements. In contrast, a condensate with a small thermal component was less well reconstructed, even with a larger amount of measurements. At present, this difference in reconstruction quality is not well understood.

The two chapters 6 and 7 did not present new QSR methods, but treated certain situations with atoms and molecules in strong laser fields. These situations are closely connected with two recent QSR experiments.

In chapter 6, we considered ionization of an atom with an attosecond Extreme Ultra Violet laser pulse in the presence of a moderately strong IR laser field. We found corrections to results obtained in the Strong Field Approxima-

tion, and we were able to interpret these corrections as an expression for the degree of non-separability of the continuum states into a commonly used separable form. Thereby, we could give conditions whose fulfillment would assure the applicability of the separable form. Furthermore, we were able to clarify an approximate model for interference structures in High Harmonic Generation (HHG) from diatomic molecules. Directly related to QSR, we provided a theoretical foundation for a key ingredient in a recent proposal for QSR of bound molecular orbitals.

Finally, chapter 7 showed how molecular rotational- and vibrational degrees of freedom could be approximately included in numerical calculations of spectra from HHG and Above Threshold Ionization (ATI) with ultrashort laser pulses. In both cases, the measured spectrum corresponded to measuring on the electron alone, whereby the rotational- and vibrational states were distinguishable in principle. Furthermore assuming that the nuclei could be considered fixed during the ultrashort interaction, we were led to conclude that both the produced HHG electric field and the ATI spectrum could be calculated as an average of contributions over the nuclei's coordinate distributions. Yet, the HHG spectrum still contains optical interferences from squaring the electric field. These results are useful in numerical calculations, but also in the QSR of bound orbitals from HHG spectra, and for QSR of motional states of electrons produced by ATI.

Moving through all these different subjects, it has become clear that QSR finds application in many research fields. Indeed, with its broad definition of "finding a quantum state from measurements", QSR is perhaps not so much a research field in itself, as a collection of methods with a common purpose. At any rate, QSR is enjoying increasing application. From being mostly a quantum optical phenomenon, QSR has spread into condensate-, molecular- and strong-field physics. In particular, the increasing interest in quantum control – controlling physical systems through their quantum state – could easily lead to QSR playing an important role in monitoring such controlled quantum states.

Last of all, I hope you enjoyed our trip. It was a pleasure having you along.

Anders

Appendix A

Wigner functions

Wigner functions are used as a conceptual tool in chapter 2 and as an illustrative tool in chapter 5. Due to their comparatively minor role in this report, only a few of their properties will be introduced in this appendix.

The Wigner function is a function that represents the quantum mechanical state of a system, a review can be found in [22]. Because it bears several resemblances with classical phase space distributions [107], it is often referred to as a "quasi-probability distribution" or "quantum mechanical phase space distribution".

In classical statistical mechanics, a central object of study is the phase space density $W_{\text{cl}}(x, p, t)$, giving the probability of finding a particle at the point x with a momentum p at time t . From this classical distribution function, the position- $\text{Pr}_x(x, t)$ and momentum-distributions $\text{Pr}_p(p, t)$ can be found:

$$\begin{aligned}\text{Pr}_x(x, t) &= \int_{-\infty}^{\infty} dp W_{\text{cl}}(x, p, t), \\ \text{Pr}_p(p, t) &= \int_{-\infty}^{\infty} dx W_{\text{cl}}(x, p, t).\end{aligned}\tag{A.1}$$

A natural question would be to ask if a similar distribution function can be found in quantum mechanics. Obviously, this is not straightforwardly answered, since a simultaneous position and momentum cannot be ascribed to a particle. Consequently, a quantity of the form:

$$W_s(x, p, t) = \text{Tr} [\hat{\rho}(t) \{\delta(x - \hat{x}) \delta(p - \hat{p})\}_s]\tag{A.2}$$

depends on the ordering parameter s , which determines the order of the \hat{x} and \hat{p} operators (or, equivalently \hat{a} and \hat{a}^\dagger), see e.g. [23] or [97]. This leads to a whole family of functions, but only the symmetric $s = 0$ (Weyl) ordering of the operator in Eq. (A.2) is used in this report. For this choice, the delta-operator in Eq. (A.2) becomes Hermitian:

$$\{\delta(x - \hat{x})\delta(p - \hat{p})\}_0 = \frac{1}{(2\pi)^2} \int_{-\infty}^{\infty} d\sigma \int_{-\infty}^{\infty} d\tau e^{i\sigma(\hat{x}-x)+i\tau(\hat{p}-p)}, \quad (\text{A.3})$$

and the real function $W_0(x, p, t)$ is exactly the Wigner function. From Eqs. (A.2) and (A.3), $W_0(x, p, t)$ is easily seen to fulfill Eqs. (A.1) and $\int dx \int dp W_0(x, p, t) = 1$. In contrast to the classical probability density, however, the Wigner function can have negativities, but only in phase space volumes smaller than \hbar . There has been much interest in measuring states with such negativities in their Wigner functions because this is interpreted as an explicitly non-classical feature.

The Wigner function has many other interesting and useful features, but we shall only mention that it has a 1 : 1 correspondence with the density operator $\hat{\rho}(t)$, which can be explicitly seen because we can get any matrix element in the complete position basis from $W_0(x, p, t)$ [108]:

$$\langle x|\hat{\rho}(t)|x'\rangle = \int_{-\infty}^{\infty} dp W_0\left(\frac{x+x'}{2}, p\right) e^{ip(x-x')/\hbar}. \quad (\text{A.4})$$

As stated in section 2.3, the quantum characteristic function in Eq. (2.1) is a complex Fourier transformation of the Wigner function. Therefore, the 1 : 1 correspondence of the characteristic function to the density operator is justified. Explicitly, changing variables in Eq. (2.3), $\tilde{w}(\eta, \theta) = \tilde{w}'[\sigma = \eta \cos(\theta), \tau = \eta \sin(\theta)]$, we get from Eq. (2.6):

$$W_0(x, p) = \int_{-\infty}^{\infty} d\sigma \int_{-\infty}^{\infty} d\tau \tilde{w}'(\sigma, \tau) e^{-i\sigma x - i\tau p}, \quad (\text{A.5})$$

which is a 1 : 1 mapping. We have thus established the 1 : 1 connection between density operators, characteristic functions and Wigner functions.

A final special result for the harmonic oscillator that deserves mentioning is that the Wigner function's marginals along rotated lines are the measured position distributions at different times. This lays the ground for tomography using inverse Radon transformations as in Eq. (2.6) [3], [4].

A.1 Discrete Wigner functions

For discrete systems, one can map the $N \times N$ (where N is odd¹) one-body density matrix to the real Wigner function $W(n, q)$ given on an $N \times N$ grid [20]:

$$W(n, q) = \frac{1}{N} \sum_{y=-M}^M \rho[f(n-y), f(n+y)] e^{4\pi i y n / N}, \text{ where} \quad (\text{A.6})$$

$$f(n-y) = \text{mod}(n-y, N) - M - 1.$$

The two arguments n and q can both assume N values, in our case $\{-M, -M+1, \dots, M\}$, like in Eq. (5.12). The mapping is bijective so the Wigner function contains all the information in the one-body density matrix. Furthermore, the wave number and spatial densities are easily recoverable:

$$\begin{aligned} \langle \hat{\psi}^\dagger(x_n) \hat{\psi}(x_n) \rangle &= \sum_{q=-M}^M W(n, q), \\ \langle \hat{a}^\dagger(k_q) \hat{a}(k_q) \rangle &= \sum_{n=-M}^M W(n, q). \end{aligned}$$

In the case of only one particle, the evolution of the quantum system is completely described by the Hamiltonian and the one-body density matrix. In chapter 5, having many particles, we instead have to specify all second moments to know the evolution of these; see Eq. (5.53). Therefore, the Wigner function is merely meant as an illustration of the one-body density matrix at a particular point of time.

¹The situation for even N is more cumbersome, see [20].

Appendix B

Numerical details of chapter 5

Several numerical problems may arise in finding the set $\{\lambda_\nu\}$ that satisfies the Eqs. (5.1). As already touched upon towards the end of section 5.3.1, we have treated the problem as a minimization of deviations. We have chosen to minimize the vector of deviations, Eq. (5.6), by using the Levenberg-Marquardt algorithm for the function `lsqnonlin` in the Matlab package. The most common problem encountered when using this approach is that for a given trial set $\{\lambda_\nu\}$, the matrix \mathcal{P} in Eq. (5.45) may not be positive definite. This problem can be remedied somewhat by testing for positiveness using a Cholesky factorization, which takes negligible time compared with the para-unitary diagonalization. A better solution is to make a good initial guess for the values of $\{\lambda_\nu\}$. One can do this by first running the minimization with an almost uniform momentum distribution (in case this is included as observables) or with $\langle \hat{a}_0^\dagger \hat{a}_0 \rangle$ set equal to N_{tot}/N , and then carrying out the subsequent program runs using the previously obtained $\{\lambda_\nu\}$ as initial values. In the subsequent program runs, one then gradually lets the momentum distributions approach the real distribution. A similar approach may be taken with the total number of particles, as making good guesses of the $\{\lambda_\nu\}$ may be easier at low particle numbers.

A trick we have made use of, which made guessing the $\{\lambda_\nu\}$ easier, is scaling down of the measured data. Since we are not interested in the true many-body density operator for the system, but only the second moments of the ladder operators, we may as well make the calculations for a smaller number of

particles, provided the calculations are still precise, and then rescale the data afterwards. As an example, we shall show how to perform this down scaling in the \mathbf{b} basis at $t = 0$.

Let $\langle \mathbf{b}\mathbf{b}^\dagger \rangle$ be the matrix of (unknown) second moments we wish to reconstruct. We will instead perform calculations on the matrix $\langle \mathbf{b}\mathbf{b}^\dagger \rangle_{DS}$, also having the characteristics of a matrix of second moments:

$$\begin{aligned} \langle \mathbf{b}\mathbf{b}^\dagger \rangle_{DS} &= \kappa \left[\langle \mathbf{b}\mathbf{b}^\dagger \rangle - \begin{pmatrix} I_N & 0 \\ 0 & 0 \end{pmatrix} \right] + \begin{pmatrix} I_N & 0 \\ 0 & 0 \end{pmatrix} \\ &= \kappa \langle \mathbf{b}\mathbf{b}^\dagger \rangle + (1 - \kappa) \begin{pmatrix} I_N & 0 \\ 0 & 0 \end{pmatrix}, \end{aligned} \quad (\text{B.1})$$

where I_N is the $N \times N$ identity matrix and κ is a real number. When reconstructing the matrix $\langle \mathbf{b}\mathbf{b}^\dagger \rangle_{DS}$ we must modify the measurements, retaining gN_{tot} and thereby the transformation matrices \mathcal{A} , \mathcal{B} , and \mathcal{U} . So, for instance, the scaled-down spatial density distributions that should be used can be found from

$$\begin{aligned} \langle \boldsymbol{\psi}(t)\boldsymbol{\psi}^\dagger(t) \rangle_{DS} &= \kappa \langle \boldsymbol{\psi}(t)\boldsymbol{\psi}^\dagger(t) \rangle + \\ &\quad (1 - \kappa) \mathcal{A}^{-1} \mathcal{B}^{-1} \begin{pmatrix} I_N & 0 \\ 0 & 0 \end{pmatrix} (\mathcal{A}^{-1} \mathcal{B}^{-1})^\dagger. \end{aligned}$$

Comparing the lower half part of the diagonals, we see that we should multiply the coordinate-space density measurements by κ and add to them $\frac{(1-\kappa)}{N} \sum_q v_q^2$. In a similar manner, measurements of other observables should be modified in the scaled down calculations. After the λ_ν has been found, relation Eq. (B.1) can easily be inverted, using the same point of time and basis as used in the original scaling.

Bibliography

- [1] U. Fano, *Description of States in Quantum Mechanics by Density Matrix and Operator Techniques*, Rev. Mod. Phys. **29**, p. 74-93 (1957).
- [2] D.-G. Welsch, V. Vogel and T. Opatrný, *Homodyne Detection and Quantum-State Reconstruction*, Progress in Optics, vol XXXIX, ed. by E. Wolf, North Holland, Amsterdam, p. 63-211 (1999).
- [3] J. Bertrand and P. Bertrand, *A tomographic approach to Wigner's function*, Found. Phys. **17**, p. 397-405 (1987).
- [4] K. Vogel and H. Risken, *Determination of quasiprobability distributions in terms of probability distributions for the rotated quadrature phase*, Phys. Rev. A **40**, p. R2847-2849 (1989).
- [5] G. Drobný and V. Bužek, *Reconstruction of motional states of neutral atoms via **MaxEnt** principle*, Phys. Rev. A **65**, 053410 (2002).
- [6] D. Leibfried, D. M. Meekhof, B. E. King, C. Monroe, W. M. Itano, and D. J. Wineland, *Experimental Determination of the Motional Quantum State of a Trapped Atom*, Phys. Rev. Lett. **77**, p. 4281-4285 (1996).
- [7] U. Leonhardt and M. G. Raymer, *Observation of Moving Wave Packets Reveals Their Quantum State*, Phys. Rev. Lett. **76**, p. 1985-1989 (1996).
- [8] E. Skovsen, H. Stapelfeldt, S. Juhl, K. Mølmer, *Quantum state tomography of dissociating molecules*, Phys. Rev. Lett. **91**, 090406/1-4 (2003).
- [9] J. R. Ashburn, R. A. Cline, P. J. M. van der Burgt, W. B. Westerveld and J. S. Risley, *Experimentally determined density matrices for $H(n=3)$ formed in H^+ -He collisions from 20 to 100 keV* Phys. Rev. A **41**, p. 2407-2421 (1990).

- [10] A. S. Mouritzen and K. Mølmer, *Tomographic reconstruction of quantum states in N spatial dimensions*, Phys. Rev. A **73**, 042105 (2006); quant-ph/0511173.
- [11] M. G. Raymer, D. F. McAlister and U. Leonhardt, *Two-mode quantum-optical state measurement: Sampling the joint density matrix*, Phys. Rev. A **54**, p. 2397-2401 (1996).
- [12] D. F. McAlister and M. G. Raymer, *Correlation and joint density matrix of two spatial-temporal modes from balanced-homodyne sampling*, J. Mod. Opt. **44**, p. 2359-2383 (1997).
- [13] T. Opatrný, D.-G. Welsch and W. Vogel, *Multi-mode density matrices of light via amplitude and phase control*, Opt. Comm. **134**, p. 112-116 (1997).
- [14] T. J. Dunn, I. A. Walmsley and S. Mukamel, *Experimental Determination of the Quantum-Mechanical State of a Molecular Vibrational Mode Using Fluorescence Tomography*, Phys. Rev. Lett. **74**, p. 884-887 (1995).
- [15] M. G. Raymer, M. Beck and D. McAlister, *Complex Wave-Field Reconstruction Using Phase-Space Tomography*, Phys. Rev. Lett. **72**, p. 1137-1140 (1994).
- [16] M. G. Raymer, M. Beck, and D. F. McAlister, *Using Phase-Space Tomography* in Quantum Optics VI, D. F. Walls and J. D. Harvey (eds.), Springer Verlag, Berlin, p. 245-253 (1994).
- [17] J. J. Sakurai, *Modern Quantum Mechanics*, Addison- Wesley, (1994).
- [18] G. M. D'Ariano, C. Macchiavello and M. G. A. Paris, *Detection of the density matrix through optical homodyne tomography without filtered back projection*, Phys. Rev. A **50**, p. 4298-4303 (1994).
- [19] U. Leonhardt, H. Paul and G. M. D'Ariano, *Tomographic reconstruction of the density matrix via pattern functions*, Phys. Rev. A **52**, p. 4899-4907 (1995).
- [20] U. Leonhardt, *Discrete Wigner functions and quantum state tomography*, Phys. Rev. A **53**, p. 2998-3013 (1996).
- [21] M. G. Raymer, *The Whittaker-Shannon sampling theorem for experimental reconstruction of free-space wave packets*, J. Mod. Opt. **44**, p. 2565-2574 (1997).

- [22] M. Hillery, R. F. O'Connell, M. O. Scully, E. P. Wigner, *Distribution functions in physics: Fundamentals*, Physics Reports **106**, p. 121-167 (1984).
- [23] K. E. Cahill and R. J. Glauber, *Ordered Expansions in Boson Amplitude Operators*, Phys. Rev. **177**, p. 1857-1881 (1969).
- [24] Y. Aharonov, J. Anandan, S. Popescu and L. Vaidman, *Superpositions of Time Evolutions of a Quantum System and a Quantum Time-Translation Machine*, Phys. Rev. Lett. **64**, p. 2965-2968 (1990).
- [25] T. C. Ralph, *Time Displaced Entanglement and Non-Linear Quantum Evolution*, arXiv: quant-ph/0510038, p. 1-5 (2005).
- [26] J. J. García-Ripoll, P. Zoller and J. I. Cirac, *Coherent control of trapped ions using off-resonant lasers*, Phys. Rev. A **71**, p. 062309/1-13 (2005).
- [27] E. Shchukin and W. Vogel, *Inseparability criteria for bipartite quantum states*, arXiv:quant-ph/0508132, p. 1-4 (2005).
- [28] L. M. Johansen, *Hydrodynamical Quantum State Reconstruction*, Phys. Rev. Lett. **80**, p. 5461-5464 (1998).
- [29] E. T. Jaynes, *Information Theory and Statistical Mechanics II*, Phys. Rev. **108**, 2, p. 171-190 (1957).
- [30] V. Bužek and G. Drobný, *Quantum tomography via the MaxEnt principle*, J. Mod. Optics **47**, p. 2823-2839 (2000).
- [31] A. S. Mouritzen and K. Mølmer, *Quantum state tomography of molecular rotation*, J. Chem. Phys. **124**, p. 244311/1-8 (2006); quant-ph/0512193.
- [32] J. J. Larsen, H. Sakai, C. P. Safvan, I. Wendt-Larsen and H. Stapelfeldt, *Aligning molecules with intense nonresonant laser fields*, J. Chem. Phys. **111**, p. 7774-7781 (1999).
- [33] F. Rosca-Pruna and M. J. J. Vrakking, *Experimental Observation of Revival Structures in Picosecond Laser-Induced Alignment of I₂*, Phys. Rev. Lett. **87**, 153902, p. 1-4 (2001).
- [34] F. Rosca-Pruna and M. J. J. Vrakking, *Revival structures in picosecond laser-induced alignment of I₂ molecules. I. Experimental results*, J. Chem. Phys. **116**, p. 6567-6578 (2002).

- [35] J. Itatani, J. Levesque, D. Zeidler, H. Niikura, H. Pe'pin, J. C. Kieffer, P. B. Corkum and D. M. Villeneuve, *Tomographic imaging of molecular orbitals*, Nature **432**, p.867-871 (2004).
- [36] H. Stapelfeldt and T. Seideman, *Colloquium: Aligning molecules with strong laser pulses*, Rev. Mod. Phys. **75**, p. 543-557 (2003).
- [37] P. W. Dooley, I. V. Litvinyuk, K. F. Lee, D. M. Rayner, M. Spanner, D. M. Villeneuve, and P. B. Corkum, *Direct imaging of rotational wave-packet dynamics of diatomic molecules*, Phys. Rev. A **68**, 023406, p. 1-12 (2003).
- [38] E. Péronne, M. D. Poulsen, H. Stapelfeldt, C. Z. Bisgaard, E. Hamilton and T. Seideman, *Nonadiabatic laser-induced alignment of iodobenzene molecules*, Phys. Rev. A **70**, 063410/1-9 (2004).
- [39] A. T. J. B. Eppinka and D. H. Parker, *Velocity map imaging of ions and electrons using electrostatic lenses: Application in photoelectron and photofragment ion imaging of molecular oxygen*, Rev. Sci. Instrum. **68**, p. 3477-3484 (1997).
- [40] V. Dribinski, A. Ossadtchi, V. A. Mandelshtam and H. Reisler, *Reconstruction of Abel-transformable images: The Gaussian basis-set expansion Abel transform method*, Rev. Sci. Instrum. **73**, p. 2634-2642 (2002).
- [41] G. B. Arfken and H. J. Weber, *Mathematical methods for physicists, 5th ed.*, Academic Press, San Diego (2001).
- [42] M. Tinkham, *Group Theory and Quantum Mechanics*, McGraw-Hill, New York (1964).
- [43] M. G. Raymer, M. Beck and D. F. McAlister, *Complex Wave-Field Reconstruction Using Phase-Space Tomography*, Phys. Rev. Lett. **72**, p. 1137-1140 (1994).
- [44] D. H. Parker and R. B. Bernstein, *Oriented Molecule Beams via the Electrostatic Hexapole: Preparation, Characterization, and Reactive Scattering*, Annu. Rev. Phys. Chem. **40**, p. 561-595 (1989).
- [45] S. R. Gandhi and R. B. Bernstein, *Focusing and state selection of NH₃ and OCS by the electrostatic hexapole via first- and second-order Stark effects*, J. Chem. Phys. **87**, p. 6457-6467 (1987).

- [46] J. E. Wollrab, *Rotational Spectra and Molecular Structure*, Academic Press, London (1967).
- [47] A. S. Mouritzen, O. Smirnova, S. Gräfe, R. Lausten and A. Stolow, *Reconstructing vibrational states in warm molecules using four-wave mixing with femtosecond laser pulses.*; arXiv:0706.1452 (2007).
- [48] A. M. Weiner, J. P. Heritage and R. N. Thurston, *Synthesis of phase-coherent, picosecond optical square pulses*, Opt. Lett. **11**, p. 153-155 (1986).
- [49] A. M. Weiner, D. E. Leaird, G. P. Wiederbrecht and K. A. Nelson, *Femtosecond Pulse Sequences Used for Optical Manipulation of Molecular Motion*, Science **247**, p. 1317-1319 (1990).
- [50] D. W. Schumacher, J. H. Hoogenraad, D. Pinkos and P. H. Bucksbaum, *Programmable cesium Rydberg wave packets*, Phys. Rev. A **52**, p. 4719-4726 (1995).
- [51] B. Kohler, V. Yakovlev, J. Che, J. L. Krause, M. Messina, K. R. Wilson, N. Schwentner, R. M. Whitnell and Y. Yan, *Quantum Control of Wave Packet Evolution with Tailored Femtosecond Pulses*, Phys. Rev. Lett. **74**, p. 3360-3363 (1995).
- [52] A. Assion, T. Baumert, J. Helbing, V. Seyfried, and G. Gerber, *Coherent control by a single phase shaped femtosecond laser pulse*, Chem. Phys. Lett. **259**, p. 488-494 (1996).
- [53] A. Zucchetti, W. Vogel, D.-G. Welsch and I. A. Walmsley, *Heterodyne measurement of vibrational wave packets of diatomic molecules*, Phys. Rev. A **60**, p. 2716-2725 (1999).
- [54] M. Shapiro, *Imaging of wave functions and potentials from time-resolved and frequency-resolved fluorescence data*, J. Chem. Phys. **103**, p. 1748-1754 (1995).
- [55] M. Shapiro, *Spectroscopic density-matrix imaging and potential inversion: the rotational effect*, Chem. Phys. **207**, p. 317-329 (1996).
- [56] I. Sh. Averbukh, M. Shapiro, C. Leichtle and W. P. Schleich, *Reconstructing wave packets by quantum-state holography*, Phys. Rev. A **59**, p. 2163-2173 (1999).

- [57] J. Faeder, I. Pinkas, G. Knopp, Y. Prior, and D. J. Tannor, *Vibrational polarization beats in femtosecond coherent anti-Stokes Raman spectroscopy: A signature of dissociative pump-dump-pump wave packet dynamics*, J. Chem. Phys. **115**, p. 8840-8454 (2001).
- [58] R. Lausten, O. Smirnova, S. Gräfe, A. S. Mouritzen and A. Stolow, *Observation of high-order fractional revivals in molecular wavepackets with Four-Wave mixing*, in preparation.
- [59] B. Sundaram and P. W. Milonni, *High-order harmonic generation: Simplified model and relevance of single-atom theories to experiment*, Phys. Rev. A **41**, p. 6571R-6573R (1990).
- [60] J. H. Eberly and M. V. Fedorov, *Spectrum of light scattered coherently or incoherently by a collection of atoms*, Phys. Rev. A **45**, p. 4706-4712 (1992).
- [61] O. Rubner, M. Schmitt, G. Knopp, A. Materny, W. Kiefer and V. Engel, *Femtosecond Time-Resolved CARS Spectroscopy on Binary Gas-Phase Mixtures: A Theoretical and Experimental Study of the Benzene/Toluene System*, J. Phys. Chem. A **102**, p. 9734-9738 (1998).
- [62] A. S. Mouritzen and K. Mølmer, *Tomographic reconstruction of quantum correlations in excited Bose-Einstein condensates*, Phys. Rev. A **71**, 033602/1-12 (2005).
- [63] E. A. Cornell and C. E. Wieman, *Nobel Lecture: Bose-Einstein condensation in a dilute gas, the first 70 years and some recent experiments*, Rev. Mod. Phys. **74**, p. 875-893 (2002).
- [64] W. Ketterle, *Nobel lecture: When atoms behave as waves: Bose-Einstein condensation and the atom laser*, Rev. Mod. Phys. **74**, p. 1131-1151 (2002).
- [65] E. Fick and G. Sauermaun, *The Quantum Statistics of Dynamic Processes*, Springer-Verlag, Heidelberg (1990).
- [66] S. S. Juhl, *Quantum State Tomography: Application to Dissociating Molecules*, Master Thesis, Niels Bohr Institute, University of Copenhagen (2003).
- [67] M. Olshanii, *Atomic Scattering in the Presence of an External Confinement and a Gas of Impenetrable Bosons*, Phys. Rev. Lett. **81**, p. 938-941 (1998).

- [68] G. E. Astrakharchik, D. Blume, S. Giorgini and B. E. Granger, *Quasi-One-Dimensional Bose Gases with a Large Scattering Length*, Phys. Rev. Lett. **92**, 030402/1-4 (2004).
- [69] N. Bogoliubov, *On the theory of superfluidity*, J.Phys. (USSR) **Vol. XI**, 1, p. 23-32 (1947), also reprinted in D. Pines, *The Many-Body Problem*, W.A. Benjamin Inc., New York 1961, p. 292.
- [70] J. H. P. Colpa, *Diagonalization of the Quadratic Boson Hamiltonian*, Physica **93A** p. 327-353 (1978).
- [71] L. P. Pitaevskii and S. Stringari, *Bose-Einstein Condensation (International Series of Monographs on Physics)*, Clarendon Press, (2003).
- [72] M. R. Andrews, M. O. Mewes, N. J. van Druten, D. S. Durfee, D. M. Kurn, and W. Ketterle, *Direct, Nondestructive Observation of a Bose Condensate*, Science **273**, p. 84-87 (1996).
- [73] A. I. Lvovsky, H. Hansen, T. Aichele, O. Benson, J. Mlynek, and S. Schiller, *Quantum State Reconstruction of the Single-Photon Fock State*, Phys. Rev. Lett. **87**, 050402/1-4 (2001).
- [74] M. T. DePue, C. McCormick, S. L. Winoto, S. Oliver, and D. S. Weiss, *Unity Occupation of Sites in a 3D Optical Lattice*, Phys. Rev. Lett. **82**, p. 2262-2265 (1999).
- [75] D. M. Stamper-Kurn, H. -J. Miesner, S. Inouye, M. R. Andrews, and W. Ketterle, *Collisionless and hydrodynamic excitations of a Bose-Einstein condensate*, Phys. Rev. Lett. **81**, p. 500-503 (1998).
- [76] J. E. Lye, J. J. Hope and J. D. Close, *Nondestructive dynamic detectors for Bose-Einstein condensates*, Phys. Rev. A **67**, 043609/1-13 (2003).
- [77] J. J. Hope and J. D. Close, *Limit to Minimally Destructive Optical Detection of Atoms*, Phys. Rev. Lett. **93**, 180402/1-4 (2004).
- [78] U. V. Poulsen and K. Mølmer, *Quantum states of Bose-Einstein condensates formed by molecular dissociation*, Phys. Rev. A **63**, 023604/1-11 (2001).
- [79] E. A. Burt, R. W. Ghrist, C. J. Myatt, M. J. Holland, E. A. Cornell, and C. E. Wieman *Coherence, Correlations, and Collisions: What One Learns about Bose-Einstein Condensates from Their Decay*, Phys. Rev. Lett. **79**, p. 337-340 (1997).

- [80] O. Smirnova, A. S. Mouritzen, S. Patchkovskii and M. Yu. Ivanov, *Coulomb-laser coupling in strong-field assisted photo-ionization and molecular tomography*, J. Phys. B. **40**, p. F197-F206 (2007).
- [81] M. Lewenstein, Ph. Balcou, M. Yu. Ivanov, A. L'Hullier and P. B. Corkum, *Theory of high-harmonic generation by low-frequency laser fields*, Phys. Rev. A **49**, p. 2117-2132 (1994).
- [82] T. Brabec and F. Krausz, *Intense few-cycle laser fields: Frontiers of non-linear optics*, Rev. Mod. Phys. **72**, p. 545-591 (2000).
- [83] M. Hentschel, R. Kienberger, Ch. Spielmann, G. A. Reider, N. Milosevic, T. Brabec, P. Corkum, U. Heinzmann, M. Drescher and F. Krausz, *Attosecond metrology*, Nature **414**, p. 509-513 (2001).
- [84] M. Lein, N. Hay, R. Velotta, J. P. Marangos and P. L. Knight, *Interference effects in high-harmonic generation with molecules*, Phys. Rev. A **66**, 023805/1-6 (2002).
- [85] M. Lein, N. Hay, R. Velotta, J. P. Marangos and P. L. Knight, *Role of the Intramolecular Phase in High-Harmonic Generation*, Phys. Rev. Lett. **88**, p. 183903/1-4 (2002).
- [86] C. Vozzi, F. Calegari, E. Benedetti, J.-P. Caumes, G. Sansone, S. Stagira, M. Nisoli, R. Torres, E. Heesel, N. Kajumba, J. P. Marangos, C. Altucci and R. Velotta, *Controlling Two-Center Interference in Molecular High Harmonic Generation*, Phys. Rev. Lett. **95**, p. 153902/1-4 (2005).
- [87] B. Zimmermann, M. Lein, and J. M. Rost, *Analysis of recombination in high-order harmonic generation in molecules*, Phys. Rev. A **71**, p. 033401/1-6 (2005).
- [88] S. Patchkovskii, Z. Zhao, T. Brabec and D. M. Villeneuve, *High Harmonic Generation and Molecular Orbital Tomography in Multielectron Systems: Beyond the Single Active Electron Approximation*, Phys. Rev. Lett. **97**, p. 123003/1-4 (2006).
- [89] M. Yu. Ivanov, M. Spanner and O. Smirnova, *Anatomy of strong field ionization*, J. Mod. Opt. **52**, p. 165-184 (2005).
- [90] L. B. Madsen, *Strong-field approximation in laser-assisted dynamics*, Am. J. Phys. **73**, p. 57-62 (2005).

- [91] O. Smirnova, M. Spanner and M. Yu. Ivanov, *Coulomb and polarization effects in laser assisted XUV ionization*, J. Phys. B **39**, p. 323-339 (2006).
- [92] O. Smirnova, M. Spanner and M. Yu. Ivanov, *Coulomb and polarization effects in sub-cycle dynamics of strong-field ionization*, J. Phys. B **39**, S307-S321 (2006).
- [93] G. L. Yudin, S. Patchkovskii, P. B. Corkum and A. D. Bandrauk, *Attosecond photoelectron interference in the separable Coulomb-Volkov continuum*, J. Phys. B **40**, p. F93-F103 (2007).
- [94] M. Jain and N. Tzoar, *Compton scattering in the presence of coherent electromagnetic radiation*, Phys. Rev. A **18**, p. 538-545 (1978).
- [95] P. Cavaliere, G. Ferrante and C. Leone, *Particle-atom ionising collisions in the presence of a laser radiation field*, J. Phys. B **13**, p. 4495-4507 (1979).
- [96] L. B. Madsen, *Gauge invariance in the interaction between atoms and few-cycle laser pulses* Phys. Rev. A **65**, 053417/1-5 (2002).
- [97] L. Mandel and E. Wolf, *Optical Coherence and Quantum Optics*, Cambridge University Press, New York (1995).
- [98] S. P. Goreslavski, G. G. Paulus, S. V. Popruzhenko and N. I. Shvetsov-Shilovski, *Coulomb Asymmetry in Above-Threshold Ionization*, Phys. Rev. Lett. **93**, p. 233002/1-4 (2004).
- [99] N. Bernstein and R. A. Handelsman, *Asymptotic Expansions of Integrals*, Dover, New York (1986).
- [100] N. G. Van Kampen, *The method of stationary phase and the method of Fresnel zones*, Physica **24**, p. 437-444 (1958).
- [101] C. B. Madsen, A. S. Mouritzen, T. K. Kjeldsen and L. B. Madsen, *Molecules in intense fields: Effects of alignment in high-harmonic generation and above threshold ionization*; Phys. Rev. A **76**, p. 035401/1-4 (2007); arXiv:physics/0703234.
- [102] T. Remetter, P. Johnsson, J. Mauritsson, K. Varjú, Y. Ni, F. Lépine, E. Gustafsson, M. Kling, J. Khan, R. López-Martens, K. J. Schafer, M. J. J. Vrakking and A. L'Hullier, *Attosecond electron wave packet interferometry*, Nature Phys. **2**, p. 323-326 (2006).

- [103] D. J. Griffiths, *Introduction to Electrodynamics, 3rd ed.*, Prentice Hall, New Jersey (1999).
- [104] F. H. M. Faisal, A. Abdurrouf, K. Miyazaki and G. Miyaji, *Origin of Anomalous Spectra of Dynamic Alignments Observed in N₂ and O₂*, Phys. Rev. Lett. **98**, 143001/1-4 (2007).
- [105] R. Torres, N. Kajumba, J. G. Underwood, J. S. Robinson, S. Baker, J. W. G. Tisch, R. de Nalda, W. A. Bryan, R. Velotta, C. Altucci, I. C. E. Turcu and J. P. Marangos, *Probing Orbital Structure of Polyatomic Molecules by High-Order Harmonic Generation*, Phys. Rev. Lett. **98**, 203007/1-4 (2007).
- [106] K. Burnett, V. C. Reed, J. Cooper and P. L. Knight, *Calculation of the background emitted during high-harmonic generation*, Phys. Rev. A **45**, p. 3347-3349 (1992).
- [107] L. E. Reichl, *A Modern Course in Statistical Physics, 2nd ed.*, John Wiley & Sons, New York (1998).
- [108] N. Mukunda, *Wigner distribution for angle coordinates in quantum mechanics*, Am. J. Phys. **47**, p. 182-187 (1979).